Hiroshima University,
Graduate School of Advanced Science and Engineering,
Earth and Planetary Systems Science Program

Effect of water-saturated cracks on seismic velocity and transport properties of oceanic crust

by

Yuya Akamatsu

A thesis for the degree of Doctor of Philosophy

February 2023

Abstract

Geophysical observations, such as seismic and electromagnetic surveys, have revealed that the presence of pore water is closely related to many geodynamic processes at various tectonic settings of the oceanic lithosphere. To quantitatively interpret those geophysical data and understand the subsurface fluid behavior, knowledge of cracks, which act as a fluid pathway and storage in the oceanic crust, is essential in the context of their geometry, distribution, and scale. This thesis provides experimental and theoretical constraints on the effects of microscopic and macroscopic water-saturated cracks on the geophysical properties of the oceanic crust based on comprehensive laboratory measurements and data analyses using core samples from the Oman Drilling Project.

Electrical resistivity and P- and S-wave velocities were measured under dry and water-saturated conditions for discrete cubic samples recovered from the Oman Drilling Project Hole GT3A. The experimental results reveal that electrical resistivity and elastic wave velocities are differently correlated with porosity. Performing joint inversion of the measured electrical and elastic properties combining an effective medium model and a statistical crack percolation model, the variations in electrical and elastic properties can be quantitatively related to the crack microstructural parameters: crack density and aspect ratio, as well as connectivity of cracks evaluated from crack density. Those data suggest that the oceanic crust can have wide ranges of abundance and geometry of microcrack.

To further understand the spatial distribution of microcracks in the oceanic crust, analyses of the continuous P-wave velocity structure measured by onboard whole-round Multi-Scanner Core Logger (MSCL-W) data for Hole GT3A were conducted. The representative elementary volume (i.e., REV), which is defined as a unit volume at which the physical properties become uniform, was estimated by calculating average P-wave velocities with increasing the window length. The results demonstrate that the scale of heterogeneity of microcrack structure in the

oceanic crust can be on the order of a few meters. This suggests that the pore pressure within the REV scale, caused by the seismic wave loading, is not able to reach an equilibrium state, which means the elastic moduli that are derived from the seismic velocity measurements can represent an unrelaxed state, which is different from the conventional assumptions.

As well as microcracks, there should be large-scale fractures in the oceanic crust, which potentially affect macroscopic geophysical properties. To assess the fracture porosity and permeability of the oceanic crust, X-ray CT images of the core sections collected from the GT sites of the Oman Drilling Project were used for analysis. The spatial distributions and geometry of macroscopic vein minerals, which can be considered to reflect the paleo-porosity structure in terms of macroscopic fractures, were quantified. The results show that despite having low paleo-porosity of ~0.1%, the oceanic crust can have significantly large paleo-permeability ranging from 10^{-9} m^2 to 10^{-13} m^2. This highlights the importance of taking the effect of macroscopic fractures on transport properties into account when interpreting geophysical data.

Finally, an upscaled geophysical property model is developed based on the characteristics of pore structure in the oceanic crust inferred from the data presented in the above studies. The upscaled model implies that the microcracks and fractures may have different impacts on the seismic and transport properties of the oceanic crust. The findings of this thesis can provide new insights that aid the quantitative interpretation of geophysical data from the in situ oceanic crust.

Acknowledgements

First and foremost, I would like to express my deepest gratitude to my supervisor Ikuo Katayama for his invaluable advice, support, encouragement, and supervision over more than six years. Without his clever guidance, ability to understand important aspects of research, and patience none of my papers and this thesis would have been possible.

I am extremely grateful to Keishi Okazaki, Kohei Hatakeyama, and Kazuki Sawayama for their commitment, availability, and enthusiasm. Keishi Okazaki generously provided knowledge and expertise about rock mechanics and experimental work. Kohei Hatakeyama always helped me out when I'm having trouble with my experiments since I was an undergraduate student. Kazuki Sawayama was always willing to discuss with me my research and offer his knowledgeable suggestions. I am also grateful to Kumpei Nagase for his assistance with my laboratory measurements and modal analyses of core samples from the Oman Drilling Project. Thanks should also go to Kazumasa Sueyoshi, Yuhki Matsuoka, Keiya Yamada, Yasushi Izuka, Kazumasa Tanimoto, and all the rest of Katayama-lab members.

I appreciate Natsue Abe, Katsuyoshi Michibayashi, Tomoaki Morishita, and Eiichi Takazawa, for their kind support and encouragement during and after the ChikyuOman project and providing me core samples and XCT data. Talking with Hanaya Okuda always motivated me to put effort into my research.

Most parts of this research have been funded by JSPS Research Fellowship for Young Researcher DC1 (Grant number: 20J22228).

Lastly, I would be remiss in not mentioning my family and friends. Without their support and encouragement, I would not have gotten through the last three years of my doctoral program during the COVID-19 pandemic.

Contents

Chapter 1

Introduction

1.1 Background and motivation

1.1.1 Water in the oceanic crust

The transport of water through the pore spaces in the oceanic crust is linked to several geoscientific processes near the Earth's surface. Close to mid-ocean ridges with a relatively-fast spreading rate, normal faulting associated with the ridge spreading can cause extensional fractures, which in turn lead to fluid circulation that acts as a heat and chemical carrier (Müller & Dutkiewicz, 2018; Stein & Stein, 1994). Pore water in the lithosphere can also become a candidate biosphere, which is considered to be a key to understanding the microbial habitability (Suzuki et al., 2020; Takai et al., 2008). The water stored in subducting plates can be supplied to the plate boundary and wedge mantle as subduction progresses. Pore water can also affect the mechanical and rheological properties of rock and has been linked to seismic activity (Saffer & Tobin, 2011; Warren-Smith et al., 2019). To understand the role of the pore water in these processes, it is essential to quantify the amount and dimension of the pore space in the oceanic crust.

Pore water can also alter rock's physical properties, including elastic wave velocity, electrical resistivity, and permeability (Guéguen & Palciauskas, 1994). Therefore, geophysical observations such as seismic and electromagnetic surveys have been used to indirectly infer the presence and distribution of subsurface water in the oceanic lithosphere (Chesley et al., 2019; Detrick et al., 1994; Fujie et al., 2013; Naif et al., 2015). Advancements in the observation methods and the analytical techniques have led to the availability of more detailed and

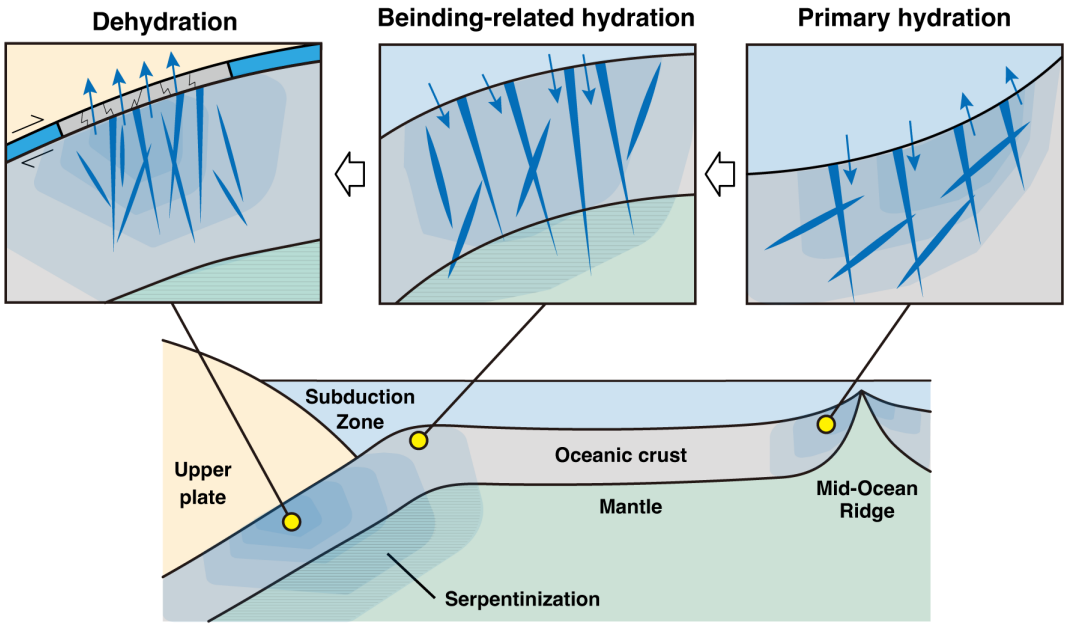

Figure 1.1 Schematic illustrations of hydration and dehydration of the oceanic crust.

comprehensive geophysical data, which provides insights into a more complete and accurate understanding of the geodynamic processes presented above. Meanwhile, to quantitatively extract the fluid behavior from these geophysical data and assess its role in the oceanic crust, it is still essential to know the fundamental relationship between the pore water and physical properties of oceanic crustal rocks. In this context, a number of laboratory measurements have been performed to explore the relationships between pore water and elastic wave velocity (Birch, 1961; Carlson & Miller, 2004; Christensen, 1984; Hatakeyama et al., 2021), electrical resistivity (Einaudi et al., 2005; Ildefonse et al., 2009; Pezard, 1990; Violay et al., 2010), and permeability (Brett-Adams et al., 2021; Christensen & Ramananantoandro, 1988; Gilbert & Bona, 2016) of oceanic crustal rocks. Thanks to these pioneering works, the knowledge of the physical properties of the oceanic crustal rocks has been clarified from the experimental point of view. However, those experimental results obviously indicate the effect of pore water at the laboratory scale (i.e., saturated microcracks and equant pores), whereas the actual geophysical data can reflect a macroscopic pore structure at a much larger scale. Although it has been implicitly assumed that the microscopic pore structure observed in the laboratory samples can be extrapolated to in situ macroscopic scale (i.e., homogenization), the natural lithospheric system possibly include heterogeneous and multi-scale porosities structures. In such a situation, the results of in situ scale geophysical data can contain both the impacts of

large-scale pore structures that cannot be taken into consideration in the laboratory. Indeed, recent studies combining laboratory- and field-scale acoustic measurements demonstrate a decrease in P-wave velocity with scale (Bailly et al., 2019; Matonti et al., 2015). This is a result of the increase in wavelength leading to the incorporation of a greater abundance of additional pore structures. Seismic measurements typically employ low-frequency (1–10 Hz) waves, which have long enough wavelengths to observe the effects of both large-scale cracks (i.e., fractures) and small-scale cracks. In addition, direct measurements of crustal permeability using boreholes at the seafloor have revealed that the upper parts of the young oceanic crust can have a bulk permeability several orders of magnitude larger than that measured in the laboratory (Fisher, 1998). This indicates that a principle similar to the upscaled seismic velocity may hold true for the transport properties, such as electrical resistivity and permeability (Guéguen et al., 1996). Given these lines of evidence, it is crucial to account for the porosity of both microcracks and fractures when quantitatively assessing the impact of pore water on the seismic and transport properties of the oceanic crust.

1.1.2 The Oman Drilling Project

To investigate the influence of porosity on the macroscopic physical and transport properties, it is preferable to comprehensively investigate rock samples at various scales. However, because of the difficulty of deep seafloor drilling and sampling, the sample recovery from the seafloor has been limited to the upper parts of the crust (Michibayashi et al., 2019). Although some International Ocean Drilling Program (i.e., IODP) expeditions recovered samples from the uppermost parts of the plutonic sequence of the oceanic crust (i.e., sheeted dike and gabbroic layers), the recovery of the core samples was incomplete (Teagle et al., 2006). Therefore, comprehensive investigations of oceanic crustal materials have been insufficient, and the pore structure and its spatial heterogeneity at the macoscopic scale are poorly known.

Ophiolites, which are fragments of ancient oceanic lithosphere that have been tectonically obducted onto continental margins, can provide us with opportunities to collect and observe rocks originating from the oceanic crust. The Samail ophiolite is the most extensive and well-exposed cross-section of the oceanic lithosphere (Nicolas et al., 2000), which exposes complete sections of sediments, pillow lavas, and mantle peridotite. Although many researchers have revealed the detailed geological structure and measured the physical properties of the surface outcrops, the information is limited to data from the limited number of outcrops and hand samples. Also, the surface environment is exposed to weathering and erosion, and their initial state is not always maintained. To reach a better understanding of the nature of

the subsurface hydrothermal processes preserved in the Samail ophiolite, continuous cores through the crustal section to the mantle section of the ophiolite was successfully sampled during the Oman Drilling Project of the International Continental Drilling Program (ICDP). The core samples were recovered from nine holes with a recovery rate of ~100% (Kelemen et al., 2020a). Using these core samples, we can comprehensively investigate the relationship between the pore structure and the physical and transport properties of the rocks that made up the actual oceanic crust.

1.2 Aim and objectives

This thesis aims to develop a new model to predict macropscopic geophysical properties of the oceanic crust that takes into account the effets of both microcracks and fractures, which might aid in improving the interpretation of geophysical data. The aim will be achieved through the following objectives using the core samples from the Oman Drilling Project:

1. to investigate the fundamental relationship among elastic wave velocity, electrical resistivity, and porosity by conducting laboratory measurements on elastic and electrical properties of cubic samples (~8 mm^3) collected by the Oman Drilling Project. The core samples show a wide range of porosity, suitable for asses the variations in the crack characteristics and the physical properties. The models linking those parameters via crack microstructural parameters were investigated.
2. to investigate the effect of relatively large-scale fractures on transport properties of the oceanic crust by obtaining the spatial distribution and abundance of vein minerals in the drilled cores of the Oman Drilling Project, which can be considered as fossilized fractures. The geometric information of those veins was combined with fracture fluid flow models to estimate the large-scale permeability. The estimated permeability can be used to discuss the effects of large-scale fluid flow on geophysical properties, in particular for seismic velocity.
3. to examine how those cracks and fractures are distributed in the oceanic crust. Although a number of previous studies implicitly assumed that homogeneous crack distribution can occur in the natural systems as observed for the laboratory samples, the damage itself may be heterogeneous, which substantially affects the interpretation of large-scale geophysical properties. The heterogeneity of cracks and fractures was evaluated using downhole variations in crack density and fracture porosity determined for the crustal sections of the Oman Drilling Project.

4. to develop new models that account for the effects of cracks and fractures on the in situ scale geophysical properties of the oceanic crust based on the datasets of crack/fracture.

1.3 Thesis structure

Chapter 2 describes laboratory physical property measurements performed on mini-cube samples to investigate the effect of microscopic cracks on the physical properties of oceanic crustal rocks collected from Hole GT3A of the Oman Drilling Project. To provide a quantitative assessment of crack geometry and connectivity, the relationship between elastic wave velocity and electrical resistivity is investigated by combining existing theoretical models. The combined model is then applied to the borehole logging data, which reflects a relatively large scale structure, leading to quantitative assessment of crack characteristics of in situ oceanic crust and highlighting the difference between those of the ophiolite and actual oceanic crust.

Chapter 3 examines the heterogeneity of crack distribution of Hole GT3A. Ultrasonic velocities that were measured continuously by the whole-round multi-scanner core logger (MSCL-W) during the shipboard description campaign of the Oman Drilling Project are utilized to assess the downhole distribution of crack density. The results show that the crack distribution can be heterogeneous at a larger scale, although it is homogeneous at the laboratory sample scale. Based on the results, the appropriate choice of the theoretical model to predict/interpret seismic velocity is discussed.

Chapter 4 presents the potential role of large-scale fractures on the transport properties of the oceanic crust. Vein minerals preserved in the drilled cores from the GT site (crustal sections) of the Oman Drilling Project are identified using X-ray Computed Tomography (XCT) images of the core sections, and their geometric information is applied to fracture fluid flow models to estimate the paleo-permeability structure of the oceanic crust. The estimated permeability is several orders of magnitude larger than that measured by laboratory experiments, indicating the importance of large-scale fractures on fluid circulation in the oceanic crust. Depending on the CT number of the vein-filling minerals, the veins show different spatial distributions and anisotropies of paleo-permeability, suggesting that the oceanic crust has undergone multi-stage fracturing and fluid flow.

Chapter 5 attempts to develop a new geophysical model that includes the effects of both cracks and fractures by incorporating the characteristics of cracks and fractures determined in the

previous chapters. Finally, the main findings and conclusions of this thesis are summarized.

Chapter 2

Cross-property relationship between electrical resistivity and elastic wave velocity of oceanic crustal rocks

2.1 Introduction

Cracks play a key role in subsurface processes in oceanic plates, including fluid transportation, chemical and heat exchange, and microbial activity (e.g., Fisher, 1998; Furnes et al., 2001; Stein & Stein, 1994). Cracks also have a substantial influence on rocks physical properties, such as seismic velocity, electrical and thermal conductivities, and permeability (Guéguen & Palciauskas, 1994). Therefore, geophysical observations have been conducted to explore pore structure and fluid behavior in the oceanic crust (e.g., Chesley et al., 2019; Detrick et al., 1994; Shearer, 1988). To quantitatively interpret geophysical data from such investigations and to evaluate the characteristics of pores and fluids, laboratory studies on relationship between physical properties and porosity are essential.

Electrical resistivity (i.e., the inverse of conductivity) at crustal depths is controlled mainly by fluid saturation of the pore network in rock. Therefore, the electrical properties of fluid-saturated rocks can provide valuable insights into subsurface fluid flow. The influence of pore structure on electrical conductivity has been investigated for porous rocks such as sandstones, primarily for engineering purposes (e.g., Cai et al., 2017; Pimienta et al., 2019). A number of previous studies have used Archie's law–which is an empirical relationship between electrical properties and porosity proposed by Archie (1942)–to relate the electrical conductivity to

the microstructure of the pore spaces (Guéguen & Palciauskas, 1994). Archie's law is valid for various rock types, including plutonic rocks such as granite and gabbro, and has been modified to include the effects of variable components (Glover et al., 2000; Glover, 2010). However, although Archie's law provides first-order information about the geometry of the pore network, it is difficult to quantitatively characterize the geometry and dimension of the pore spaces.

The elastic wave velocity (i.e., seismic velocity) of rocks is also dependent on porosity, as the elasticity of rock is highly sensitive to the presence of void spaces, such as cracks. According to the effective medium theory, which predicts the effective elastic moduli of cracked rocks, changes in elastic wave velocity can be attributed principally to crack density, crack geometry, and fluid properties (e.g., Guéguen & Kachanov, 2011; Kachanov, 1994; Kuster & Toksöz, 1974; O'Connell & Budiansky, 1974). Therefore, applying such theoretical models to the seismic properties of oceanic rocks can assist in the evaluation of the distribution and geometry of cracks and fluids in the oceanic crust (e.g., Shearer, 1988).

Electrical and seismic data are often interpreted independently by different parameters that describe the microstructures of pore space. However, because both electrical and elastic properties are influenced by cracks and fluids, linking these properties to joint microstructural parameters could provide valuable information about subsurface pore structure and fluid behavior (e.g., Carcione et al., 2007; Cilli & Chapman, 2021; Han, 2018; Iwamori et al., 2021; Pride et al., 2017). Although several studies have reported data for the electrical resistivity and elastic wave velocity of oceanic rock collected from various tectonic settings (e.g., Einaudi et al., 2000, 2005; Ildefonse & Pezard, 2001; Karato, 1983; Violay et al., 2010), little work has been performed to relate these properties of the oceanic crust to parameters describing pore structures (e.g., Evans, 1994).

Upon comparison with lithologies of ophiolites, which is interpreted as fragments of ancient oceanic lithosphere that have been tectonically emplaced on continental margins, the igneous oceanic crust formed at fast-spreading ridges is thought to be comprised typically of pillow lavas, sheeted dike complex, and gabbros (Figure 2.1a). Recently, [the International Continental Drilling Program (i.e., ICDP) Oman Drilling Project sampled continuous cores comprising the crustal section to the mantle section of the Oman ophiolite (Figure 2.1b), which is one of the best examples of the paleo-oceanic lithosphere in the world, with a recovery rate of ~100%. The recovered cores were systematically described and analyzed onboard in the laboratory of drilling vessel *Chikyu*, with preliminary data, including fundamental physical properties,

having been reported recently (Kelemen et al., 2020a). Recent studies have investigated the roles of pore space in the oceanic lithosphere using physical property data obtained onboard, such as electrical resistivity and elastic wave velocity (Katayama et al., 2020, 2021). However, although P-wave velocity (V_P) passing through the core samples was obtained during the shipboard measurements, S-wave velocity (V_S) was not measured because of the lack of a measurement system, despite the fact that a combination of P- and S-wave velocities can give information about crack geometry and fluid contribution. In addition, electrical resistivity was not measured for discrete samples from GT sites, which cover the crustal section of the Oman ophiolite.

In this study, to constrain the geophysical properties and pore structures of oceanic crust, we measured electrical resistivity and elastic wave velocities (P- and S-wave velocities) of mafic rock samples collected from Oman Drilling Project Hole GT3A. Hole GT3A was drilled through the transition zone from the sheeted dike complex to the underlying gabbro of the Oman ophiolite, which corresponds to the boundary between upper and lower oceanic crusts. We first present the conventional interpretations of the measured electrical resistivity while comparing them with previous studies. Then, we newly proposed the cross-property relationship between electrical and elastic properties that combines an effective medium model by Kachanov (1994) and a statistical crack fluid flow model by Guéguen & Dienes (1989) with percolation theory, and attempted quantitative interpretations of the laboratory data by performing joint inversion. Finally, we apply this cross-property relationship to geophysical data obtained by borehole logging measurements at International Oceanic Drilling Program (i.e., IODP) Hole 1256D, which drilled entire upper oceanic crust formed at fast-spreading ridge, as a basis for examining the nature of cracks and the effect of in situ conditions in the oceanic crust.

2.2 Method

2.2.1 Core samples

The Oman Drilling Project obtained continuous core samples from the upper oceanic crust to the uppermost mantle in the Oman ophiolite, with a recovery rate of ~100% (Kelemen et al., 2020a). Hole GT3A continuously sampled the transition zone from the sheeted dike to the underlying gabbro of the crustal sections of the Oman ophiolite. The drillhole is divided into four lithologic sequences on the basis of the occurrence of gabbro in the core (Figure 2.1c): Upper Dike Sequence (Sequence I); Upper Gabbro Sequence (Sequence II);

Lower Dike Sequence (Sequence III); and Lower Gabbro Sequence (Sequence IV). Shipboard descriptions of thin sections have shown that all core samples of Hole GT3A are partly or highly altered due to hydrothermal activity (Kelemen et al., 2020d).

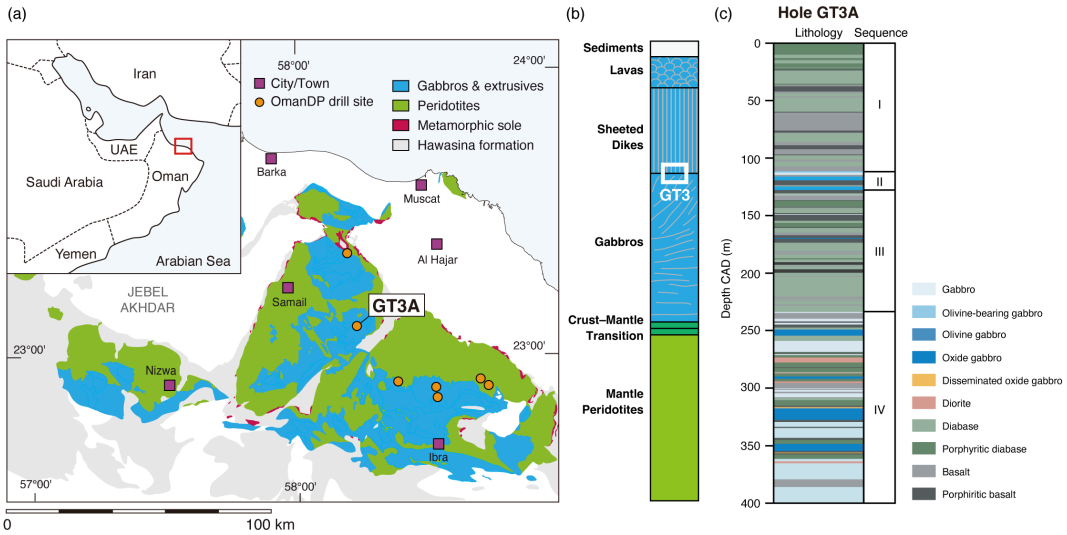

Figure 2.1 (a) Geological map of the southeastern massif of the Samail ophiolite (after Nicolas et al., 2000) showing the drill site locations of the Oman Drilling Project, including Hole GT3A. The colored units are the ophiolite sequence. The inset shows a map of the Arabian Peninsula, in which the location of the main figure is indicated by the red box. (b) Simplified stratigraphy of the Oman ophiolite. Hole GT3A corresponds to the sheeted dike–gabbro transition zone. (c) Borehole stratigraphy of Hole GT3A. Hole GT3A is divided into four lithologic sequences on the basis of the occurrence of gabbro: Upper Dike Sequence (I); Upper Gabbro Sequence (II); Lower Dike Sequence (III); and Lower Gabbro Sequence (IV).

The recovered core samples were systematically described and analyzed onboard D/V *Chikyu*. Discrete cubic samples (~2 cm × 2 cm × 2 cm) were taken from each core section, in which the x and y directions of the cubes were perpendicular and parallel to the split surface of the working halves, respectively, and the z direction was the down-hole axis. For the discrete samples from GT sites, fundamental physical properties such as bulk porosity, bulk/grain density, and P-wave velocity were measured. The mass and the volume of the solid phase of the samples were measured using the dual balance system and gas pycnometer, respectively, and the samples were vacuum saturated for >24 h in water based on the IODP protocols. Then, porosity and density were determined from the difference between dry and wet masses and the solid volume (for details, see Kelemen et al., 2020a).

To understand the relationship between physical properties and crack characteristics in more detail, information on S-wave velocity and electrical properties is required. In this study,

we conducted additional laboratory measurements of P- and S-wave velocities and electrical resistivity on a series of 94 cubic samples, as described below. The samples were selected to cover the wide variation in lithology and porosity of the core from Hole GT3A. The samples comprise mainly basalt, diabase, and gabbro (Figure 2.2). These samples are composed mainly of plagioclase and pyroxene, which are partly or completely replaced by secondary minerals such as amphibole and epidote. Basalt and diabase show intergranular texture but different matrix grain size, in which basalt is microcrystalline (<0.2 mm) and diabase is microcrystalline to fine grained (<1 mm; Figure 2.2a and c). Gabbroic rocks show variable textures, such as subophitic granular texture, and are mostly medium-grained (>1 mm; Figure 2.2b and d). A few gabbro samples contain minor amounts of oxide minerals and are classified as oxide gabbro (Figure 2.2d). More detailed descriptions of the igneous petrology and microstructural observations of the samples from Hole GT3A have been reported by Kelemen et al. (2020d).

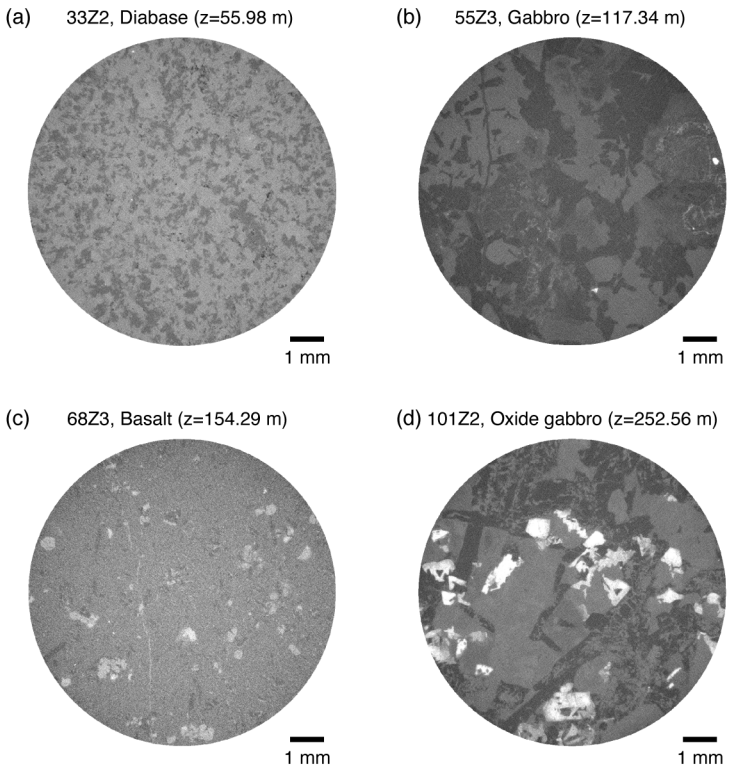

Figure 2.2 Representative 2D slices taken from X-ray μCT images of four samples. (a) 33Z2-60–62 cm (z = 55.98 m), fine-grained diabase. (b) 55Z3-54–56 cm (z = 117.34 m), medium grained gabbro. (c) 68Z3-67–69 cm (z = 154.29 m), microcrystalline basalt. (d) 101Z2-49–51 cm (z = 252.56 m), gabbro containing small amounts of oxide minerals (colored white).

2.2.2 Electrical properties

In a rock comprising an electrically insulating matrix and a connected pore space saturated with a conductive fluid, the electrical conductivity is controlled predominantly by electrolytic conduction by the fluid in the pore network. In the presence of clay minerals, a surface conduction mechanism should be taken into account. Surface conduction is caused by the presence of charges along the pore surface and is related to hydrothermal alteration through the cation exchange capacity of clay minerals (Waxman & Smits, 1968). Then, the total conductivity of a porous rock σ can be expressed as

$$\sigma = \frac{\sigma_{\text{fluid}}}{F} + \sigma_{\text{S}}, \tag{2.1}$$

where σ_{fluid} is the conductivity of the pore fluid, F is the formation factor, and σ_{S} is the surface conductivity (Waxman & Smits, 1968). Formation factor represents the contribution of the conductivity due to the pore space to the bulk conductivity and has been considered to reflect the 3D topology of the pore space (e.g., Ildefonse & Pezard, 2001; Violay et al., 2010). Because Equation 2.1 tends to overestimate the surface conductivity at low fluid salinity, Revil & Glover (1998) proposed a non-empirical statistical approach based on the pore space microgeometry as

$$\sigma = \frac{\sigma_{\text{fluid}}}{F}\left[1 - t^f_{(+)} + F\xi + \frac{1}{2}(t^f_{(+)} - \xi)\left(1 - \frac{\xi}{t^f_{(+)}} + \sqrt{\left(1 - \frac{\xi}{t^f_{(+)}}\right)^2 + \frac{4F\xi}{t^f_{(+)}}}\right)\right], \tag{2.2}$$

where $t^f_{(+)}$ is the Hittorf number of cations in the electrolyte that characterizes the mobility of ions. The dimensionless parameter ξ is defined by Kan & Sen (1987) as

$$\xi = \frac{\sigma_{\text{S}}}{\sigma_{\text{fluid}}}. \tag{2.3}$$

Table 2.1 Properties of brine used for electrical measurements

Salinity (g/L)	0.035	0.35	3.5	35	70
Resistivity (Ωm)	50	14.71	1.59	0.18	0.1

To characterize the electrolytic and surface conduction components of each sample, we performed a series of electrical resistivity (conductivity) measurements on the samples

saturated with five different salinities of NaCl solutions ranging from ~0.035 to ~70 g/, in a similar way to the IODP protocols (Table 2.1). The measured data for each sample were then fit by Equation 2.2, using a least-square inversion method to extract the intrinsic formation factor F and the surface conductivity σ_S with $t^f_{(+)}$ of 0.38 for NaCl solution (Revil & Glover, 1998). Measurements were performed in three orthogonal directions of the cubic samples by using an impedance analyzer at room temperature and pressure, with a set of two stainless steel electrodes (Figure 2.3a). To enhance the contact between the samples and the electrodes, paper filters soaked in brine water were placed on the top and bottom surfaces of the samples. The magnitude and phase angle of the complex impedance were measured with the frequency ranging from 20 Hz to 1 MHz (Figure 2.4).

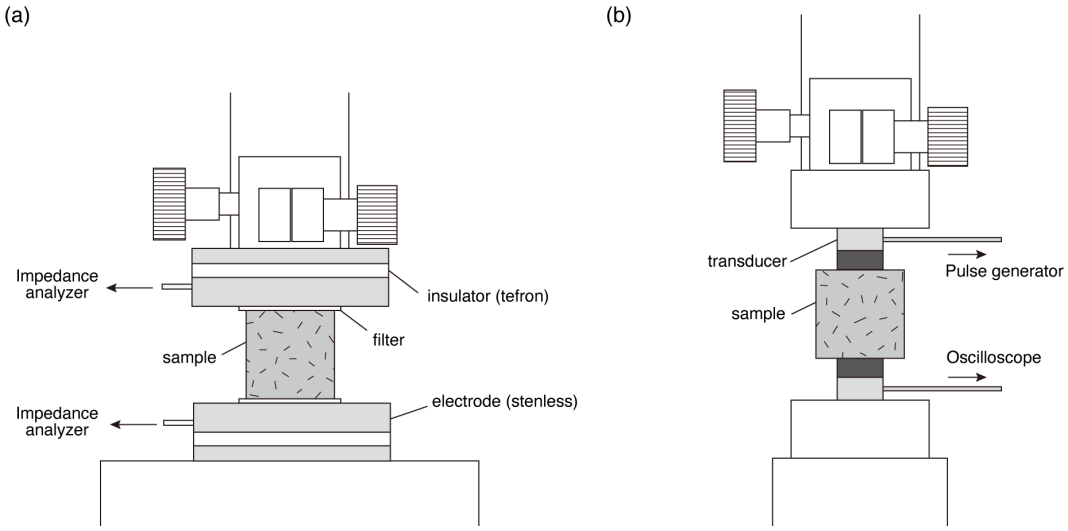

Figure 2.3 Schematics view of the experimental setups of (a) resistivity and (b) elastic wave velocity measurements.

To calculate the sample resistivity we used only data measured at ~100 Hz, which is similar to those used for the previous studies and borehole logging (Einaudi et al., 2005; Ildefonse & Pezard, 2001). Impedance measurements were also made on the samples under dry condition with stainless mesh filters to calculate the resistivity of the solid phase. The sample resistivity on the x-axis ρ_x can be calculated as

$$\rho_x = \frac{L_y L_z}{L_x} |Z| \cos\theta, \tag{2.4}$$

where L_x, L_y, and L_z are the sample lengths of each direction, respectively. The resistivities on the other directions were calculated in the same manner. The sample lengths were measured at three locations on each orthogonal direction with digital caliper and the mean

values of each direction were used for the resistivity calculation, in which the standard deviation of the lengths of each facing surfaces is usually <1%. The relative error in resistivity comes from the errors in the measured resistance and sample dimensions and ranges typically from 5% to 10% (Watanabe et al., 2019).

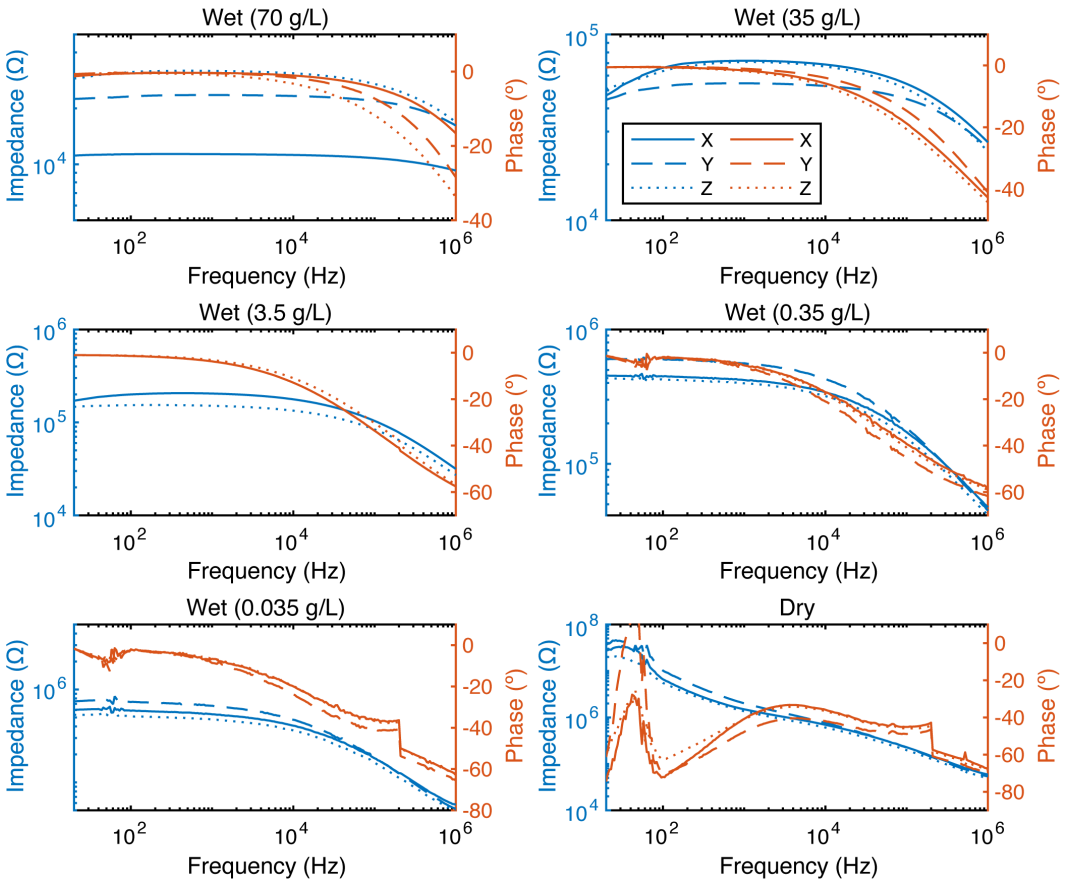

Figure 2.4 Example of impedance spectra as a function of frequency under dry and brine-saturated (wet) conditions (49Z-3, Basalt). Blues lines represent amplitude of impedance |Z|, and red lines represent phase shift θ.

2.2.3 Elastic wave velocity

We measured P- and S-wave velocities in three orthogonal directions of the cubic core samples under both dry and wet (water-saturated) conditions at room temperature and pressure. Under wet conditions, the samples were saturated with NaCl solution (3.5 g/L). Elastic wave velocities were determined by a pulse transmission method, in which travel times of ultrasonics passing through the sample were measured. P- and S-waves with a resonant frequency of 1 MHz were generated by transducers (Olympus V103-RM and V153-RM, 13

mm in diameter) attached to the framework (Figure 2.3b). An input pulse with an amplitude of 5 V was sent to the transducer by a pulse generator and was transmitted through the samples, and the output signal was received by another transducer mounted on the opposite side and digitalized by an oscilloscope at a sampling rate of 2.5×10^{10} s^{-1} (Figure 2.5). Elastic wave velocity was calculated by dividing the sample length by the travel time. The time of first arrival of the ultrasonic wave was determined using the Akaike Information Criterion (AIC). The waveform can be divided into intervals before and after the arrival time using the statistical AIC function:

$$AIC(t) = t \log(var(A[1,t])) + (T - t - 1) \log(var(A[t+1,T])), \qquad \text{(A1)}$$

where t is each sampling point; T is the total number of sampling points; and var denotes the variance in the signal data over the prescribed interval range (Hassanzadegan et al., 2014; Kurz et al., 2005; Sarout et al., 2009). The global minimum of the AIC corresponds to the onset time of the signal (Figure 2.6). To pick the onset time accurately, it is necessary to set an appropriate time window that includes the waveform regions of interest (Sarout et al., 2009). Time delay related to transducer faces and electronic circuitry was compensated by using a waveform measured with the two transducers in direct contact. The measurement error in elastic wave velocity can be evaluated from the errors in length and travel time, which is 1–2% for our samples.

2.3 Results

Although some samples show relatively large variations in electrical resistivity with respect to measurement direction, there are no systematic variations with respect to depth and orientation; therefore, we present the mean values (circle symbol) and the variations in the three orthogonal directions (bars) in all figures below in all figures below.

Figure 2.7a and b show depth variations of bulk porosity data that were reported by the shipboard measurements (Kelemen et al., 2020d) and electrical resistivity under wet conditions that we measured in this study, respectively. Although we measured sample resistivities using five different brine water concentrations, only those data obtained for 35 g/L (0.175 Ωm) brine water, which is similar to the salinity of sea water, are shown in Figure 2.7b. Resistivity ranges from 7 to 6876 Ωm, and its moving mean tends to be slightly higher in the Lower Gabbro Sequence compared with the other sequences (Figure 2.7b). This trend

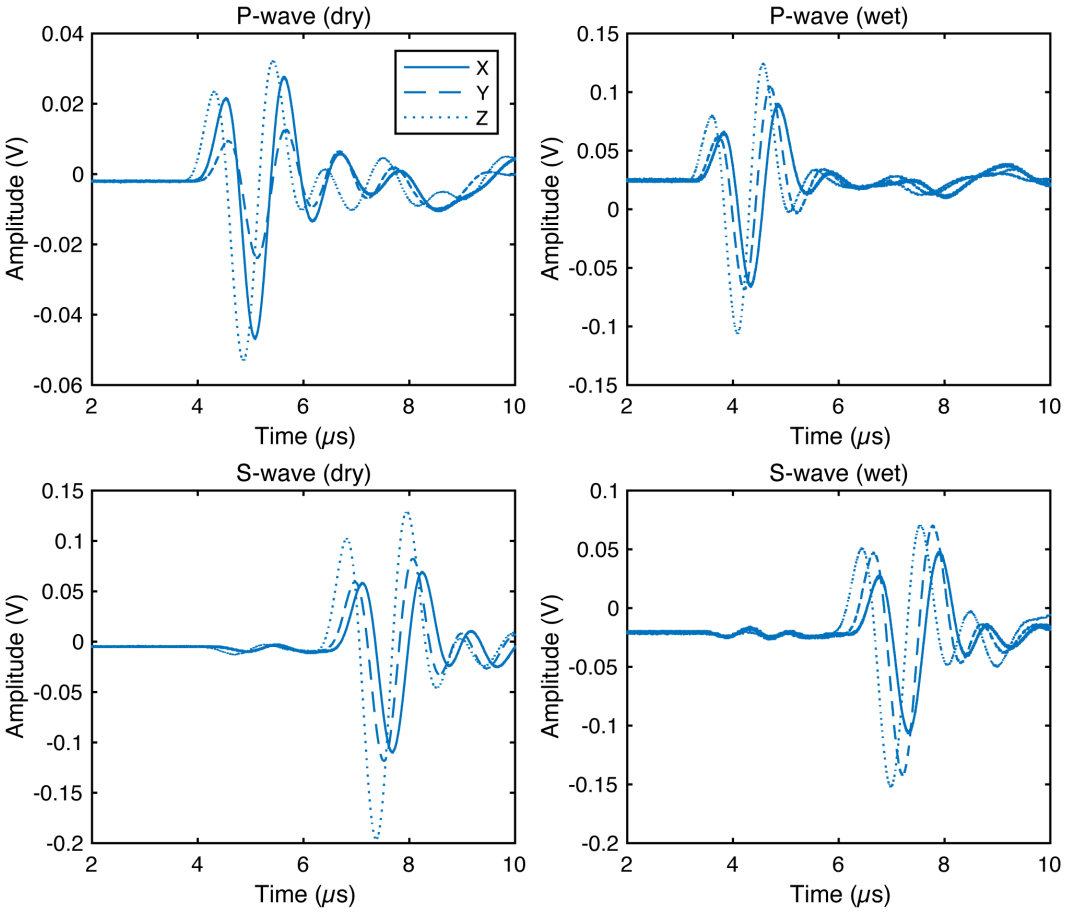

Figure 2.5 Example of waveforms of P- and S-waves under dry and brine-saturated (wet) conditions (49Z-3, Basalt).

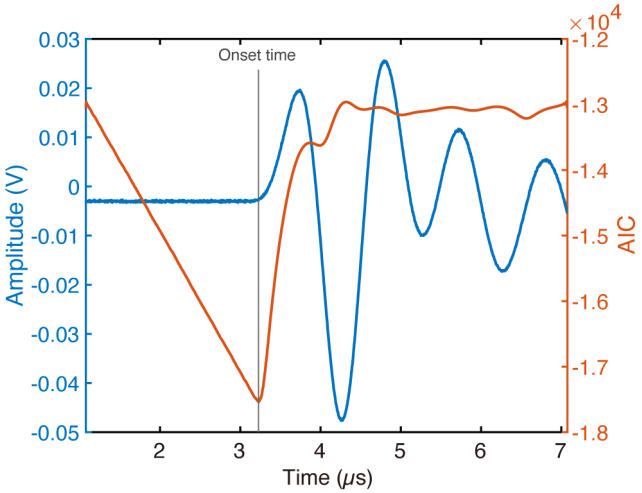

Figure 2.6 Example of the determination of the onset time of a P-wave by using the Akaike Information Criterion (AIC). The minimum of the AIC function corresponds to the onset time of the signal.

is also observed for the data obtained using different brine concentrations. Bulk porosity also varies widely from 0.09% to 11.27%, with the samples from the Lower Gabbro Sequence having the lowest porosities (Figure 2.7a).

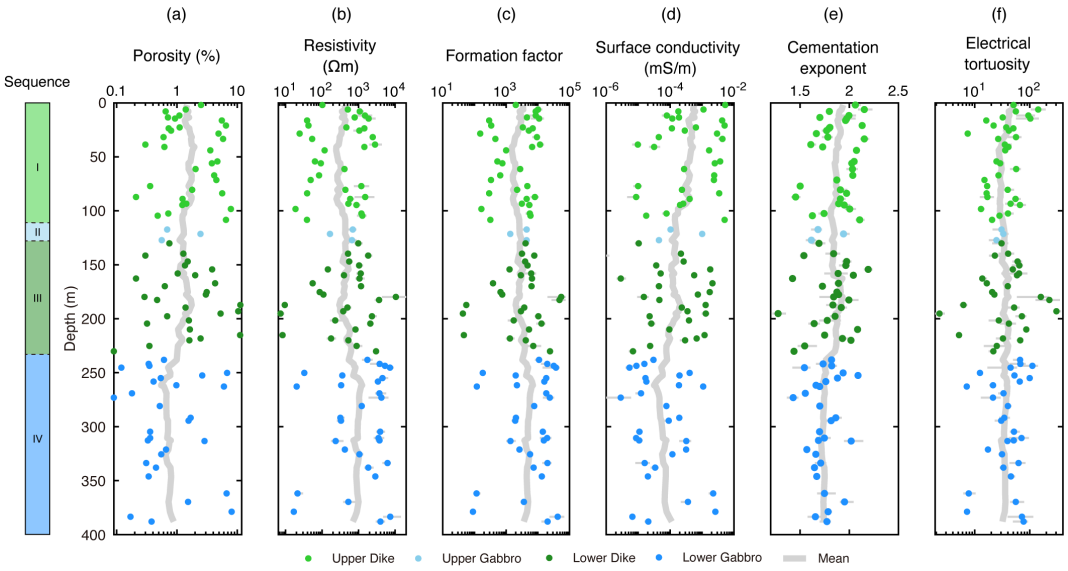

Figure 2.7 Depth variations of porosity and electrical parameters. (a) Porosity measured by shipboard measurements (Kelemen et al., 2020d). (b) Resistivity obtained using 35 g/L (0.175 Ωm) brine, which has a similar brine concentration to that of sea water. (c, d) Formation factor and surface conductivity calculated from Equation 2.2 based on a series of resistivity measurements using five different brine. (e, f) Cementation exponent and electrical tortuosity calculated from the porosity and the formation factor using Equations 2.5, 2.6. Except for (a), the data represent the mean values in three orthogonal orientations, and the bars indicate the variations in the measurement directions. Bold gray lines represent the moving mean values over 20 data points.

To evaluate the contributions of pore space and surface conduction to the bulk electrical conduction, we determined the formation factor F and surface conductivity σ_S by fitting the measured resistivities with five different brine for each sample (Figure 2.8). Formation factor ranges from 40 to 3873, and its moving mean increases slightly with depth (Figure 2.7c), suggesting that the pore structure changes with depth. Surface conductivity ranges from 10^{-6} to 10^{-2} S/m and shows a systematic decrease with depth (Figure 2.7d). This indicates that the degree of hydrothermal alteration decreases with depth and is possibly related to the variation in pore structure. Figure 2.9 shows the relationship between the porosity and the formation factor. The formation factor is correlated to the porosity, suggesting that the variation in resistivity is related to pore structure. We estimated the microstructural characteristics of the pore space by using two relationships between the formation factor and porosity, as described below. Archie (1942) proposed an empirical relationship between the

formation factor and porosity as

$$F = \phi^{-m}, \tag{2.5}$$

where m refers to the cementation exponent. The parameter m is roughly constant depending on rock type and typically ranges from 1.5 to 2.5 for most crystalline rocks (Guéguen & Palciauskas, 1994). In general, m has been considered to describe the non-uniformity of the cross-sections of the pore space (e.g., Ildefonse & Pezard, 2001; Violay et al., 2010). The formation factor can be also related to electrical tortuosity τ as

$$F = \frac{\tau}{\phi}. \tag{2.6}$$

The electrical tortuosity τ is commonly related to the complexity of the conduction channels or the degree of connectivity of the pore space (e.g., Violay et al., 2010). Fitting of our data of all samples using Equations 2.5, 2.6 yields $m = 1.76 \pm 0.04$ and $\tau = 35.2 \pm 5.8$. Note that Equation 2.2 was originally developed assuming $F = \phi^{-2}$, so that care should be taken in using the formation factor from Equation 2.2 to estimate the microstrucural parameters, althoug its influence is expected to be small.

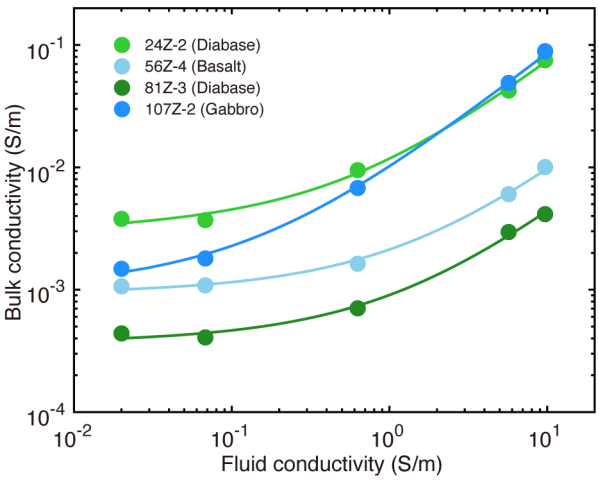

Figure 2.8 Examples of plots of the sample bulk conductivities as a function of the saturating fluid conductivity. Circle symbols are the representative data for each lithologic sequence. Best-fit curves were calculated using Equation 2.2.

We also applied Equations 2.5, 2.6 to individual data for first-order evaluation of the microstructural characteristics of the pore space of each sample. Depth variations of the calculate cementation exponent m and electrical tortuosity τ are shown in Figure 2.7 and f. Cementation exponent of each sample ranges from ~1.2 to ~2.2, and its mean trend decreases gradually with depth, where it tends to show slightly higher values in the Lower

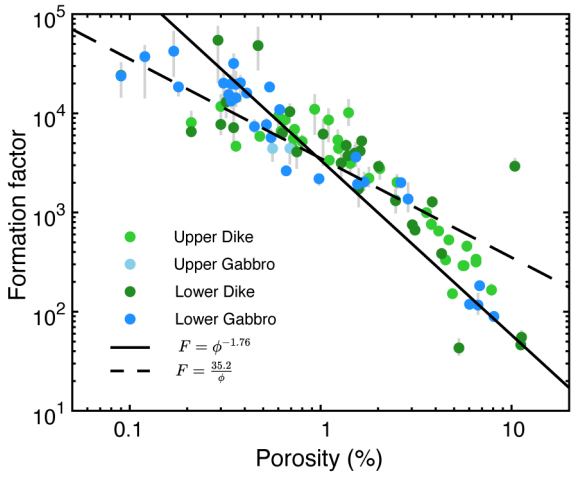

Figure 2.9 Formation factor as a function of porosity. The data represent the mean values in three orthogonal orientations, and the bars indicate the variations in the measurement directions. Solid and dashed lines are fitted results using Equations 2.5, 2.6, respectively.

Dike Sequence. This suggests that the geometry of the pore space changes with depth, as m is interpreted as the degree of non-uniformity of the cross-sections of the pores (Ildefonse & Pezard, 2001; Violay et al., 2010). Electrical tortuosity of each sample ranges from 2 to ~100, with the exceptions of a few outlier. In contrast to m, no depth trend is observed through the hole, suggesting that the complexity of the conduction paths does not depend on depth and hence lithologic sequence.

Figure 2.10 shows depth variations of elastic wave velocities that were obtained under dry and wet conditions. P-wave velocity (V_P) ranges from 3.53 to 6.89 km/s, and shows slightly higher values in the Lower Gabbro Sequence than in the sheeted dike sections. S-wave velocity (V_S) ranges from 1.66 to 3.77 km/s, with its mean profile showing a similar depth trend to that of P-wave velocity. The ratio between P- and S-wave velocities (V_P/V_S) under wet conditions is ~1.9 through the hole, and no clear depth trend is observed.

Figure 2.11 shows the relationships between the elastic wave velocities and the bulk porosity. Both P- and S-wave velocities decrease with increasing porosity, probably because of the presence of cracks, which can significantly lower the rocks elasticity. P-wave velocity in all case shows higher values under wet conditions than dry conditions, suggesting that the cracks become stiffened owing to water saturation (e.g., Guéguen & Kachanov, 2011). In contrast, S-wave velocity shows no clear difference between wet and dry conditions, possibly due to the lower sensitivity of the shear modulus to the presence of pore fluid (e.g., Guéguen & Kachanov, 2011). This different dependence of elastic wave velocities on the pore fluid results

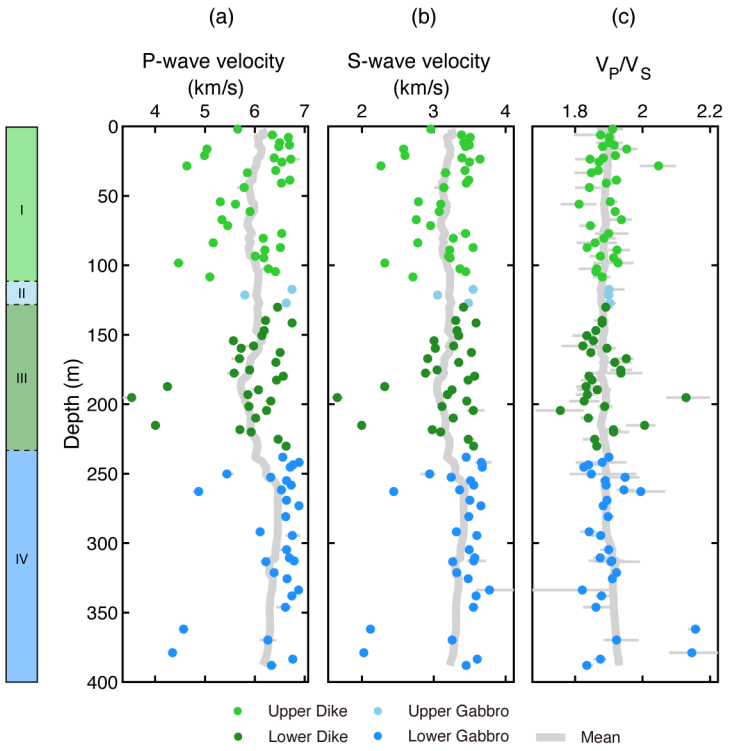

Figure 2.10 Depth variations of (a) P-wave velocity, (b) S-wave velocity, and (c) V_P/V_S. Symbols indicate the mean values, and bars represent the variation in the three orthogonal directions. Bold gray lines represent the moving mean values over 20 data points.

in different trends of V_P/V_S with bulk porosity for each condition (Figure 2.11c). Whereas V_P/V_S under dry conditions tends to decrease with porosity, V_P/V_S under wet conditions does not change markedly.

The formation factor and elastic wave velocities are clearly correlated with each other, in which the formation factor changes markedly at high-velocity regime (~6–7 km/s) and changes gradually through to low-velocity regime (Figure 2.12). This suggests that the electrical and elastic properties differently depend on pore structure.

2.4 Discussion

We observed gradual increases in electrical resistivity and formation factor from the sheeted dike section to the gabbro section of Hole GT3A. These increases can be related to changes in the microstructure of the pore network as expressed by m and τ. Although it is difficult to quantitatively evaluate the geometry of pore networks from m and τ, these parameters are useful for evaluating first-order information on the pore structure and making direct comparison with the literature data. In this section, we first compare those microstructures with the previous studies that measured petrophysical properties of oceanic crustal rocks collected from oceanic drilling sites and ophiolites. We also measured elastic wave velocities, which are highly sensitive to pore geometry and can be interpreted using various theoretical models. Effective medium theory has been widely applied to rocks containing cracks to relate the variation in elastic wave velocity to crack microstructural parameters (e.g., Guéguen & Kachanov, 2011; Kachanov, 1994; Kuster & Toksöz, 1974; O'Connell & Budiansky, 1974). We investigate the pore structure of the core samples of Hole GT3A by performing joint inversion of both electrical resistivity and elastic wave velocity combining the effective medium model by Kachanov (1994) and the statistical crack conductivity model by Guéguen & Dienes (1989) based on percolation theory. We compare the estimated crack porosities with the bulk porosities measured onborad and evaluate the validity of our modeling. Then, we apply the joint electrical-elastic properties relationship to in situ geophysical data obtained from IODP Hole 1256D to discuss the influence of external factors at in situ conditions such as pressure and the role of cracks in fluid flow and related processes in the oceanic crust.

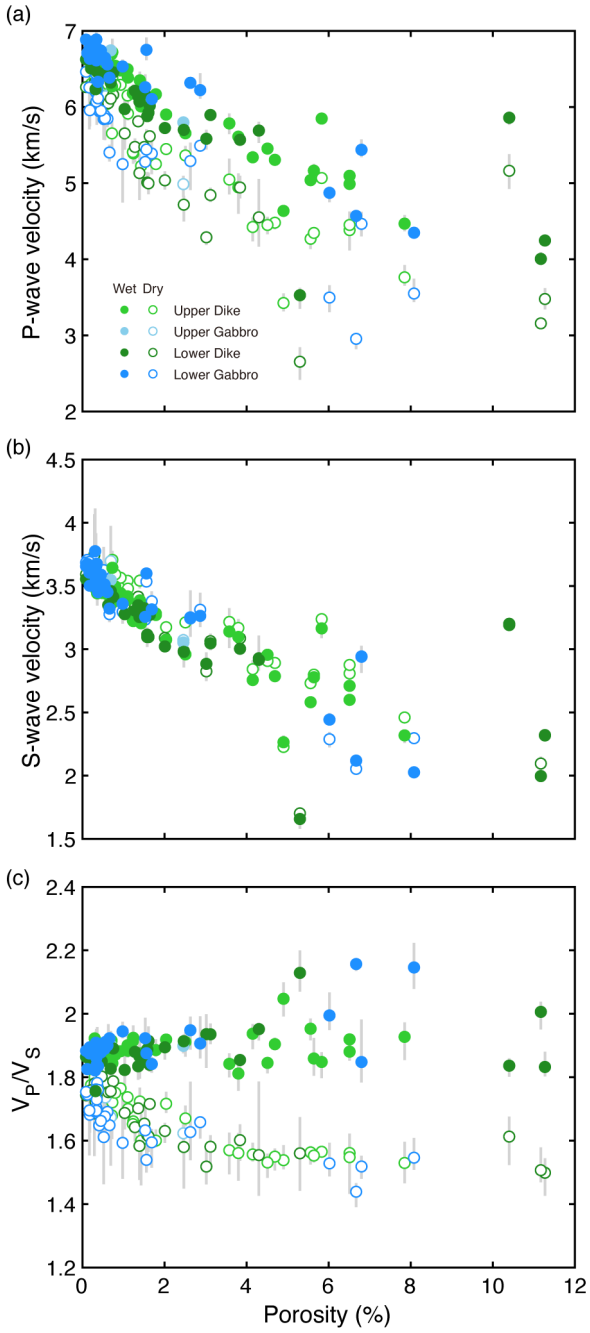

Figure 2.11 Relationships between porosity and (a) P-wave velocity, (b) S-wave velocity, and (c) V_P/V_S. The data represent the mean values in three orthogonal orientations, and the bars indicate the variations in the measurement directions.

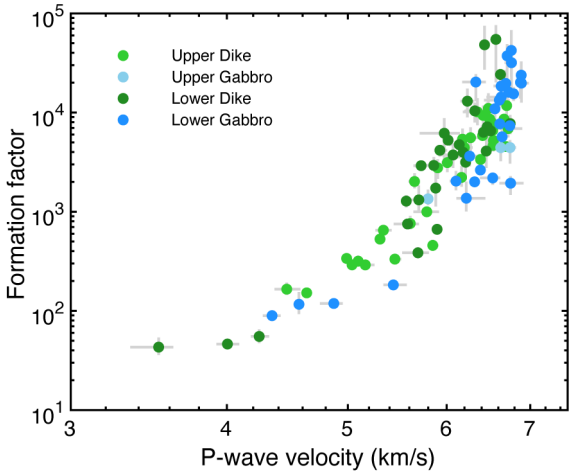

Figure 2.12 Relationship between P-wave velocity and formation factor. The data represent the mean values in three orthogonal orientations, and the bars indicate the variations in the measurement directions.

2.4.1 Comparison of electrical parameters with previous laboratory data

Measurements of petrophysical properties have been made on oceanic crustal rocks collected from various tectonic settings and have included measurements from oceanic drilling sites and ophiolites. Violay et al. (2010) reported the electrical and acoustic properties of mini-core samples collected from ODP/IODP Hole 1256D in the Cocos Plate, where the upper crust was drilled from the root zone of the sheeted dike complex to the uppermost part of the varitextured gabbros. Einaudi et al. (2000) measured a series of physical properties for volcanic rocks collected from a continuous transect along the Sarami Massif, which compirse the uppermost crustal section of the Oman ophiolite. Figure 2.13 presents a comparison of data for the electrical properties measured in this study with data reported for Hole 1256D and the Sarami Massif in Oman. The porosity values for the samples from the Sarami Massif are limited mainly to higher than ~1%, which coincides with the range of the sheeted dike section of Hole GT3A, and the microstructural parameters (F, m, and τ) for Hole GT3A are comparable with those for the Sarami Massif at a given porosity. This suggests that the geometry and topology of pore space of the crustal section of the Oman ophiolite are comparable with those of the volcanic section down to at least the sheeted dike section in Hole GT3A. In contrast, the formation factor values are slightly higher in Hole GT3A than in Hole 1256D, suggesting that the crustal section of the Oman ophiolite is slightly more resistive relative to in situ oceanic crust. The cementation exponent m and electrical

tortuosity τ are also higher in Hole GT3A than in Hole 1256D at the same porosity, meaning that Hole GT3A is characterized by higher complexity and non-uniformity of the pore space compared with Hole 1256D. The surface conductivity in Hole GT3A is similar to that in Hole 1256D at a given porosity, suggesting that the degree of hydrothermal alteration and/or nature of the alteration phase of Hole GT3A are similar to those of Hole 1256D, with cracks likely playing a role in hydrothermal fluid flow and subsequent alteration at the scale of grain boundaries (Violay et al., 2010).

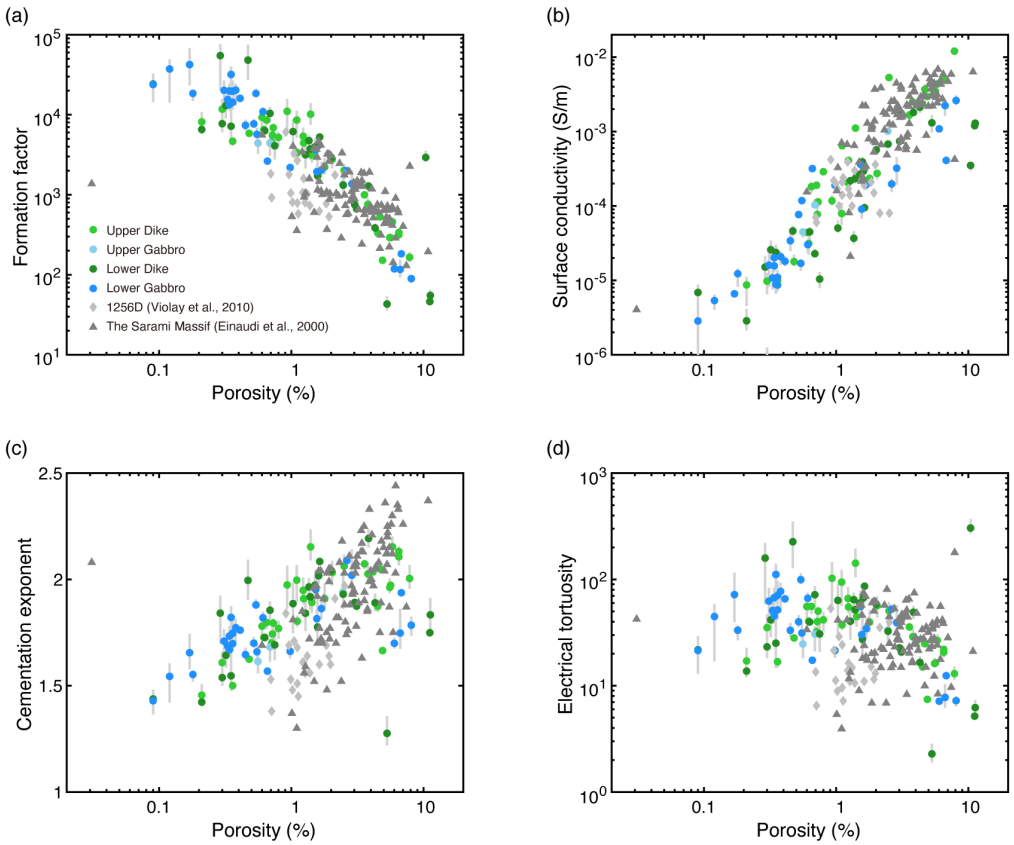

Figure 2.13 Comparison of electrical properties of Hole GT3A with data from IODP Hole 1256D (Violay et al., 2010) and the Sarami Massif in Oman (Einaudi et al., 2000). (a) Formation factor, (b) surface conductivity, (c) cementation exponent, (d) electrical tortuosity are plotted as a function of porosity. The data obtained in this study represent the mean values in three orthogonal orientations, and the bars indicate the variations in the measurement directions.

2.4.2 Cross elastic–electrical properties

2.4.2.1 Effective medium model for elastic wave velocity

A number of micromechanical models based on effective medium theory have been proposed for isotropic rocks with certain distributions of cracks (e.g., Kachanov, 1994; Kuster & Toksöz, 1974; Shafiro & Kachanov, 1997). For a medium containing circular cracks whose centers and normals are oriented randomly, the crack density ρ_c is defined as:

$$\rho_c = \frac{1}{V}\sum_N c_i^3, \tag{2.7}$$

where c_i is the radius of the ith crack, and N is the total number of cracks in a representative elementary volume V which is elastically homogeneous (Guéguen & Kachanov, 2011). According to Kachanov (1994) model, when neglecting interactions between individual cracks, the effective bulk modulus K^* and shear modulus G^* are given by:

$$\frac{K_0}{K^*} = 1 + \frac{h\rho_c}{1-2\nu_0}\left(1 + \left[\left(1-\frac{\nu_0}{2}\right)\frac{\delta_c}{1+\delta_c} - 1\right]\right) \tag{2.8}$$

and

$$\frac{G_0}{G^*} = 1 + \frac{h\rho_c}{1+\nu_0}\left(1 + \frac{2}{5}\left[\left(1-\frac{\nu_0}{2}\right)\frac{\delta_c}{1+\delta_c} - 1\right]\right), \tag{2.9}$$

where ν is Poisson's ratio, and subscript 0 denotes crack-free material (Fortin et al., 2007). The scalar parameter h is a geometric factor for a penny-shaped crack and is expressed as

$$h = \frac{16(1-\nu_0^2)}{9(1-\nu_0/2)}, \tag{2.10}$$

and δ_c is a non-dimensional parameter for penny-shaped crack defined by

$$\delta_c = \frac{3\pi}{16(1-\nu_0^2)}\frac{E_0}{K_f}\alpha, \tag{2.11}$$

where α is the mean aspect ratio of cracks defined as $\alpha = w/c$, where c and w are the mean crack radius and aperture, respectively, and K_f is the fluid bulk modulus. The parameter δ_c is referred to as the saturation parameter and determines the contribution of fluid to the effective bulk modulus (Benson et al., 2006; Fortin et al., 2011; Schubnel et al., 2006). These equations from Kachanov (1994) model allow the difference between the elastic wave velocity of crack-free rock and the measured velocities under wet conditions to be attributed to crack density and crack aspect ratio. In contrast, when a crack is filled with dry air, δ_c exceeds 1

owing to the extremely small K_f, meaning that the contribution of aspect ratio is negligible under dry conditions. For penny-shaped cracks, crack porosity can be estimated from crack density and mean aspect ratio as (Kachanov, 1994):

$$\phi_c = \pi \rho_c \alpha. \tag{2.12}$$

2.4.2.2 Statistical and percolation model for electrical resistivity

We observed that the nonlinear relationship between the formation factor and elastic wave velocity, in which the formation factor changes steeply at high-velocity regime and changes gradually through low-velocity regime (Figure 2.12). This steep change at higher velocities can be related to changes in both crack porosity and connectivity of cracks, as interpreted by percolation theory. Guéguen & Dienes (1989) showed that the transport properties of rocks containing cracks, such as permeability and electrical conductivity, can be modeled by the connection of cracks based on statistics and percolation theory. The effective conductivity for a rock containing randomly oriented cracks can be expressed as:

$$\sigma_{\text{eff}} = \frac{1}{4} f \phi_c \sigma_{\text{fluid}} + \sigma_{\text{solid}}, \tag{2.13}$$

where f is crack connectivity, ϕ_c is crack porosity, and σ_{fluid} and σ_{solid} are the fluid and solid conductivities, respectively. Crack connectivity represents the fraction of connected cracks, which can be calculated using a percolation model based on Bethe Lattice with the coordination number of four as:

$$f = 1 - 4\left(\sqrt{\frac{1}{p} - \frac{3}{4}} - \frac{1}{2}\right)^3 + 3\left(\sqrt{\frac{1}{p} - \frac{3}{4}} - \frac{1}{2}\right)^4, \tag{2.14}$$

where p is the probability that two cracks intersect each other and is given by (Guéguen & Palciauskas, 1994):

$$p = \frac{\pi^2}{4} \rho_c. \tag{2.15}$$

These relationships reveal that f can take any value from 0 to 1, which implies that p ranges between 1/3 and 1. This lower bound ($p = 1/3$) corresponds to the threshold for percolation, meaning that a conductive crack network starts to form when crack density reaches a critical value ($\rho_c \sim 0.135$).

2.4.2.3 Joint inversion of elastic wave velocity and electrical resistivity

Based on the models presented in the previous sections, both electrical resistivity ρ and elastic wave velocity V can be expressed as a function of crack density ρ_c and aspect ratio α as:

$$\rho = f(\rho_c, \alpha) \quad \text{and} \quad V = g(\rho_c, \alpha). \tag{2.16}$$

To quantify the microstructural characteristics of the pore space, we performed joint inversion of the measured velocities and resistivities using these models. We assumed an elastically homogeneous matrix containing randomly oriented cracks, given the observed weak anisotropy of elastic wave velocities. Then, crack density and aspect ratio were determined by performing a least-square inversion, in which the differences between the measured P- and S-wave velocities and electrical resistivity under wet conditions and the model predictions were simultaneously minimized. We defined the misfit function $\boldsymbol{r}$ to be minimized between the experimental and modeled values as follows:

$$\boldsymbol{r} = \begin{bmatrix} V_P^{\text{exp}} - V_P^{\text{model}}(\rho_c, \alpha) \\ V_S^{\text{exp}} - V_S^{\text{model}}(\rho_c, \alpha) \\ \log_{10} \frac{\rho^{\text{exp}}}{\rho^{\text{model}}(\rho_c, \alpha)} \end{bmatrix}. \tag{2.17}$$

This misfit function was minimized using the Levenberg–Marquardt method in MATLAB® software package.

Table 2.2 Elastic properties and densities of minerals used for calculation of Voigt-Reuss-Hill averages of porosity-free velocities.

Mineral	Bulk modulus K (GPa)	Shear modulus G (GPa)	Density (g/cm^3)
Plagioclase	75	34	2.68
Clinopyroxene	96	58	3.32
Amphibole	87	43	3.12
Olivine	131	81	3.32
Orthopyroxene	105	76	3.34
Quartz	37	44	2.65

The crack-free elastic wave velocities for each rock type were estimated from primary mineral abundances that were reported by shipboard descriptions of sample thin sections from Hole GT3A (Kelemen et al., 2020d). We calculated Voigt-Reuss-Hill averages of elastic moduli

for each sample using elastic moduli of mineral presented in Table 2.2 and determined the representative values for each rock type. The variations of the calculated crack-free velocities were 3–5% for velocities and ~10% for density for all rock types (Figure 2.14). The fluid bulk modulus was taken as $K_f = 2.2$ GPa. For the electrical properties, fluid conductivity was taken as $\sigma_{fluid} = 5.7$ S/m (salinity of 35 g/L), and solid conductivity was taken as $\sigma_{solid} = 2.0 \times 10^{-5}$ S/m based on the dry measurements.

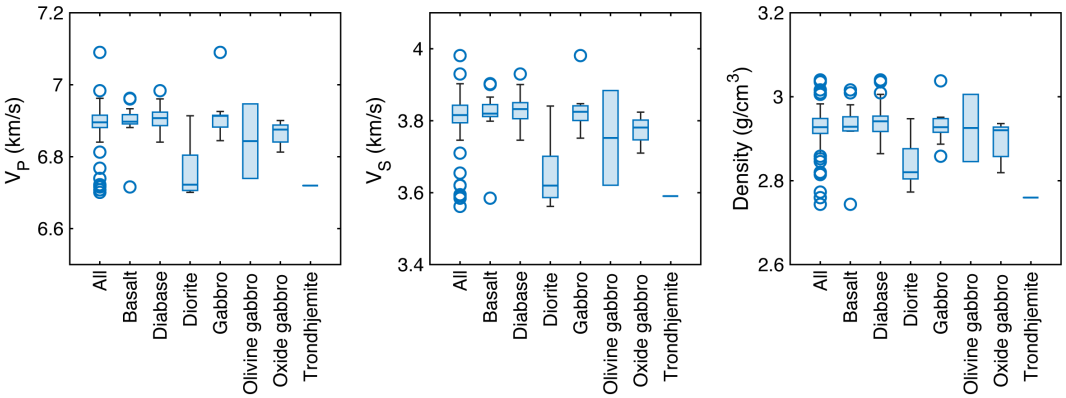

Figure 2.14 Comparison of calculated porosity-free velocities and density for each lithology. Box plots show the medians (blue horizontal bars), the 25th to 75th percentiles (boxes), whiskers extending to the extreme nonoutlier data, and outliers (circles). We used the medians of each lithology for crack density inversion of laboratory data from Hole GT3A and used the medians of all data for the inversion of logging data from Hole 1256D.

Figure 2.15 shows the depth variations of calculated crack density, aspect ratio, and crack porosity. The modeled velocities and resistivities broadly agree with the measured data used as input for inversions (Figure 2.16). Most of the samples show crack densities ranging from 0 to 1, whereas some samples yield crack densities > 1. Except for such high-crack density samples, the mean crack density tends to slightly decrease across the dike–gabbro transition. Aspect ratio varies widely from 10^{-4} to 10^{-1} and shows no clear depth trend. These values are consistent with those estimated from high-pressure experiments on mafic rocks collected from the Oman ophiolite (Hatakeyama et al., 2021). The calculated crack porosity typically ranges from 0.01% to 3% and shows a decrease across the dike–gabbro transition zone. Although this depth trend is consistent with the depth trend of bulk porosity (Figure 2.7a), the crack porosities determined from the joint inversion tend to be ~1% lower than the bulk porosities, suggesting the presence of spherical pores (i.e., equant pores). Indeed, microstructural obserations using high-resolution µCT imaging suggest that some samples contain both thin cracks and rounded pores (Figure 2.17). Although it is challenging to estimate the effects of equant pores on the elastic and electrical properties of the samples

because they are nearly insignificant in comparison to those of thin cracks (Fortin et al., 2011; Kachanov, 1994), ignoring their effects could result in an underestimation of porosity.

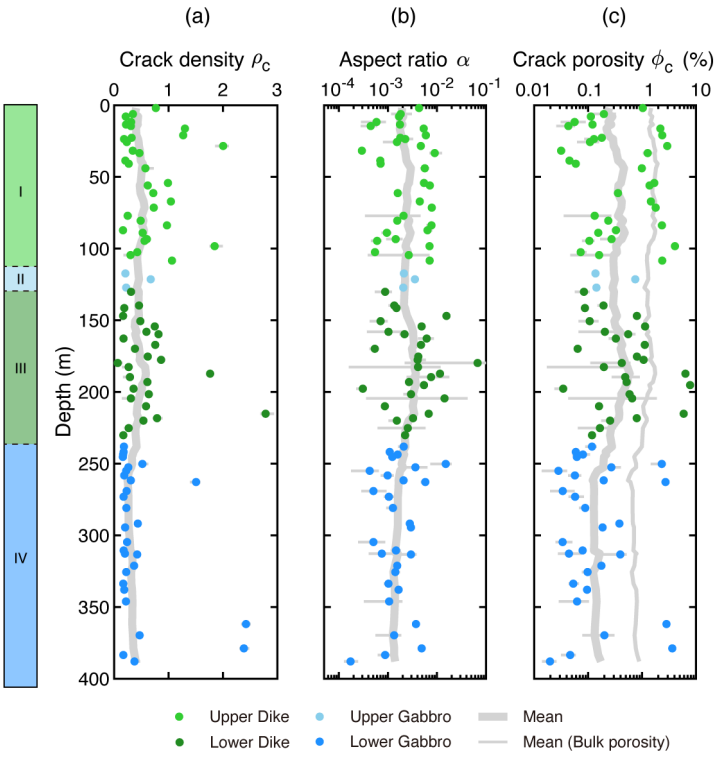

Figure 2.15 Depth variations of (a) crack density, (b) aspect ratio, (c) crack porosity, that were inverted from the measured elastic wave velocities and electrical resistivities. The data represent the mean values in three orthogonal orientations, and the bars indicate the variations in the measurement directions. Bold gray lines represent the moving mean values over 20 data points.

Although the assumption of non-interactions between cracks may be valid for crack densities below 0.5 for cracked effective medium model (Fortin et al., 2007; Guéguen & Kachanov, 2011; Schubnel & Guéguen, 2003), some samples yield high crack densities >1, which results in high crack porosities >3%. One possible cause of this high crack density and porosity is a high degree of fracturing that is possibly associated with brittle failure (Akamatsu et al., 2021; Paterson & Wong, 2005). Another possible cause may be the uncertainty of the crack-free parameters. The grain densities of our samples vary more than those calculated from the mineral compositions used for the determination of crack-free elastic moduli (Figure 2.14). This suggests that some of our samples may have unique mineral compositions and hence the crack-free parameters.

The microstructural characteristics of cracks are quantitatively estimated from the joint

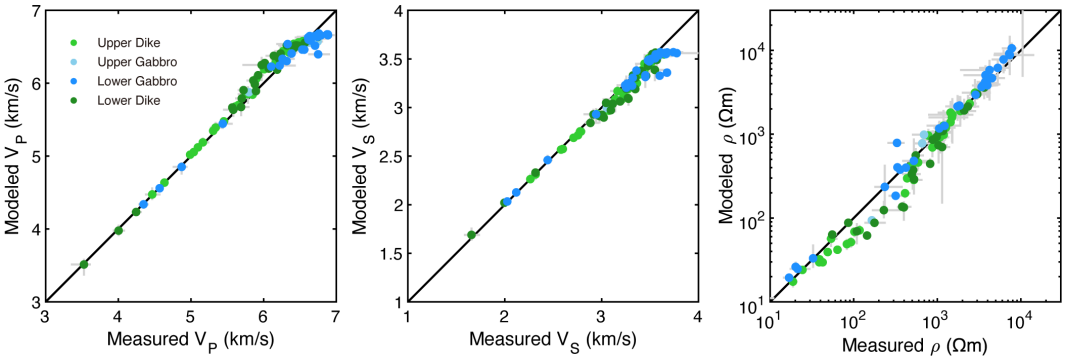

Figure 2.16 Comparison of the modeled velocities and resistivities with the experimental values.

inversion using elastic wave velocity and electrical resistivity. However, it should be noted that our model of electrical resistivity has some large uncertainties, in particular for low crack density regime near the percolation threshold. The percolation threshold ($p = 1/3$) is resulted from a simple Bethe lattice model whose coordination number is four (Guéguen & Palciauskas, 1994), and the probability of crack interconnection is estimated assuming penny-shaped cracks with homogeneous distribution. Thus, the critical crack density of ~0.13 should be regarded as an approximated value (Guéguen & Schubnel, 2003), and these assumptions and approximations possibly result in the large uncertainty on the crack density.

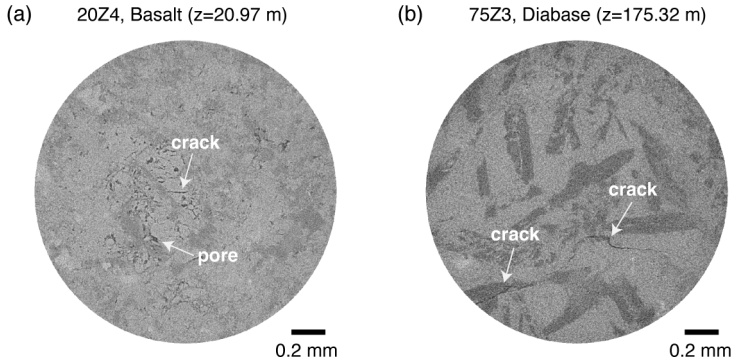

Figure 2.17 Cross-sections of μCT images of (a) 20Z-4 and (b) 75Z-3 with a resolution of ~2 μm. Cracks and spheroidal pores are indicated by white arrows.

2.4.3 Implications for in situ geophysical properties of oceanic crust

Combining the effective medium model and the percolation model, the elastic and electrical properties of oceanic crustal rocks measured in laboratory can be related to crack density and aspect ratio. Meanwhile, whereas our data were measured under ambient conditions, in

situ geophysical data obtained in oceanic crust must include various external factors such as pressure and temperature. To understand the potential effects of in situ conditions on seismic and electrical properties, we performed joint inversion using the proposed cross-property relationship to the sonic velocities and electrical resistivity obtained at IODP Hole 1256D. Logging measurements in Hole 1256D have provided downhole physical properties, including P- and S-wave velocities, electrical resistivity, and temperature down to the lowermost parts of the sheeted dike complex in a superfast spreading segment of the Cocos plate (Teagle et al., 2006). Sonic velocities at depths 250–1200 m and 1076–1422 m were measured at 1–14 kHz using the Schlumberger Dipole Sonic Imager during IODP Expedition 309 and 312, respectively (Guerin et al., 2008; Teagle et al., 2006). Deep resistivity data from the Dual Laterlog was measured during IODP Expedition 312 (Teagle et al., 2006). Temperature at depths 148–1455 m was acquired during IODP Expedition 335.

Crack density, aspect ratio, and crack porosity were calculated by joint inversion using the 25 m average values of sonic velocities and resistivities. Cracks were postulated to be fully saturated with seawater, and the fluid conductivity at each depth was estimated from the temperature log as (Becker et al., 1982; Key et al., 2012):

$$\sigma_{\text{fluid}} = 3 + \frac{T}{10}, \tag{2.18}$$

where T is the temperature (°C). The electrical conductivity of the solid phase was taken as 2×10^{-5} S/m. The crack-free velocities were taken to be $V_{\text{P}} = 6.90 \pm 0.06$ km/s and $V_{\text{S}} = 3.82 \pm 0.08$ km/s, based on the first, second, and third quartile values of of those calculated from the mineral abundances of Hole GT3A.

The results of joint inversion of Hole 1256D are shown in Figure 2.18. The forward solutions via the effective medium theory (EMT) and percolation model (solid lines in Figure 2.18a–c) well agree with the logging data used as input for inversions. For any crack-free velocities, crack density systematically decreases with depth approaching the percolation threshold (~0.13) at depths greater than ~1200 m, meaning that the connectivity of crack network decreases toward the deepest parts of the sheeted dike (Figure 2.18d). These decreases in crack density and connectivity can be the cause of the abrupt and large decrease in logging resistivity at the base of the sheeted dike complex. Aspect ratio and crack porosity show no clear depth trend down to the depths of ~1000 m for any crack-free velocities (Figure 2.18e, f). However, at the deeper parts of the hole, the aspect ratio and crack porosity begin to markedly decrease with depth for relatively high crack-free velocities, whereas those for low

crack-free velocities tend to slightly increase or do not vary markedly. Although the accurate solutions of the aspect ratio and hence crack porosity were not obtained at the deepest parts of the hole, possibly due to the less sensitivity of the aspect ratio to the elastic wave velocity in low-crack density regime, this suggests that the assumption of the crack-free velocity and hence mineral compositions can affect the inversion results at low crack density close to the percolation threshold. As mentioned above, however, care should be taken that there are also large uncertainties in the percolation threshold ($\rho_c \sim 0.13$) resulted from the simple geometric assumptions.

Whereas the range of in situ crack density is similar to that of the laboratory samples from Hole GT3A, its depth trend differs somewhat from those of the laboratory data, whereby the crack density of our samples does not change substantially in the sheeted dike sequence (Figure 2.15). The systematic decrease in crack density of Hole 1256D could be caused by the closure of cracks owing to elevated in situ effecive pressure within the oceanic crust. One could expect that the application of effective pressure corresponding to in situ depth to our laboratory data from Hole GT3A results in the closure of thin cracks, leading to further systematic increase in elastic wave velocities and electrical resistivity with increasing depth, as shown in the logging measurements at Hole 1256D. It should be noted, however, that another geometry of pore network, such as equant pores and tubes, may contribute to electrical conduction even under high pressure such that the thin cracks are completely closed (Pimienta et al., 2017). Alternatively, it may reflect that the cracks are sealed with secondary minerals due to the hydrothermal circulation prevailing at greater depths (Wilkens et al., 1991).

Compared with porosity estimated from Archie's law with different cementation exponents, the calculated crack porosity is in good agreement with that inferred from $m = 1.5$. However, there are some discrepancies at depths where the crack connectivity starts to decrease. This implies that the cementation exponent may change with depth, possibly related to the crack connectivity. Although electrical resistivity observed in oceanic crust is often interpreted with Archie's law (e.g., Carlson, 2010; Chesley et al., 2021; Schwalenberg et al., 2017; Swift et al., 2008), the transformed porosity is strongly dependent on the choice of cementation exponent. Our results suggest that care must be taken in choosing proper coefficients when using Archie's law, especially at depths where crack density is relatively low.

The wavelength of the sonic waves used for logging measurements is usually a few meters, which is much longer than that of ultrasonics used for laboratory measurements. Thus,

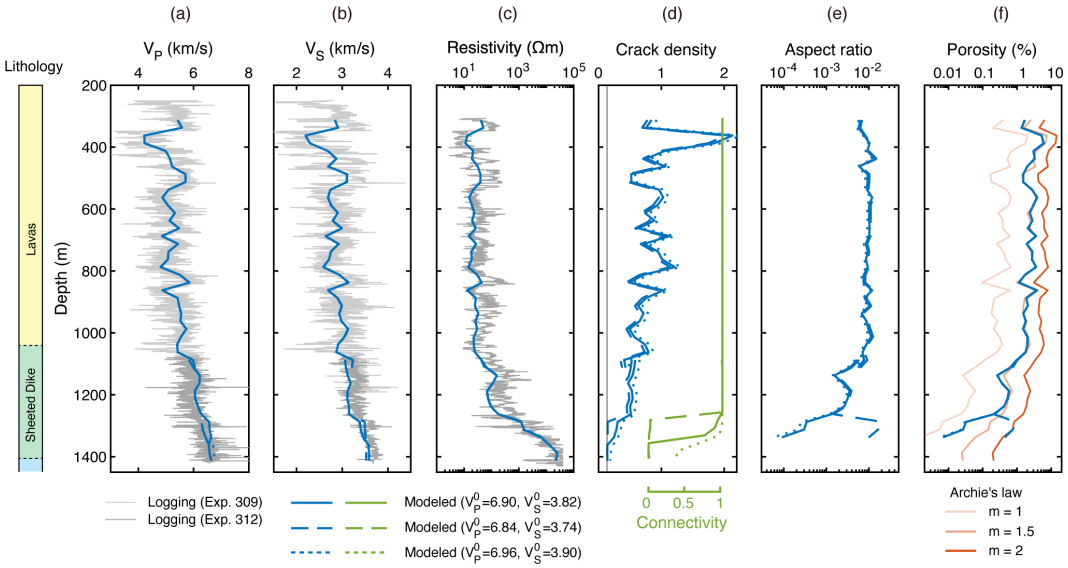

Figure 2.18 Results of joint inversion of sonic velocities and electrical resistivity obtained by borehole logging measurements at Hole 1256D. (a–c) Downhole plots of P- and S-wave velocities, and electrical resistivity logs (gray lines). Blue lines denote best fit values by joint inversion. The crack-free velocities were taken to be $V_P = 6.90 \pm 0.06$ km/s and $V_S = 3.82 \pm 0.08$ km/s. The fluid conductivity at each depth was estimated from the temperature log using Equation 2.18. The electrical conductivity of the solid phase was taken as 2×10^{-5} S/m. (d–f) Calculated crack density, aspect ratio, and crack porosity. Porosities estimated from Archie's equation using different cementation exponents are plotted for comparison (red lines).

velocities measured by borehole sonic logging include the effects of relatively large-scale cracks (Karato, 1983), possibly measuring a few meters in length and a few millimeters or less in width. The estimated crack densities and aspect ratios for Hole 1256D possibly include the characteristics of such large-scale cracks. The large-scale cracks can dominantly control the fluid flow in the oceanic crust, because rock's permeability depends strongly on the size of cracks (e.g., Guéguen & Dienes, 1989; Walsh & Brace, 1984). The permeability at the scale of in situ oceanic crust such as Hole 1256D could be much larger than that measured in the laboratory. Indeed, packer measurements using boreholes usually yield a permeability that is several orders of magnitude larger than that measured in the laboratory (Guéguen et al., 1996), and the large-scale permeability of Hole 1256D, that were estimated from the distribution of hydrothermal veins preserved in the drilled cores, has been shown to be much larger than the permeability of mini-core samples (Gilbert et al., 2018; Gilbert & Bona, 2016). However, our calculations show that the crack connectivity rapidly decreases in the sheeted dike complex. This implies that current fluid flow away from the ridge axis due to the networks of large-scale cracks may not be prominent in the deeper parts of the oceanic crust near Hole 1256D.

Whereas the effective medium model postulates a situation where fluid pressure differs from crack to crack, at sufficiently low frequency the pore fluid pressure can equilibrate between cracks within the representative elementary volume, because there is sufficient time for local fluid flow to occur, although macroscopic fluid flow does not take place over a scale of the wavelength (Guéguen & Kachanov, 2011). In such a case, elastic wave velocity should be evaluated by macroscopic poroelasticity theory which assumes pore pressure equilibration within each representative elementary volume (Fortin & Guéguen, 2021). The frequency at which the effect of pore pressure relaxation becomes prominent is typically $\ll$ 1 kHz (Fortin & Guéguen, 2021), whereas the frequency of sonic logging measurements at Hole 1256D was 1–14 kHz (Swift et al., 2008). This implies that the sonic measurements can be interpreted with the effective medium model. However, when extrapolating the cross-property relationship to data obtained by seismological surveys with a much lower frequency range (~10 Hz), the effect of pore pressure equilibration should be accounted for.

Field-scale geophysical surveys, including seismological and electromagnetic observations, have been recently conducted at various tectonic settings of oceanic lithosphere (e.g., Chesley et al., 2019, 2021; Fujie et al., 2018). Although our measurements and analysis have some uncertainties that should overcome, the proposed cross-property relationship between elastic wave velocity and electrical resistivity of oceanic crustal rocks can provide insight into the

quantitative interpretation of geophysical data from oceanic crust at various scales.

2.5 Conclusions

We measured P- and S-wave velocities and electrical resistivity of cubic samples collected from Hole GT3A of the Oman Drilling Project. Elastic wave velocity and resistivity tend to increase from the sheeted dike complex to the underlying gabbro sequence. By using an effective medium theory and a fluid flow model for cracks based on statistics and percolation theory, the variation in the electrical and elastic properties can be interpreted in terms of crack density and aspect ratio. To attempt to interpret in situ geophysical data in oceanic crust, we perfomed the joint inversion using sonic velocities and electrical resistivity obtained by logging measurements at IODP Hole 1256D. As a result, the depth variations of sonic velocities and electrical resistivity can be interpreted by systematic decrease in crack density and aspect ratio, suggesting that the crack network may be broken at the deeper parts of the oceanic crust. Our experimental data and analysis suggest that the physical properties of oceanic crust can be interpreted using the same model at both laboratory and in situ scales.

Chapter 3

Heterogeneity of crack distribution in oceanic crust inferred from shipborad MSCL data from the Oman Drilling Project

3.1 Introduction

The presence of subsurface water can be estimated from seismic observations because the fluid filling the pore space can readily modify the rock's elastic properties (Guéguen & Palciauskas, 1994). To investigate the distribution of pore water in the oceanic lithosphere, many seismological surveys have been conducted at various tectonic settings, and the seismic velocity structures have been obtained in particular for subduction zones (e.g., Audet et al., 2009; Eberhart-Phillips et al., 2017; Fujie et al., 2013; Kato et al., 2010). The seismic waves used for the explorations typically have a frequency of 1–10 Hz, which corresponds to a wavelength of tens–to–hundreds of meters. Therefore, the seismic structures obtained from those surveys should reflect macroscopic structures on such large scales. When interpreting the elastic properties of a rock, the assumption that the rock is homogeneous at the macroscopic scale allows various theoretical models, such as effective medium theory (Kachanov, 1994; Kuster & Toksöz, 1974; O'Connell & Budiansky, 1974; Takei, 2002) and poroelastic theory (Gassmann, 1951), to be applied. For this reason, it is often assumed that the pore structure at the macroscopic scale can be represented by the representative elementary volume (i.e., REV,

Figure 3.1), in which the microstructure is determined by laboratory ultrasonic measurements.

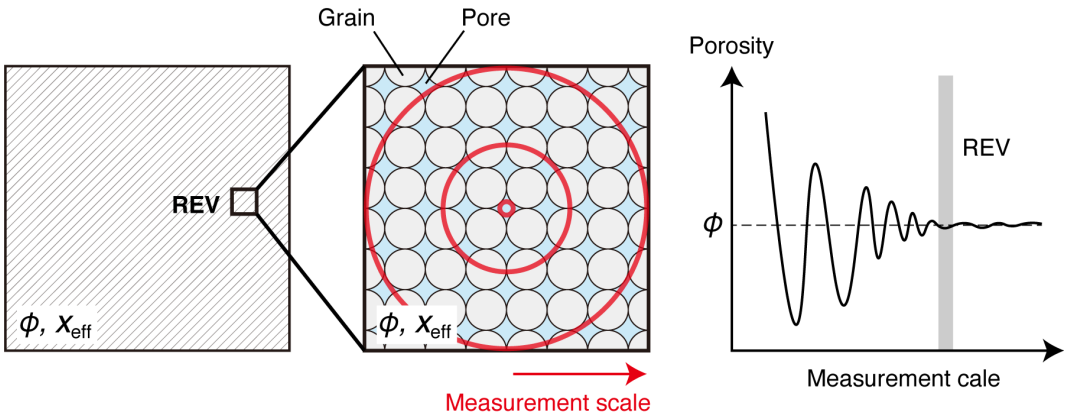

Figure 3.1 Schematic concept of Representative Elementary Volume (REV). Statistically homogeneous medium with porosity ϕ and the effective physical property x_{eff} (left). The macroscopic porosity and physical properties can be represented by those of the REV (middle). The porosity and physical property within the REV vary with measurement scale and exhibit a plateau, which is defined as REV (right).

When porous/cracked rocks are saturated with fluid, the loading associated with the wave propagation causes a pore pressure gradient in the pore network (Mavko et al., 2020). The pore pressure is diffused by fluid flow, which is referred to as wave-induced fluid flow (i.e., WIFF). The effective elasticity of the fluid-saturated rocks depends on the rate of loading of a REV as compared with the rate of pore pressure diffusion across the REV, meaning that the elastic wave velocity depends on the frequency (Guéguen & Kachanov, 2011). At high frequencies, such as ultrasonic velocity measured by laboratory measurements, the fluid flow has no time to take place within a given REV during the wave propagation, so the pore pressure within the REV is different from crack to crack. In this case, the elastic properties measured on this rock are referred to as "unrelaxed" moduli. The unrelaxed moduli can be modeled by effective medium theory, which postulates non-uniformity of pore pressure within REV (e.g., Kachanov, 1994). At lower frequencies, such as sonic velocity used for borehole logging and seismic velocity, there is enough time for fluid flow to occur between cracks, and the pore pressure can be equilibrated on the scale of the REV. In this case, the elastic properties measured on this rock are referred to as "relaxed" moduli, which is within the validity range of the concept of poroelastic theory. Nevertheless, there is no time for fluid flow to take place over the scale of the REV, and the pore pressure varies between REVs at the macroscopic scale. This situation corresponds to the "undrained condition" of poroelastic theory, and the undrained elastic moduli can be predicted by Gassmann's equations (Gassmann, 1951).

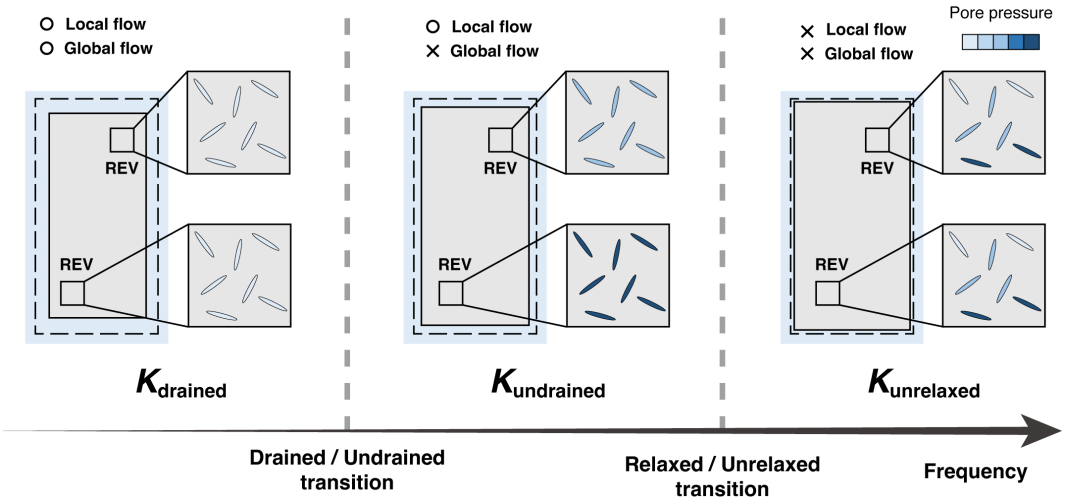

Figure 3.2 Schematics of drained (left), undrained (middle), and unrelaxed conditions (right). The elastic moduli of each condition are related to the relationship between the rate of wave-induced loading (i.e., frequency) and wave-induced fluid flow (i.e., WIFF) within REV.

These conventional interpretations implicitly assume that the REV at the scale of seismic wavelength is on the millimeter scale, as determined for the laboratory samples. This assumption may be valid for certain rock types with homogeneous mineral combinations, grain size and geometry, and pore structures, such as porous sandstone. However, for cracked crystalline rocks such as basalt and gabbro, which make up the plutonic layers of the oceanic crust, it is unclear whether the REV determined by the laboratory measurements can be applied to the wavelength scale of seismic waves. Indeed, many laboratory studies using discrete core samples originating from the seafloor have exhibited a markedly wide range of variations in physical properties and crack characteristics, even for the samples collected from similar depths and lithologies (Gilbert & Salisbury, 2011; Hatakeyama et al., 2021; Karato, 1983; Violay et al., 2010). This may suggest that the crack distribution within the oceanic crust is somewhat heterogeneous and has a larger REV than the conventional interpretations. The scale of REV can greatly affect the interpretation and prediction of the pore water pressure conditions and hence elastic constants that the observed seismic velocities "see". To quantitatively evaluate the REV that represents microcrack structure in the oceanic crust, it is essential to understand how microscopic physical properties spatially vary on a macroscopic scale. However, as there has been no continuous drilling into the plutonic sequence of the oceanic crust, comprehensive measurement of their physical properties is lacking.

Ophiolites, which are fragments of ancient oceanic lithosphere that have been tectonically

obducted onto continental margins, provide us with opportunities to obtain samples derived from the oceanic lithosphere. Samail ophiolite is the most extensive and best-exposed cross-section of the oceanic lithosphere, extending complete sections from sediments and pillow lavas to mantle peridotite sequences from the crust to mantle (Nicolas et al., 2000). Recently, the International Continental Drilling Program (i.e., ICDP) Oman Drilling Project sampled continuous cores comprising the crustal section to the mantle section of the Samail ophiolite, with a recovery rate of ~100% (Kelemen et al., 2020a). The recovered cores were systematically described and analyzed onboard in the laboratory of the drilling vessel Chikyu, with preliminary data, including fundamental physical properties, having been reported recently (Kelemen et al., 2020a). Those preliminary data include whole-round multisensor core logger (MSCL-W) data, as well as data measured for individual discrete samples taken from the cores. The MSCL-W (GEOTEK Ltd.) continuously measures various physical properties of the drilled cores, including P-wave velocity measured at every 4 cm interval with ultrasonic transducers. Such continuous P-wave velocity data obtained for the core samples from the crustal sections of the Samail ophiolite is ideal for assessing the heterogeneity of crack distribution in the oceanic crust.

In this study, we analyzed the depth variation of P-wave velocity data from the MSCL-W measurements to evaluate the spatial heterogeneity of crack distribution and REV in the crustal section of the Samail ophiolite. Based on the estimated REV, we discussed the validity of theoretical models for the interpretation of seismic velocity and the potential influence of microcracks on macroscopic elastic properties.

3.2 Core samples and MSCL-W measurements

The Oman Drilling Project obtained continuous core samples from the upper oceanic crust to the uppermost mantle in the Oman ophiolite, with a recovery rate of ~100%. Hole GT3A continuously sampled the transition zone from the sheeted dike to the underlying gabbro of the crustal sections of the Oman ophiolite. The total length of the hole is about 400 m and is composed mainly of basalt, diabase, and gabbro (Figure 3.3a). Shipboard descriptions logged the downhole variations in total alteration intensity and relative abundances of secondary minerals for 701 intervals (Kelemen et al., 2020d). Alteration intensity is highly heterogeneous downhole and varies strongly over short depth intervals, without any clear correlations with depth and lithology (Figure 3.3b). Total alteration logged ranges from 10%–100%, suggesting that the whole core sections are moderately altered. During logging, the main alteration

minerals were identified as albite, amphibole, chlorite, and epidote/clinozoisite. These four minerals represent at least 70% of total secondary mineralization in all but five alteration intervals. Other minerals occurring locally at >5% include quartz, zeolite, and, rarely, pyrite and Fe oxyhydroxide.

The recovered core samples were carefully reconstructed and shrink-wrapped by core liners and run through MSCL-W measurements before the core splitting. For Hole GT3A, whole-round magnetic susceptibility, natural gamma ray, non-contact resistivity, gamma ray attenuation density, and P-wave velocity were continuously measured using the MSCL-W. Of these data, we focus on P-wave velocity, which is highly dependent on microcrack characteristics and can be inverted in terms of crack geometrical parameters. P-wave velocity V_{P} is defined by the time required for a compressional wave to travel a set distance as follows:

$$V_{\mathrm{P}} = \frac{d}{t_{\mathrm{core}}}, \tag{3.1}$$

where d is the path length of the wave across the core, and t_{core} is the travel time through the core. P-wave velocity transducers on the MSCL-W system measure the total travel time of the compressional wave between the transmitter and receiver. The wave travels horizontally across the whole core and core liner. The total travel time observed is given as the sum of several components:

$$t_{\mathrm{total}} = t_{\mathrm{delay}} + t_{\mathrm{pulse}} + 2t_{\mathrm{liner}} + t_{\mathrm{core}}, \tag{3.2}$$

where t_{delay} is the time delay related to transducer faces and electronic circuitry, t_{pulse} is the delay related to the peak detection procedure, and t_{liner} is the transit time through the core liner. Assuming that the core is completely covered by the liner, the P-wave velocity of the core is calculated as follows:

$$V_{\mathrm{P}} = \frac{d_{\mathrm{cl}} - 2d_{\mathrm{liner}}}{t_{\mathrm{total}} - t_{\mathrm{pulse}} - t_{\mathrm{delay}} - 2t_{\mathrm{liner}}}, \tag{3.3}$$

where d_{cl} is the measured diameter of core and liner, and d_{liner} is the liner wall thickness. The components other than t_{core} are calibrated by measurement using a core liner filled with distilled water. For GT3A, V_{P} with a frequency of 500 kHz were measured every 4 cm under dry conditions. As the corresponding wavelength is about 4–12 mm, the observed velocity should reflect the pore structure at such a small scale. We assumed that the velocity measured at each point is the representative value of ± 2 cm of the point, as made for typical laboratory measurements.

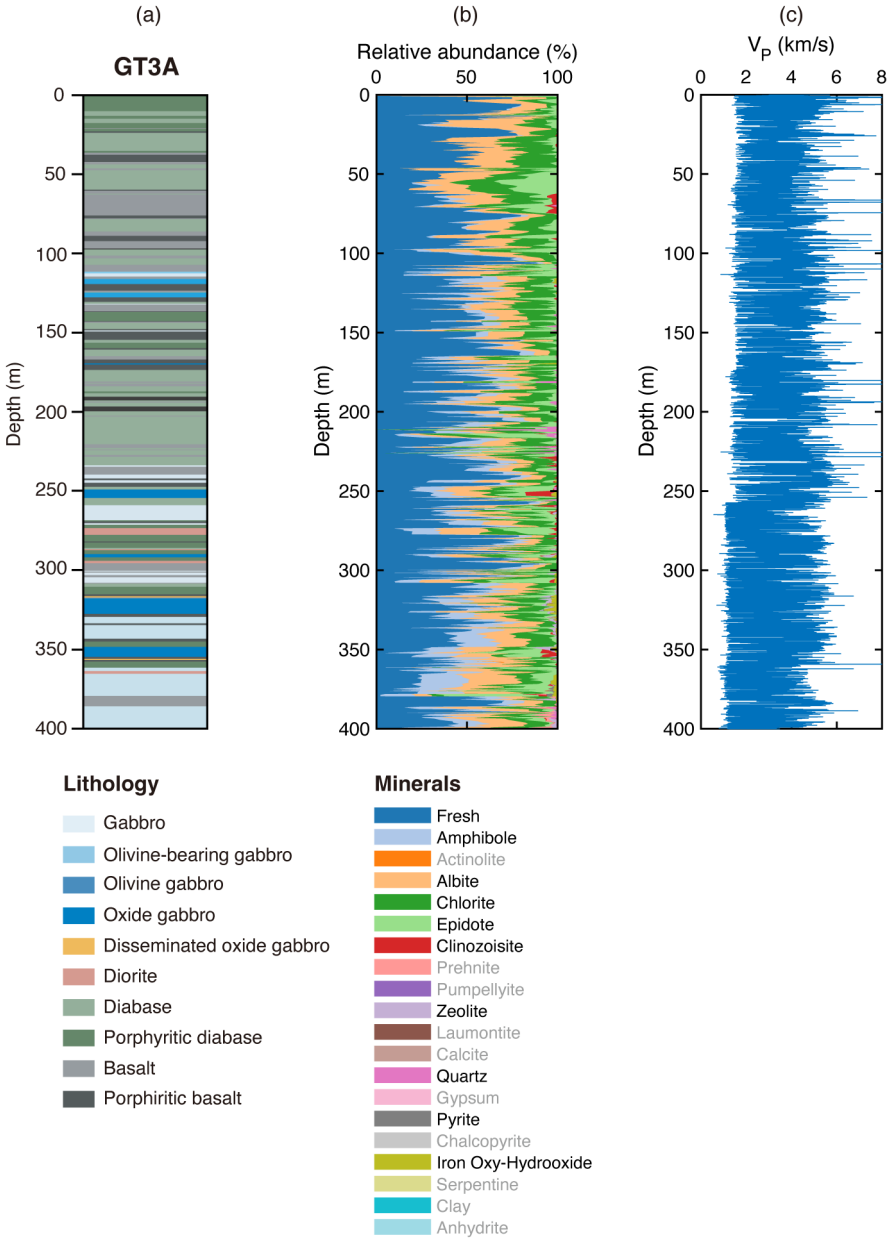

Figure 3.3 (a) Borehole stratigraphy of Hole GT3A. (b) Downhole variations in the relative abundance of secondary minerals that were visually determined during the shipboard descriptions (Kelemen et al., 2020d). (c) Downhole variations in P-wave velocity measured by the whole-round multi-scanner core logger (MSCL-W) system (Kelemen et al., 2020d).

Downhole variations in P-wave velocity are shown in Figure 3.3c. P-wave velocity also varies strongly over short depth intervals, ranging from ~2 km/s to ~7 km/s in almost all depth intervals. These variations in P-wave velocity reflect variations in the amount and geometry of cracks, which can be used to assess the spatial heterogeneity of crack distribution. However, the ranges of the measured V_{P} is much larger than those measured on the discrete samples of the same hole under dry conditions (Akamatsu et al., 2023. under review). This implies that the measured values contain substantial errors and uncertainties, possibly derived from the roughness of the surface topography of the cores. These measurement errors and uncertainties can lead to an overestimation of the true heterogeneity of P-wave velocity and crack characteristics. Therefore, it is necessary to remove these noises from the measured data and extract downhole variations in V_{P} and cracks that reflect the true heterogeneity.

3.3 Data preprocessing

3.3.1 Crack density

Elastic wave velocity of rock containing cracks can be related to crack density based on effective medium theory (e.g., Kachanov, 1994; Kuster & Toksöz, 1974; O'Connell & Budiansky, 1974; Shafiro & Kachanov, 1997; Takei, 2002). For a medium containing circular cracks whose centers and normals are oriented randomly, the crack density ρ is defined as:

$$\rho = \frac{Nc^3}{V}, \tag{3.4}$$

where c is the radius of the crack, and N is the total number of cracks in a representative elementary volume V which is elastically homogeneous (Guéguen & Kachanov, 2011). Given this definition, heterogeneity in terms of the amount of cracks can be directly evaluated by calculating the depth variations in the crack density. Assuming no interaction between cracks, the effective elastic moduli of a medium containing randomly oriented cracks under dry conditions (K_{d} and G_{d}) are given as:

$$K_{\mathrm{d}} = K_0 \left(1 + \frac{16(1-\nu_0^2)}{9(1-2\nu_0)}\rho\right)^{-1} \tag{3.5}$$

and

$$G_{\mathrm{d}} = G_0 \left(1 + \frac{16(1-\nu_0/5)(1-\nu_0)}{9(1-\nu_0/2)}\rho\right)^{-1}, \tag{3.6}$$

where ν is Poisson's ratio, and subscript 0 denotes the solid phase (Fortin et al., 2007; Kachanov, 1994). These equations allow the difference between the elastic wave velocity of crack-free rock and the measured velocities under dry conditions to be attributed to crack density. However, inverting crack density with these equations would yield overestimated crack density values, in particular for high crack density regime (>0.5), as the crack interactions are not taken into account (Guéguen & Kachanov, 2011; Pimienta et al., 2018). To account for the interaction between cracks, we applied the Differential Effective Medium (DEM) scheme, which can account for the crack interactions, to Equation 3.5. The DEM scheme consists of adding a few crack densities step by step (Le Ravalec & Guéguen, 1996). At each step, new effective elastic moduli are defined and used as a reference value for the solid phase constants in the next step. We set the number of calculation steps (iteration) to $N = 100$.

We estimated the elastic moduli of crack-free medium from mineral abundances (Figure 3.3b) using Voigt–Reuss–Hill (VRH) averages by assuming an isotropic medium (Mavko et al., 2020). The VRH average is given as:

$$M_{\mathrm{VRH}} = \frac{M_{\mathrm{V}} + M_{\mathrm{R}}}{2}, \tag{3.7}$$

where M_{V} and M_{V} are Voigt and Reuss averages, respectively, and correspond to upper and lower bounds on the effective elastic moduli of a mixture of grains. Each average is given as:

$$M_{\mathrm{V}} = \sum_{i=1}^{n} f^i M^i \tag{3.8}$$

and

$$\frac{1}{M_{\mathrm{R}}} = \sum_{i=1}^{n} \frac{f^i}{M^i}, \tag{3.9}$$

where f^i is the volume fraction of the ith phase and M^i is the bulk or shear modulus of the ith phase. At any given volume fraction of constituents, the effective modulus will fall between these bounds. The VRH average has been shown to give an accurate estimate of crack-free rock properties for oceanic rocks collected from the Samail ophiolite (Hatakeyama et al., 2021). In this study, we used the elastic properties of the minerals that are listed in Table Table 3.1. Note that we assumed that the unaltered phase, which is referred to as "fresh," comprises plagioclase and clinopyroxene in identical proportions because the modal abundances of such primary minerals were not logged during the shipboard descriptions.

Table 3.1 Elastic constants and densities of minerals used for the calculation of solid-phase properties

Mineral	K (GPa)	G (GPa)	Density (g/cm^3)	Reference
Plagioclase	75	34	2.68	Carmichael (2017)
Clinopyroxene	96	58	3.32	Hacker et al. (2003)
Amphibole	87	43	3.12	Brown & Abramson (2016)
Albite	54	28	2.62	Hacker et al. (2003)
Chlorite	76	28	3.16	Carlson & Miller (2004)
Epidote	106	61	3.40	Mavko et al. (2020)
Zeolite	47	28	2.25	Mavko et al. (2020)
Quartz	37	44	2.65	Carmichael (2017)
Pyrite	147	133	4.93	Mavko et al. (2020)

3.3.2 Noise removal

As mentioned above, the magnitude of the spatial variations in P-wave velocity and crack density inverted using a simple least-square method with Equations 3.5, 3.6 will be possibly overestimated due to the substantial measurement noise and uncertainties. Crack density and porosity of rocks are assumed to be somewhat continuously varying while spatially being heterogeneous. Here, we defined an intuitive evaluation function E that incorporates the effects of smoothing as follows:

$$E(\boldsymbol{V_P}, \boldsymbol{\rho}, \lambda) = \frac{1}{2}\sum_{i=1}^{n}(V_P^i - V_P(\rho^i))^2 + \frac{\lambda}{2}\sum_{i\sim j}^{n}(\rho^i - \rho^j)^2, \tag{3.10}$$

where n is the total number of the measured point; $\boldsymbol{V_P}$ and $\boldsymbol{\rho}$ are the respective sets of variables V_P and ρ for the measured point $i = 1, ..., n$; $\sum_{i\sim j}$ is the summation of all pairs of neigboring points. In the evaluation function, the first term indicates the reproducibility of the observation, whereas the second term indicates the spatial continuity of the crack density. The parameter λ fully controls the relative importance of reproducing the observational data to honor the continuity of the physical properties, and so this parameter is often referred to as a hyperparameter. Minimization of $E(\boldsymbol{V_P}, \boldsymbol{\rho}, \lambda)$ satisfies the requirements of both the reproducibility of the observed data and the spatial continuity of the physical variables. In other words, it is expected that distributions of P-wave velocity and crack density close to

the true distributions are recovered. However, the estimated distribution greatly depends on the choice of the hyperparameter, λ; therefore, it is necessary to choose an appropriate value.

Here, this study attempted to determine the appropriate λ value using synthetic data for crack density and P-wave velocity. First, a random walk based on a Gaussian distribution with known variance ($\sigma_\rho^2 = 0.05^2$) was used to prepare a one-dimensional true crack density distribution (Figure 3.4a). Assuming the crack-free elastic wave velocity of $V_{\mathrm{P}}^0 = 7.0$ km/s and $V_{\mathrm{S}}^0 = 3.8$ km/s, the distribution of the true P-wave velocity obtained for this crack density distribution was calculated from Equation 3.5 (blue line in Figure 3.4b). To simulate the potential errors and uncertainties in the observed P-wave velocity, another Gaussian noise with known variance ($\sigma_V^2 = 0.5^2$) was applied to the true values to produce a synthetic distribution of the observed P-wave velocity (red line in Figure 3.4b). Using this synthetic data, we performed the minimization of the evaluation function E for various values of λ so that the appropriate value of λ at which the estimated crack densities are closest to the true values can be obtained. Here, we explored λ that minimizing a root mean square error function given as:

$$\mathrm{RMSE} = \sqrt{\frac{1}{n}\sum_{i=1}^{n}(\rho^i_{\mathrm{estimated}} - \rho^i_{\mathrm{true}})^2}. \tag{3.11}$$

Figure 3.5 shows the calculated RMSEs as a function of λ. The minimum value is obtained at $\lambda = 169$. Estimates of crack density and P-wave velocity for this value are shown in Figure 3.6. The estimates (red line) are well consistent with the true values (blue line) than the distributions determined from the least-squares method without the term of the spatial continuity of the crack density (transparent red line).

According to the framework of Bayesian estimation based on the Markov Random Field (MRF) model applied to seismic velocity data (Kuwatani et al., 2014), it is known that the hyperparameter λ can be related to a ratio of the variance of the noise in the observed velocity and the variance of the change in the crack parameter between two adjacent points, which is given here as:

$$\lambda = \frac{\sigma_V^2}{\sigma_\rho^2}. \tag{3.12}$$

Based on this equation, the hyperparameter for the true crack density distribution is expected $\lambda = 100$, which is similar to that estimated from our synthetic data. Therefore, we consider that the crack density inversion using the evaluation function E is valid for the MSCL-W data, and $\lambda = 100$ will be used in the following calculations.

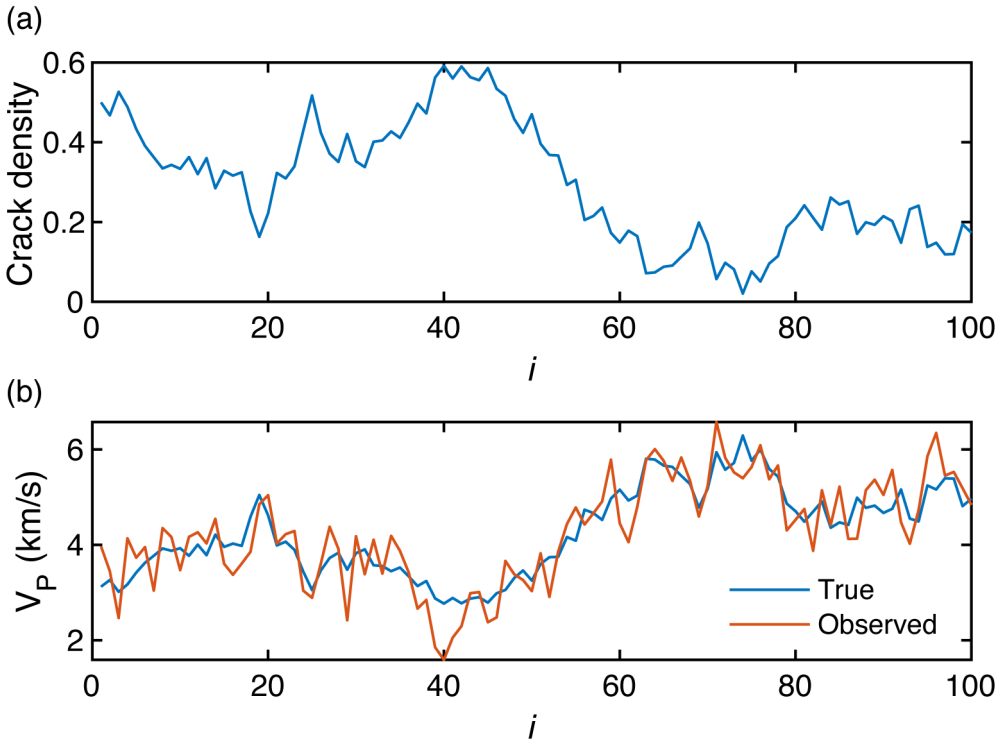

Figure 3.4 Synthetic data of (a) crack density and (b) P-wave velocity.

Figure 3.7a shows the downhole variations in the estimated V_P plotted with the raw V_P (gray line) and the crack-free velocities V_P^0 determined from the modal abundances. The estimated V_P seems to be well denoised. Figure 3.7b shows the downhole variations in the estimated crack density plotted with those of the discrete core samples taken from the same hole determined by laboratory measurements (open circles, Akamatsu et al.). The estimated crack densities are within the range of the discrete sample data, suggesting that the estimation is valid.

3.4 REV estimation

We estimated the scale of REV of the P-wave velocity and crack density based on a conventional deterministic approach, in which mean V_P and crack density were calculated for multiple moving windows as the size of the window increased (Costanza-Robinson et al., 2011). We used a one-dimensional moving window, in which the window length was increased systematically in top and bottom directions from the starting point. The mean P-wave velocity and crack density in each window length were calculated and plotted as a function of

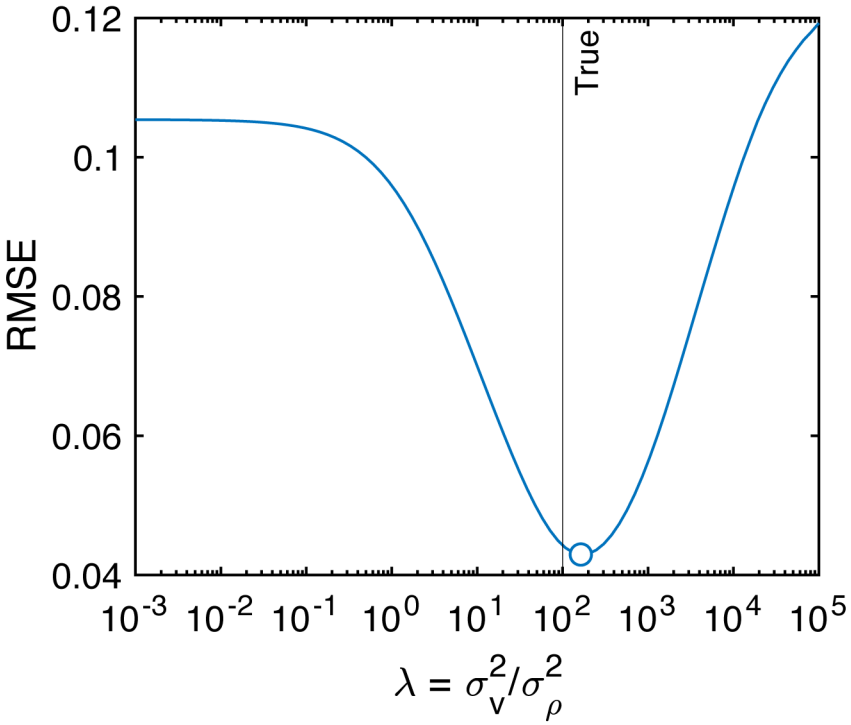

Figure 3.5 Calculated root mean square error (RMSE) as a function of the ratio between variances of observation noise and true crack density, which is referred to as a hyperparameter.

the window length, which is here referred to REV plot. Although we cannot directly evaluate the volumetric geometry of REV because our data is one-dimensional depth variation, we postulated the window length at which the REV plot exhibits a distinct plateau as the length of REV (L_{REV}) that characterizes the scale of REV, as analogous to the conceptual schematic shown in Figure 3.1. Here, L_{REV} was taken as the minimum window length at which the absolute value of the relative gradient error ϵ_g in the measured system variable, shown here for P-wave velocity and crack density, remained below 0.1:

$$\epsilon_g = \left| \frac{x^{i+1} - x^{i-1}}{x^{i+1} + x^{i-1}} \right| \frac{1}{\Delta L}, \tag{3.13}$$

where i refers to the window increment number and ΔL is the magnitude of the increment in the window length (Li et al., 2009). The REV criterion requires changes in the measured variable over a given length-scale increment to be relatively small proportional to the size of the increment, which relies on a subjective judgment regarding the magnitude of acceptable variation in the measured property and what constitutes a clear plateau. Here, the maximum window length was set to 50 m, and the window was moved from the top to the bottom of

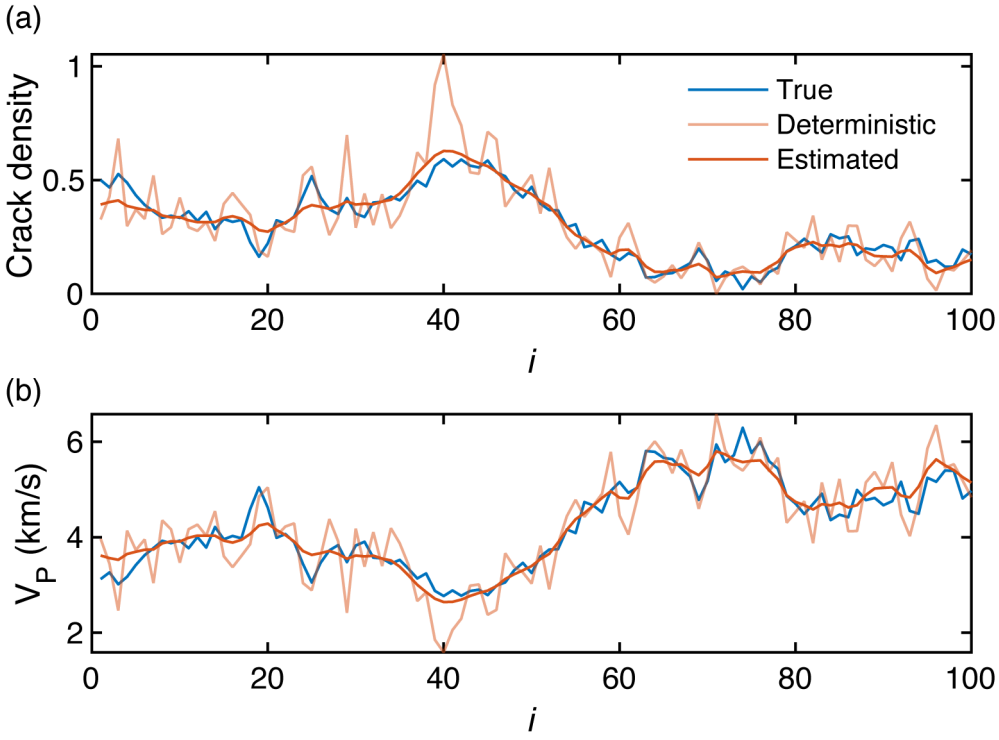

Figure 3.6 Estimated crack density and P-wave velocity using $\lambda = 100$ (red lines), plotted with those determined by the simple least-square method (deterministic).

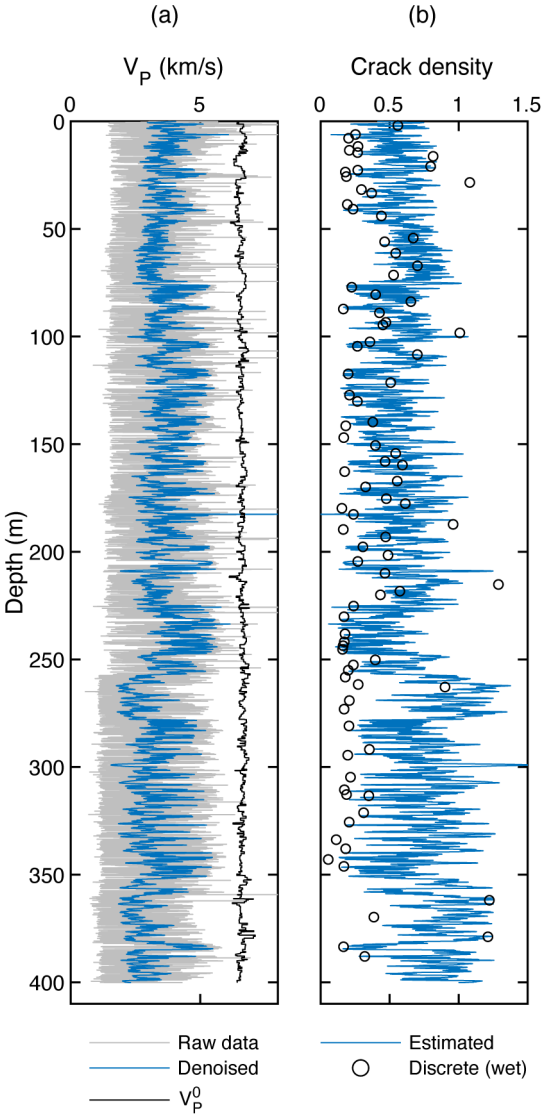

Figure 3.7 Downhole variations in (a) P-wave velocity and (b) crack density estimated by minimization of the evaluation function using $\lambda = 100$. The black line indicates crack-free velocities determined from the mineral abundances. Open circles denote crack densities that were estimated from the laboratory measurements on discrete cubic samples from Hole GT3A (for details, see Chapter 2).

the hole depths (~400 m) every 10 m depth. Namely, we performed the REV evaluation for 35 locations through the hole. Note that, the mean Vp was calculated as a harmonic mean as:

$$\frac{1}{V_{\mathrm{P}}^{i}} = \left\langle \frac{1}{V_{\mathrm{P}}} \right\rangle . \tag{3.14}$$

This corresponds to calculating Backus average, which represents the low-frequency limit of elastic wave velocity for isotropic medium (Mavko et al. 2020).

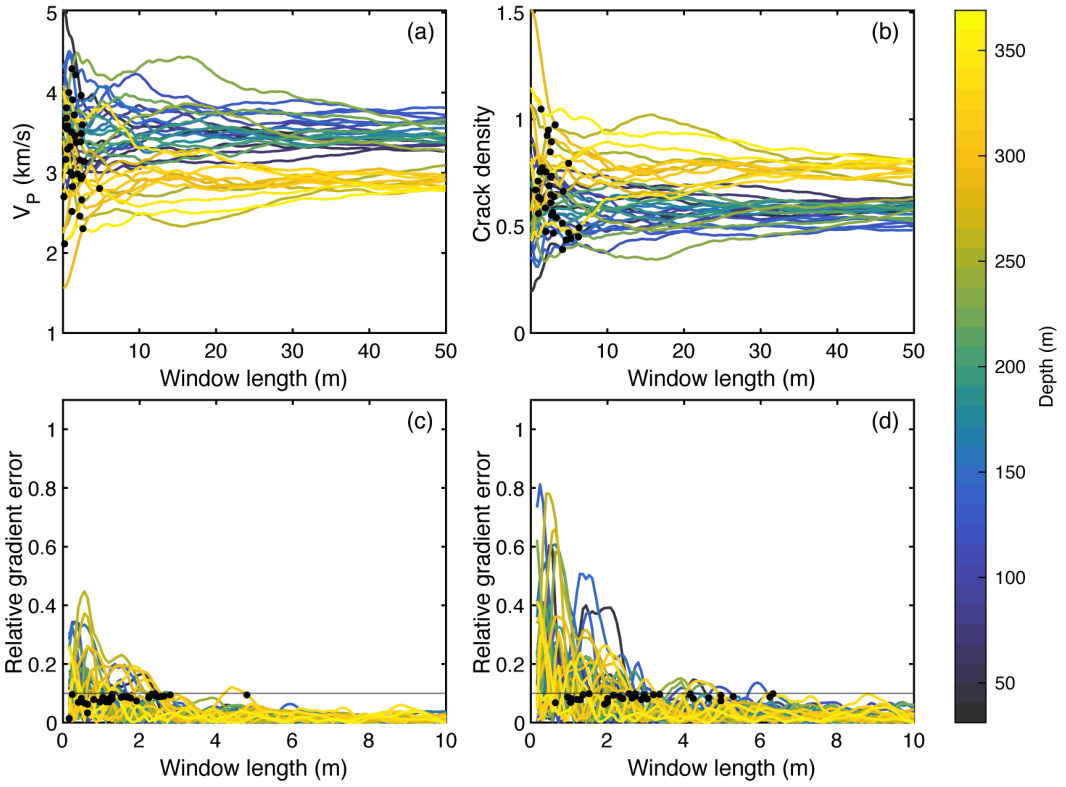

Figure 3.8 (a,b) Changes in mean P-wave velocity and crack density, and (c,d) the relative gradient errors as a function of the window length. Color represents the depth of the center of the moving window. Black dots indicate the L_{REV}.

Figure 3.8 shows the calculated mean V_{P} and crack density and the magnitude of relative gradient errors for those variables as a function of the window length. The color indicates each depth domain for the moving window. At small window size, erratic variations in both variables and ϵ_g were observed for incremental growth in window size, which is consistent with sub-REV scales Figure 3.1. At larger window sizes, mean V_{P} and crack density exhibited the characteristic REV plateaus, and the variability and magnitude of ϵ_g decreased well below the 0.1 REV criterion (black dots). The L_{REV} estimated using the $\epsilon_g < 0.1$ visually corresponded with our assessment of the beginning of the plateau in V_{P} and crack density,

suggesting that the criterion is reasonable. This behavior was observed in all cases, meaning that the crack distribution in Hole GT3A is homogeneous in the scale of 50 m regardless of the depth intervals. The estimated L_{REV} for V_{P} and crack density were 0.5–3 m and 1–5 m, respectively Figure 3.9. These values are significantly larger than the typical scale of the REV determined by laboratory ultrasonic measurements (Müller et al., 2010). This indicates that, although the microstructure of the pore space of oceanic crustal rock is homogeneous in the millimeter- to centimeter-scales, it can turn heterogeneous in larger scales up to the meter-scale, and then become homogeneous again in the tens of meter-scales. In other words, the REV that can represent the macroscopic physical properties, including seismic velocity with large wavelength (low-frequency), should be derived from the meter-scale crack distribution.

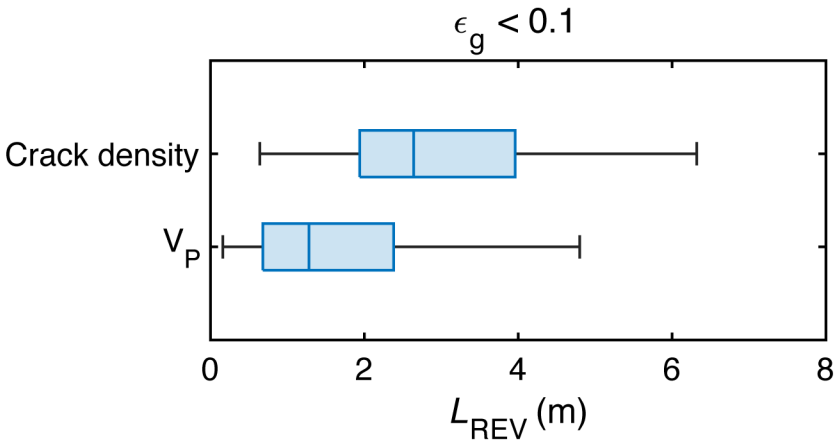

Figure 3.9 Boxplots of the length of REV (L_{REV}) for P-wave velocity and crack density that are determined using the criterion of $\epsilon < 0.1$.

3.5 Discussion

3.5.1 Is pore pressure within REV equilibrated or not?

Choosing an appropriate model to predict/interpret seismic velocity, which reflects the pore structure at the macroscopic scale, requires comparison with the rate of REV loading and the rate of WIFF across the REV (Guéguen & Kachanov, 2011). Therefore, we calculated the time for fluid flow to diffuse over the REV length estimated for crack distribution in Hole GT3A and investigated whether the pore pressure is equilibrated within the REV or not (i.e., relaxed or unrelaxed) for typical frequency ranges. The time required for the fluid to

diffuse over a distance L within a rock containing cracks and pores is calculated as:

$$\tau = \frac{\eta L^2}{K_d k}, \tag{3.15}$$

where η is the fluid viscosity, K_{d} is the drained bulk modulus, and k is the permeability (Guéguen & Palciauskas, 1994). The critical frequency at which the relaxed/unrelaxed transition f_{c} occurs can be obtained as an inverse of Equation 3.15:

$$f_c = \frac{1}{\tau}. \tag{3.16}$$

If the frequency of the elastic wave is greater than f_{c}, fluid diffusion in the length L is slower than the rate of loading, resulting in unrelaxed conditions; if the frequency is less than f_{c}, fluid diffusion is faster than the rate of loading, resulting in relaxed (but unrained) conditions. According to the crack percolation theory by Guéguen & Dienes (1989), the permeability of rock containing randomly oriented cracks is given as:

$$k = \frac{8w^2}{15F}, \tag{3.17}$$

where w is the crack aperture, and F is the electrical formation factor, which is a parameter representing the geometry of the crack network. We used the values of the formation factor reported by Akamatsu et al., who measured electrical resistivity under brine-saturated conditions for the 94 discrete core samples from Hole GT3A. Assuming the typical value of crack aperture of 1 µm yields the crack permeability of Hole GT3A ranging from 0.31×10^{-16} m^2 to 9.26×10^{-16} m^2 with the mean value of 1.72×10^{-16} m^2. The drained bulk modulus K_{d} was set to 13.6 GPa, as obtained from the estimated V_{P} (Figure 3.7a). The fluid viscosity η is taken to be 10^{-4} Pa.s, which is plausible for in situ crustal conditions (Pimienta et al., 2018).

Figure 3.10 shows the critical frequencies calculated from the possible range of permeability as a function of the REV length (hatched blue line). Under conditions above the blue line, the pore pressure within the REV is unrelaxed where the effective medium theory can be applied, whereas, under conditions below the blue line, the pore pressure within the REV is relaxed (but undrained) where the poroelastic theory can be applied. Note that the red-colored region denotes the range of wavelengths greater than REV, in which no effective elastic constants can be obtained because the rock cannot be considered a homogeneous medium. The remaining region is primarily divided into five domains, denoted by A–E. The domains A, B, and C are

recognized as situations based on the conventional scale of REV, where laboratory ultrasonic velocity (10^5–10^6 Hz), borehole sonic velocity (10^3–10^4 Hz), and seismic velocity (10^0–10^2 Hz) "see" the millimeter- to centimeter-scale microstructure extending homogeneously over the scale of each wavelength. The ultrasonic velocity reflects unrelaxed elastic moduli, whereas the seismic velocity reflects relaxed moduli. The sonic logging velocity coincides with the transition between unrelaxed and relaxed conditions. However, our analysis using MSCL-W data of the continuous core sections from Hole GT3A suggests that the actual scale of REV in terms of crack distribution can be up to the meter-scale in the oceanic crust. Based on those estimates, the pore pressure conditions within the REV in the oceanic crust against the sonic and seismic velocities can be expressed as the domains D and E, respectively. This suggests that the fluid flow cannot follow the rate of the loading and hence the observed velocities reflect the unrelaxed elastic moduli even for the seismic frequency, inconsistent with the conventional interpretation of seismic velocity.

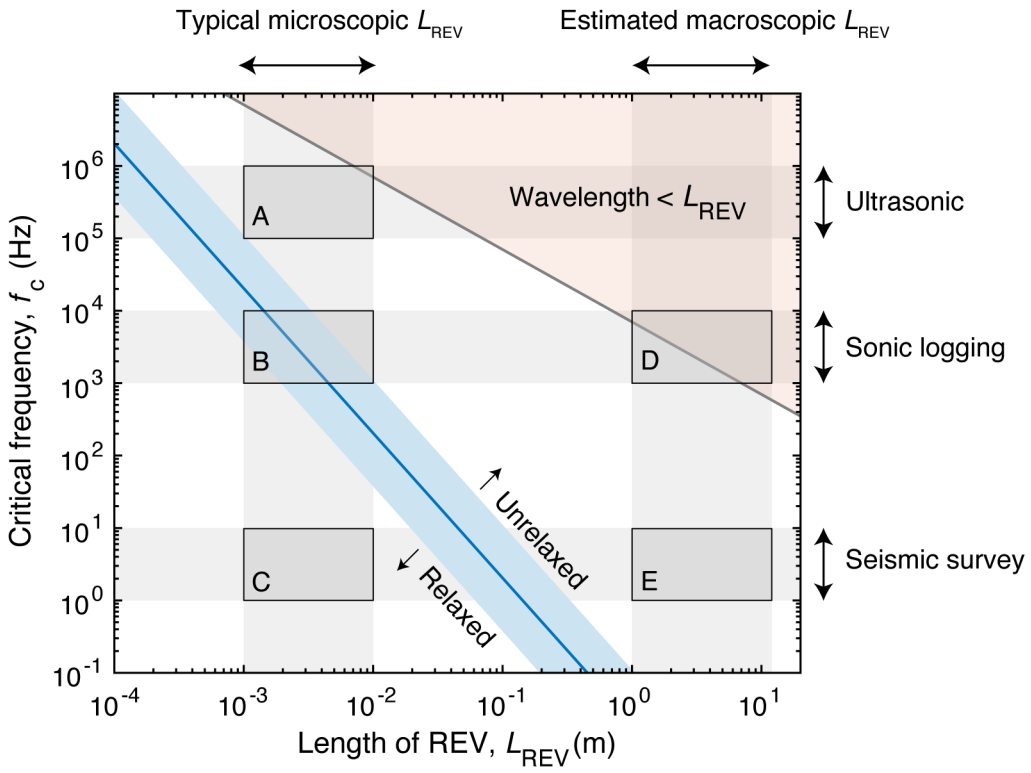

Figure 3.10 Critical frequency at which unrelaxed/relaxed transition occurs in a cracked rock as a function of the length of REV. The red-colored region denotes the range of wavelengths greater than REV. The remaining region is divided into five domains denoted by A–E, based on the L_{REV} and the typical frequencies.

3.5.2 Influence on prediction/interpretation of seismic velocity of oceanic crust

Based on the typical microscopic REV, the undrained conditions have been implicitly assumed for the prediction and interpretation of low-frequency elastic wave velocity (Fortin & Guéguen, 2021). The undrained elastic moduli (K_{ud} and G_{ud}) can be given by Gassmann's equation (Gassmann, 1951) as:

$$K_{\mathrm{ud}} = K_{\mathrm{d}} + \frac{\beta^2 K_{\mathrm{f}}}{\phi + (\beta - \phi)\frac{K_{\mathrm{f}}}{K_0}} \tag{3.18}$$

and

$$G_{\mathrm{ud}} = G_{\mathrm{d}}, \tag{3.19}$$

where K_{d} and G_{d} are the drained bulk modulus and shear modulus, respectively; ϕ is the porosity; K_{f} is the fluid bulk modulus; and β is the Biot's coefficient defined as:

$$\beta = 1 - \frac{K_{\mathrm{d}}}{K_0}. \tag{3.20}$$

Since the drained moduli can be calculated from Equation 3.5, the undrained moduli can be determined by the combined use of effective medium theory and Gassmann's equation (Le Ravalec & Guéguen, 1996).

On the other hand, based on the scale of REV estimated for crack distribution in Hole GT3A, the P- and S-wave velocities to be observed in the saturated oceanic crust by seismological surveys should reflect unrelaxed conditions. The unrelaxed elastic moduli of rock containing randomly oriented cracks (K_{ur} and G_{ur}) can be given by effective medium theory (Fortin et al., 2007; Kachanov, 1994) as:

$$\frac{K_0}{K_{\mathrm{ur}}} = 1 + \frac{h\rho}{1 - 2\nu_0}\left(1 + \left[\left(1 - \frac{\nu_0}{2}\right)\frac{\delta}{1+\delta} - 1\right]\right) \tag{3.21}$$

and

$$\frac{G_0}{G_{\mathrm{ur}}} = 1 + \frac{h\rho}{1 + \nu_0}\left(1 + \frac{2}{5}\left[\left(1 - \frac{\nu_0}{2}\right)\frac{\delta}{1+\delta} - 1\right]\right), \tag{3.22}$$

where the parameter h is a geometric factor for a penny-shaped crack and is expressed as

$$h = \frac{16(1 - \nu_0^2)}{9(1 - \nu_0/2)}, \tag{3.23}$$

and δ is a non-dimensional parameter for a penny-shaped crack defined by

$$\delta = \frac{\pi E_0 \alpha}{4(1-\nu_0)} \left(\frac{1}{K_\mathrm{f}} - \frac{1}{K_0} \right), \tag{3.24}$$

where E_0 is the crack-free Young's modulus, α is the mean aspect ratio of cracks, and K_f is the fluid bulk modulus. The parameter δ is referred to as the saturation parameter and determines the contribution of fluid to the effective bulk modulus (Benson et al., 2006; Fortin et al., 2011; Schubnel et al., 2006).

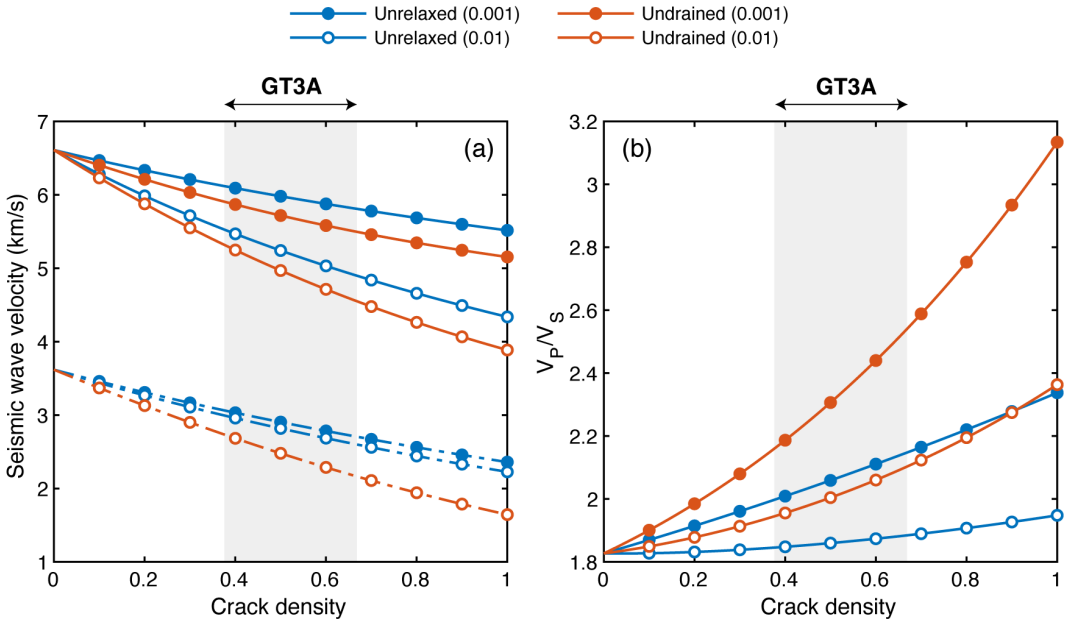

Figure 3.11 (a) P- and S-wave velocities and (b) $V_\mathrm{P}/V_\mathrm{S}$ as a function of crack density. Blue and red lines denote the values under unrelaxed and undrained conditions, respectively. Solid and open circles denote the values calculated with aspect ratios of 0.001 and 0.01, respectively. The range of crack density at the REV scale is shown as gray areas. The calculation was based on the DEM method.

Figure 3.11 shows the P- and S-wave velocities modeled for unrelaxed and undrained conditions as a function of crack density using Equation 3.18 with the DEM scheme. The crack aspect ratios are set to the typical values (10^{-3} and 10^{-2}), and the crack-free parameters were taken to be the mean values of V_P^0 and V_S^0 determined from the mineral abundances of Hole GT3A. The modeled V_P at a given crack density is higher under unrelaxed conditions than undrained conditions for both aspect ratios. This can be attributed to the elevated pore pressure, which serves to elastically stiffen the crack, under relaxed conditions as opposed to undrained conditions. A similar trend is modeled for shear wave velocity (V_S), however, its reduction is more pronounced under undrained conditions than under unrelaxed conditions, as

Gassmann's equations predict that pore water does not affect shear modulus. Consequently, the ratio of P-wave velocity to S-wave velocity (V_P/V_S) under unrelaxed conditions may be relatively lower than that under undrained conditions, despite being higher than when fluid is absent. This implies that the interpretation assuming undrained conditions may lead to an underestimation of the crack density inferred from the observed V_P/V_S in seismic surveys. Given that range of crack density of Hole GT3A inferred from our analysis can be extrapolated to in situ oceanic crust, seismic-scale V_P/V_S observed would range from ~2 to ~2.2 under unrelaxed conditions, whereas that for undrained conditions are predicted to be up to >3.

Note that the MSCL-W data and the computed crack density utilized in this study are based on ambient pressure conditions. As previous laboratory experiments have demonstrated, cracks with small aspect ratios tend to close under in situ pressure conditions in the ocean crust (Christensen, 1984; Hatakeyama et al., 2021; Nagase et al., 2022). In such a case, the permeability would be significantly reduced (Christensen & Ramananantoandro, 1988; Katayama et al., 2012), and the WIFF may be even suppressed, resulting in a more unrelaxed system. Meanwhile, care must be taken that the heterogeneity of the crack distribution itself may be altered with crack closure.

Despite the depth at which the pressure is high enough to close cracks, many seismic surveys have found anomalously high V_P/V_S up to ~3.0 at low-velocity zones in the interior of the subducting oceanic crust (Audet & Bürgmann, 2014). These anomalies possibly indicate the significantly low effective pressure that is enough high to remain the cracks open (i.e., extremely high pore pressure close to the lithostatic pressure). Since the effective pressure largely controls the rock's rheological properties, it has been suggested that such high V_P/V_S and the seismic activity at subduction zones are linked (Saffer & Tobin, 2011). Pimienta et al. (2018) suggested that the observed high V_P/V_S anomalies can be related to highly damaged rock with undrained pore pressure conditions, based on their laboratory measurements of frequency-dependent elastic moduli. However, our analysis implies that the REV in terms of microcracks in the oceanic crust can be unrelaxed conditions even for low-frequency seismic velocity. The unrelaxed V_P/V_S expected for Hole GT3A is ~2.2 at most, which is much lower than the anomalies observed at subduction zones. This discrepancy indicates that a much high crack density may be needed to account for the observed seismic anomalies. Otherwise, the structure of the microcrack network related to brittle fracturing within the subducting crust could be markedly homogeneous extensively.

We evaluated the heterogeneity of the pore structure of Hole GT3A in terms of microcracks that can be captured by ultrasonic measurements. However, natural geological systems likely contain multiple scales of porosity structure and hence multiple scales of heterogeneity in addition to that of microcracks (Bailly et al., 2019; Ringrose et al., 2008). Indeed, the cores collected from Hole GT3A commonly contain millimeter-scale mineral veins, that can be interpreted as fractures that once acted as fluid pathways within the oceanic crust (Kelemen et al., 2020d). Assuming the typical aspect ratio of those fractures to be 10^{-3} (van Everdingen, 1995), the length of such large-scale fractures can be as much as several meters. The scale of heterogeneity of those fracture distributions may be a few orders of magnitude larger than that of microcracks (Bailly et al., 2019). Meanwhile, such fractures can have much larger effective permeability as much as 10^{-11} m^2 (Akamatsu et al., 2023), because permeability strongly depends on the size of the fracture (Guéguen & Palciauskas, 1994). Given such high permeability, pore pressure conditions in terms of the large-scale fractures would be undrained if its scale of REV is less than several tens of meters, whereas that for microcracks is still unrelaxed. This could imply that the presence of large-scale fractures in addition to microcracks may lead to much high V_P/V_S, even if their population is relatively minor compared with that of microcracks.

3.6 Conclusions

Analyses of the depth variation of continuous V_P data measured during the Oman Drilling Project revealed that the scale of heterogeneity of microcrack structure in the oceanic crust is on the order of a few meters. Based on the permeability calculated from the microcrack geometry parameters, the elastic wave velocities observed by borehole logging and seismic surveys possibly reflect elastic moduli under unrelaxed conditions, in contrast to the conventional interpretation. In such cases, the degree of crack damage inferred from V_P/V_S anomalies observed at subduction zones, may be underestimated. Although our calculations are simplified and involve many assumptions and uncertainties, they can be applied to other borehole data, facilitating the evaluation of the heterogeneity of various physical properties in different tectonic settings.

Chapter 4

Paleo-permeability structure of the crustal section of the Samail ophiolite inferred from vein geometry

4.1 Introduction

Water transported into an oceanic plate plays a key role in various geochemical and geophysical processes, such as global transfers of mass and heat (Müller & Dutkiewicz, 2018; Stein & Stein, 1994) and magmatic and seismic activities at subduction zones (Hacker, 2008; Peacock, 2001). The water is supplied mainly through fractures and faults in the oceanic crust that are formed by tectonic and thermal stresses (Faccenda, 2014; Korenaga, 2007). It is, therefore, important to characterize fractures in the interior of the crust if we are to understand fluid behavior in the oceanic lithosphere.

Permeability is a measure of the ease of fluid flow in a rock, and it is an important physical property for constraining the flow rate and mechanism of fluid circulation in oceanic plates (Guéguen & Palciauskas, 1994). To investigate the influence of fractures on the permeability of oceanic crust, measurements of permeability have been conducted in the laboratory using oceanic crustal rocks (e.g., Brett-Adams et al., 2021; Christensen & Ramananantoandro, 1988; Gilbert & Bona, 2016; Katayama et al., 2012). These laboratory experiments yielded values for the permeability of intact basaltic and gabbroic rocks ranging from 10^{-22} m^2 to 10^{-16} m^2 under crustal pressure and temperature conditions. These values are several orders of magnitude lower than those obtained directly from borehole measurements in actual

oceanic crust and indirect estimates based on numerical models (10^{-18}–10^{-9} m^2, Fisher, 1998). The discrepancy between laboratory and *in situ* measured permeabilities is possibly related to differences in the scale of measurements and hence the scale of fractures, and relatively large-scale fractures can control the fluid flow in actual oceanic crust (Guéguen et al., 1996; Schulze-Makuch et al., 1999). However, measurements of *in situ*-scale permeability using boreholes have been limited to the uppermost oceanic crust because of the difficulty of deep seafloor drilling and sampling, and the permeability structure of deeper parts of the oceanic crust is poorly understood.

Knowledge of water–rock interactions in deep oceanic crust can be obtained from ophiolites, which are fragments of ancient oceanic lithosphere that have been tectonically obducted onto continental margins. The Samail ophiolite is the most extensive and best-exposed cross-section of oceanic lithosphere (Nicolas et al., 2000), and it exposes complete sections from sediments and pillow lavas to mantle peridotite. Various geological and geochemical studies conducted on the Samail ophiolite have revealed that the hydrothermal circulation of seawater-derived fluids was important, even down to the lower oceanic crust as well as in the upper crust (Bosch et al., 2004; Coogan et al., 2006; Manning et al., 1996; Zihlmann et al., 2018). To reach a better understanding of the nature of the subsurface hydrothermal processes preserved in the Samail ophiolite, continuous cores through the crustal section to the mantle section of the ophiolite were recently sampled with a recovery rate of ~100% during the Oman Drilling Project of the International Continental Drilling Program (ICDP). The cores collected from crustal sections during the Oman Drilling Project commonly contain macroscopic mineral veins that are filled with minerals such as epidote and calcite (Kelemen et al., 2020b, 2020c, 2020d). These veins can be interpreted as fractures that once acted as fluid pathways. Therefore, by examining the distribution and geometry of these veins, we can estimate the paleo-permeability of these core samples (Gilbert et al., 2018).

For this study, we developed a new method of automatically detecting veins in the the drilled core samples using 3-D X-ray Computed Tomography (XCT) images. XCT imaging enables nondestructive observation of the internal structures of materials, and it has recently been introduced to the field of Earth sciences (e.g., Baker et al., 2012; Godel, 2013; Gupta et al., 2019; Ohtani et al., 2001; Okazaki et al., 2021). Using our newly developed method, we investigated the spatial abundance and geometry of veins in the core samples collected from Oman Drilling Project Holes GT1A, GT2A, and GT3A, which correspond to the upper to lower crustal sequences of the Samail ophiolite. Applying the geometric data for the detected veins to the equivalent channel model (Walsh & Brace, 1984) and permeability

tensor theory (Oda, 1985), we estimated a first-order approximation of the maximum model permeability structure for the deeper parts of the oceanic crust when the veins were acting as fluid conduits.

4.2 Drill Holes and Core Samples

We analyzed core samples of the Samail ophiolite from boreholes GT1A, GT2A, and GT3A of the Oman Drilling Project (Table 4.1). Hole GT1A was drilled vertically through the layered cumulate gabbro section of the lower crustal sequence of the ophiolite (Figure 4.1a,b). At the outcrop near Hole GT1A, a hydrothermal fault cuts across the hole at a depth of ~200m with a dip angle of 54°±9° (Zihlmann et al., 2018). Hole GT2A penetrated the transition zone from upper foliated gabbro to lower layered gabbro that makes up the middle- to upper-parts of the plutonic sequence of the ophiolite (Figure 4.1a,c). Hole GT3A was drilled through the sheeted dike section to the gabbro section, which corresponds to the transition from the upper crust to the lower crust (Figure 4.1a,d). Hole GT3A was drilled perpendicular to the ground, and the transition zone of the sheeted dike and underlying gabbro dips gently (~30°) toward the southeast. The cores from these boreholes have undergone hydrothermal alteration, and hydrothermal veins are found throughout the core sections (Kelemen et al., 2020a).

Table 4.1 Drill-hole information

Hole	Lithology	Total depth (m)	Number of core sections[a]
GT1A	Layered cumulate gabbro	400	548 (500)
GT2A	Foliated to layered gabbro transition	406	541 (521)
GT3A	Sheeted dike to gabbro transition	403	545 (502)

[a] Numbers in parentheses are those used for our analyses.

All core samples collected during the Oman Drilling Project were scanned using a medical XCT scanner (Discovery CT 750HD, GE Medical Systems) before various descriptions and measurements were taken onboard. This technique allowed for non-destructive examination of the internal structure of the cores. All XCT data were obtained using an excitation voltage of 140 kV and a current of 100 mA in the X-ray tube (X-ray source), and with resolutions of 0.176 mm/pixel for the directions perpendicular to the core axis (X and Y directions) and

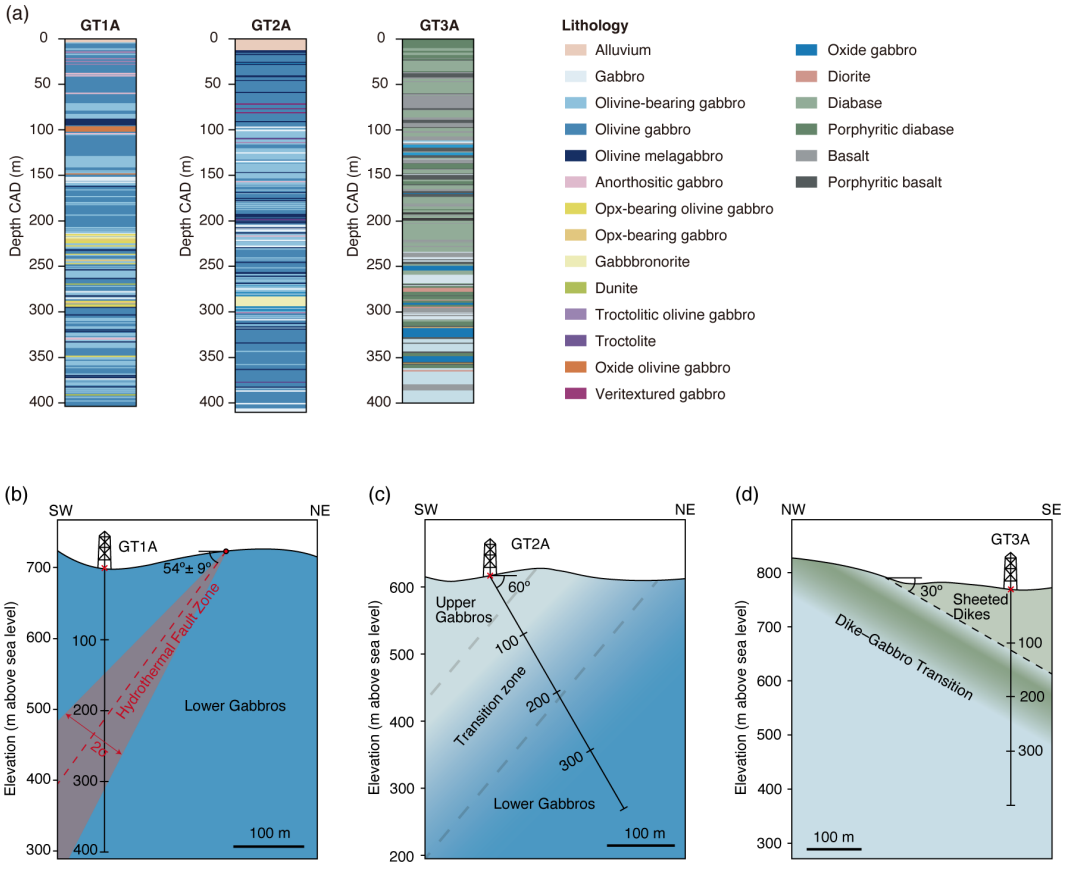

Figure 4.1 (a) Stratigraphy of crustal sections of the Samail ophilite from boreholes of the Oman Drilling Project. Hole GT1A penetrated the layered cumulate gabbro section of the lower crust; Holes GT2A penetrated foliated gabbro to layered gabbro, representing the middle of the crust; and Hole GT3A penetrated the sheeted dike–gabbro transition zone, which corresponds to the upper–lower crust transition. (b–d) Cross-sections along the trends of Holes GT1A, GT2A, and GT3A. Hole GT1A was drilled to intersect the Zihlmann–Müller Fault Zone (Zihlmann et al., 2018).

0.625 mm/pixel for the direction parallel to the core axis (Z direction). Details of the XCT scanning method are summarized in the initial report of the Oman Drilling Project (Kelemen et al., 2020a). Figure 4.2a shows an example of a volume-rendered 3-D XCT core image (GT3A 36Z-2), and Figure 4.2b, c shows the X–Z and Y–Z slice images. Colors indicates the Computed Tomography (CT) number of each voxel and pixel, which is defined as follows:

$$\text{CT number} = \frac{\mu_t - \mu_w}{\mu_w} \times 1000, \tag{4.1}$$

where μ_t is the linear attenuation coefficient (LAC) of the target material and μ_w is the LAC of water. When an X-ray of incident intensity I_0 passes through a homogeneous material of thickness L, the transmitted intensity I decays as follows:

$$I = I_0 \times e^{-\mu L}. \tag{4.2}$$

A reference material was used for quality control (QC) and comprised three layers of air, water, and aluminum that made up a telescope-shaped cylinder with six steps (1–6 cm in diameter). The QC material was scanned after air calibration to check that the CT numbers were within QC ranges of -1008 < CT number < -1002 for the air layer, -2 < CT number < 7 for the water layer, and 2416 < CT number < 2499 for the aluminum layer. The LAC is a function of the chemical composition and density of the target material (Godel, 2013), which meas that XCT imaging provides information not only about density but also about the chemical composition of the cores. According to the shipboard descriptions, the cores of the GT sites are composed mainly of plagioclase and pyroxene, but the veins are filled with secondary minerals such as chlorite and epidote (Kelemen et al., 2020d). The veins are recognized in the XCT images as parts with CT numbers that differ from those of surrounding material (Figure 4.2).

4.3 Automated vein detection in 3-D X-ray CT images

4.3.1 Procedure of vein detection from XCT core images

The minerals that fill the veins have chemical compositions that differ from those of the matrix, so we can expect these differences to be observed in the differences in CT number (gradient) in the XCT images. Therefore, we used the gradient in CT numbers to detect the veins from the XCT core images. Planar features such as veins and fractures in the cylindrical core specimens appear as sine curves in an “unwrapped” image of the core (Figure 4.3a).

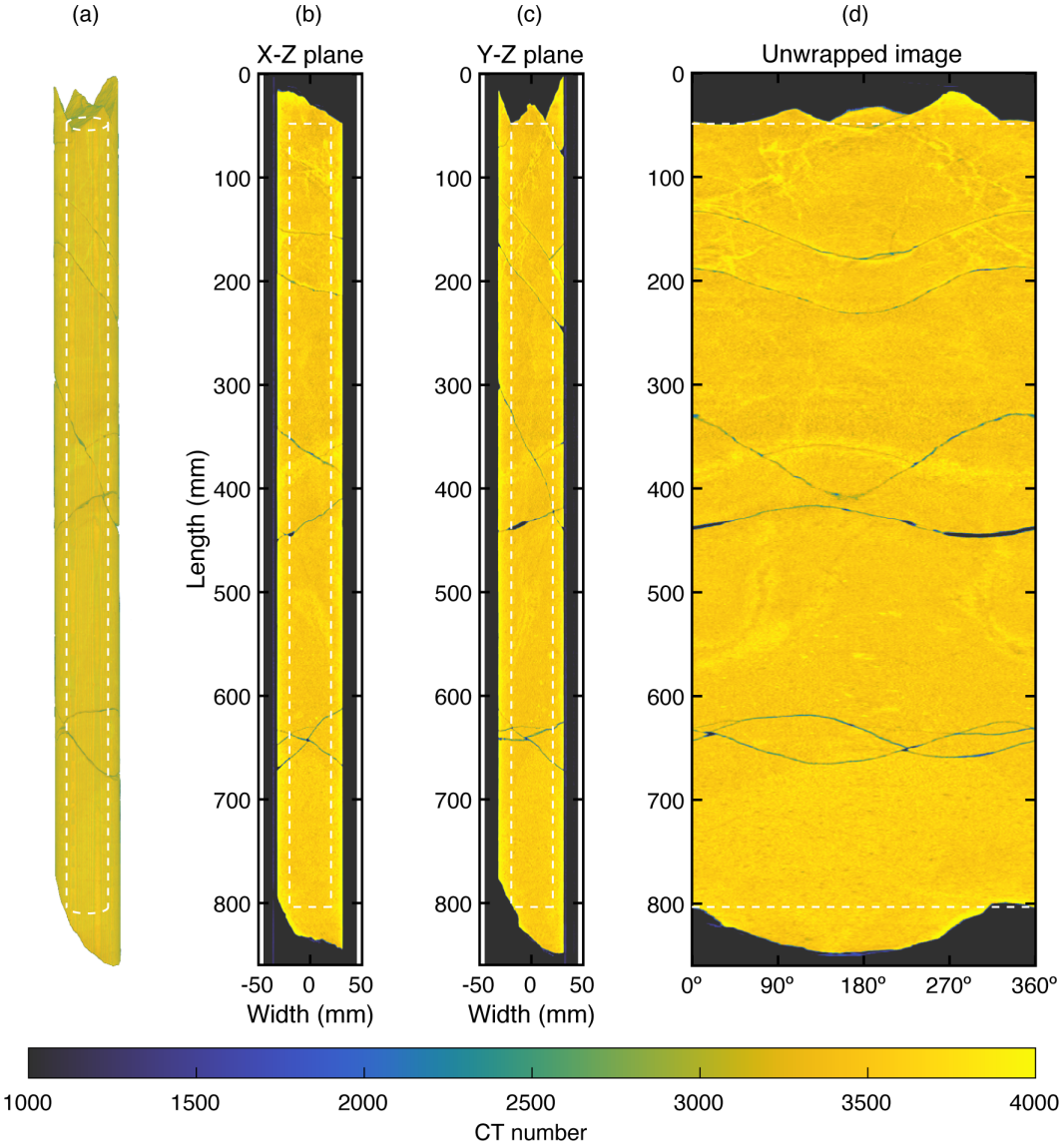

Figure 4.2 Example of X-ray Computed Tomography (XCT) images of core section 36Z-2 from Hole GT3A. (a) 3-D XCT image. (b, c) 2-D X-ray CT images along the X–Z and Y–Z planes. (d) Unwrapped image generated from the center of the core cropped in a circle with a radius of 100 pixels (diameter of 35.2 mm, white dashed lines). The region of interest (ROI) is selected so that the core is cylinder-shaped.

The geometry and attitude of such features can be determined by identifying the parameters of the sine curve. Such a method is commonly applied to detect fractures in the image of a borehole wall (e.g., Al-Sit et al., 2015; Assous et al., 2014; Taibi et al., 2019). Based on these standard approaches, we developed a new method of detecting planar geological features, including veins and fractures, in the XCT core images. To reduce problems of human interpretation and computational time, we fully automated the proposed method by using an iterative adaption of the two-step Hough transform combined with multiscale Hessian filtering for identifying an elongate structure. A block diagram illustrating the proposed method is shown in Figure 4.3b, and each step is described in detail in the following sections.

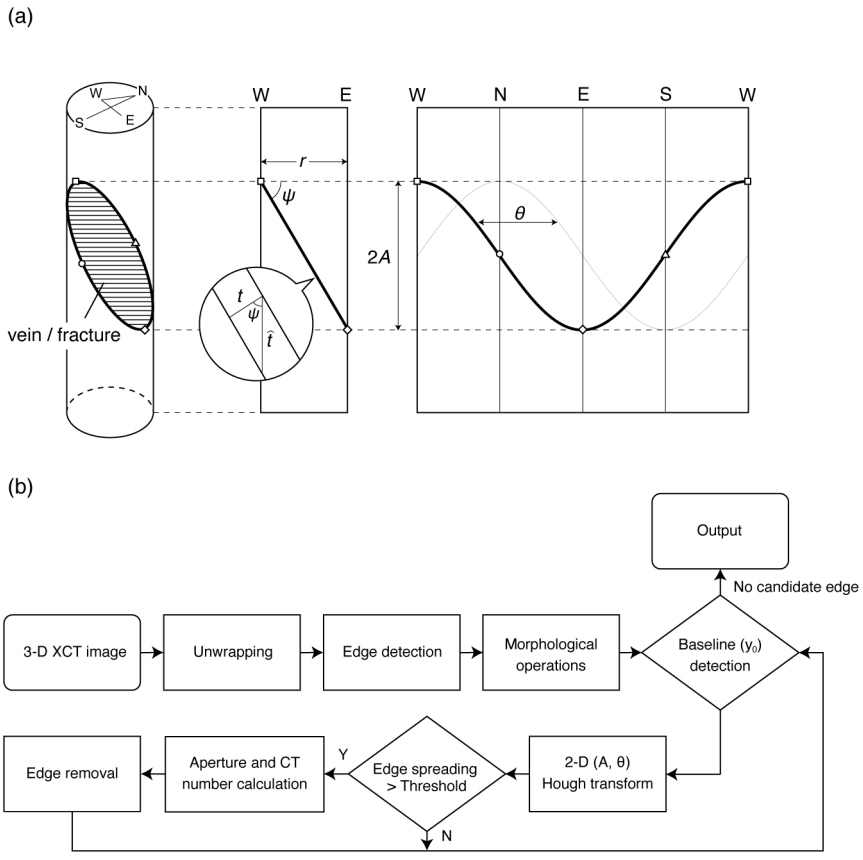

Figure 4.3 (a) Illustration showing a vertical cylindrical core with a dipping planar feature such as a vein or fracture and its appearance in the unwrapped image. (b) The flow chart of the automated vein detection process.

4.3.1.1 Edge extraction

First, an unwrapped image is prepared from a 3-D core CT image (Figure 4.2d). To remove the CT hardening effect, which is an effect where the CT number appears artificially high at the boundary between two materials with extremely different CT numbers (such as the boundary between air and minerals), the unwrapped image was generated from the cylindrical-shaped region cropped with a radius of 100 pixels, which is equivalent to a diameter of 35.2 mm (Figure 4.2). Next, multiscale Hessian matrix filtering was applied to the unwrapped image to extract vein-like regions. The Hessian matrix is a square matrix containing second-order partial derivatives of the input image data, and it can roughly distinguish lines, grains, and planes using eigenvalues (Jerman et al., 2015, 2016). Multiscale Hessian filtering has been used to detect fractures in rocks from micro-CT (μCT) images (e.g., Voorn et al., 2013). The filter was implemented in MATLAB-code by Jerman (2017) and by applying it to a CT image, the likelihood of each pixel being a vein (likeness of vein) is expressed as a value between 0 and 1 (Figure 4.4b). Then, a binary image is created by extracting pixels with a high likeness of vein (Figure 4.4c) based on a percentile method in which the pixels are extracted in order from that with the highest (or lowest) value until the total number of extracted pixels reaches the specified percentage. Because the volume fraction of the vein to the whole core can be up to 6% (Kelemen et al., 2020a), we defined the threshold as 6% of the total image area. Finally, we applied some post-processing steps to the binarized image to remove noise and uncertain edges (Figure 4.4d). We applied some morphological operators to remove noises, skeletonize the binary image (i.e., thinning), and prune small spurs that appear on the skeleton by using the *bwpropfilt*, *bwskel*, and *bwmorph* functions of the MATLAB Image Processing Toolbox.

4.3.2 Vein detection using the iterative two-step Hough transform

The exact shape of edge segments that correspond to veins/fractures is found using a pattern recognition technique that fully characterizes the sine curves. The Hough transform is a well-established method for detecting complex patterns of points in binary image data, allowing us to determine the parameters that characterize the patterns even in the presence of noise, extraneous data, and occlusions (Al-Sit et al., 2015). A successful application of the Hough transform requires clear knowledge of the type of curve being sought, so that an analytical relationship between the image and the parameters of the transform space can be obtained. The shape of a planar rock discontinuity appears as a sinusoid expressed as

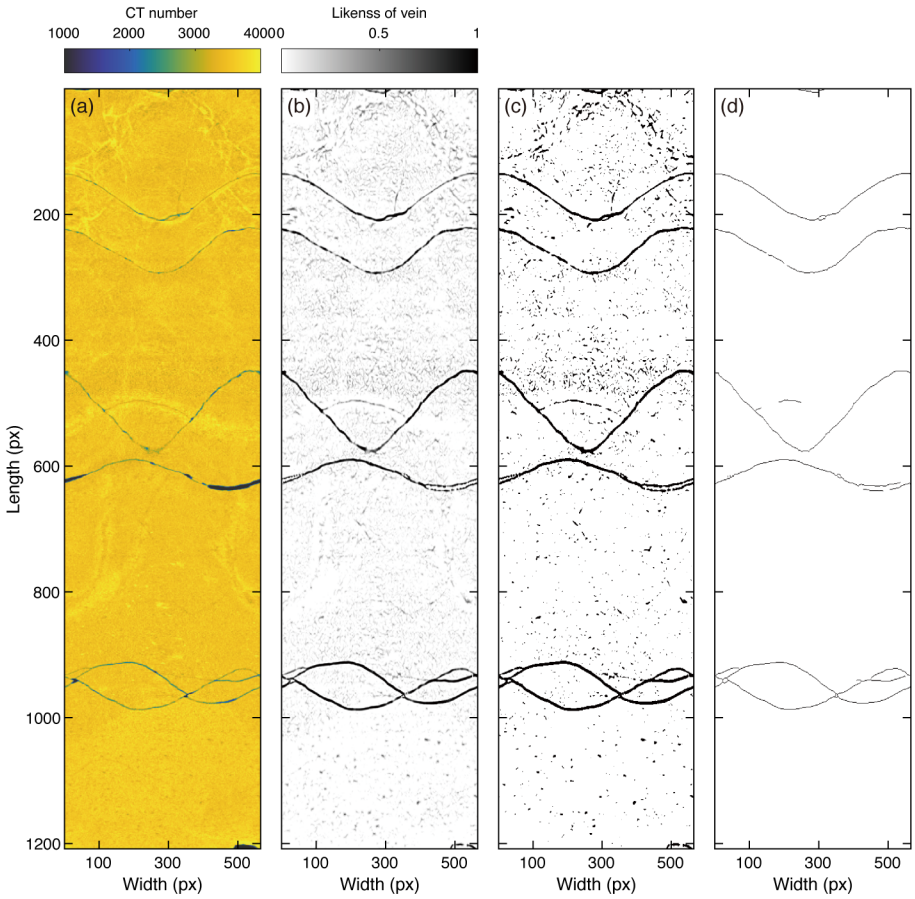

Figure 4.4 Example of edge extraction process of core section 36Z-2 from hole GT3A. (a) Original unwrapped CT image. (b) Results of the multi-scale Hessian filtering (Jerman et al., 2015). (c) Binarized image. (d) Edges filtered by several morphological operations which remove noises and extra pixels.

follows:

$$y = A\sin(\omega x + \theta) + y_0, \tag{4.3}$$

where A is the amplitude, y_0 is the baseline position, ω is the angular frequency, and θ is the phase (Figure 4.3a). Note that $\omega = 2\pi/T$, and T is the image width (565 px). As ω is constant in the core image, the sinusoidal features can be fully captured by specifying A, θ, and y_0. In this case, the Hough transform can be interpreted as a one-to-many mapping from binary image points (x, y) to the parameter space (A, θ, y_0), which is equivalent to computing the parameters of all sine curves belonging to the set passing through any given image point (Al-Sit et al., 2015). To increase the computational efficiency and make interpretation of the results easier, we developed a method of performing automated vein detection from XCT images using an iterative two-step Hough transform based on the method proposed by Changchun & Ge (2002). In this method, y_0 is first determined by a search strategy that utilizes the symmetry of a sine curve, and then the Hough transform is performed in two dimensions (A, θ). The novelty of our method is to perform these processes iteratively for each vein candidate one by one, which allows us to detect the veins efficiently while avoiding false positives. The specific steps are as follows:

1. Start with the binary image generated at the edge detection stage (see section 3.2) or step 12 described below. If the number of edge candidates is less than a threshold that should be chosen in advance, the calculation is finished.
2. Prepare a 1-D accumulator array for y_0, the length of which is the same as that of the binary image, and initialize all elements to zero.
3. For an edge point p_1 with coordinates (x_{p_1}, y_{p_1}) in the binary image, find edge points p_2 (x_{p_2}, y_{p_2}) that are $T/2$ away from p_1 on the x-axis (Figure 4.5a).
4. Point C is selected as the average between points p_1 and p_2, where the vertical coordinate y_C is calculated from $y_C = (y_{p_1} + y_{p_2})/2$. According to the symmetry of a sine curve, the point C happens to fall on the baseline of the sine curve that passes through points p_1 and p_2, and values of y_C are the same for all pairs of points on a curve. Therefore, the vertical component of C can be used to represent the baseline y_0.
5. Increment the accumulator element corresponding to the determined y_C by one.
6. Loop steps 3–5 until all edge points are computed. The offsets where sine curves are likely to be present appear as peaks in the accumulator (Figure 4.5b).
7. Pick one peak with the highest value, which should be higher than a predetermined threshold, and set the y_C of the peak as a candidate offset y_0, which is used in the

next set of calculations (Figure 4.5c). The remaining peaks will be picked in the next loops. If there are no peaks beyond the threshold, finish the calculation and output the detection result.

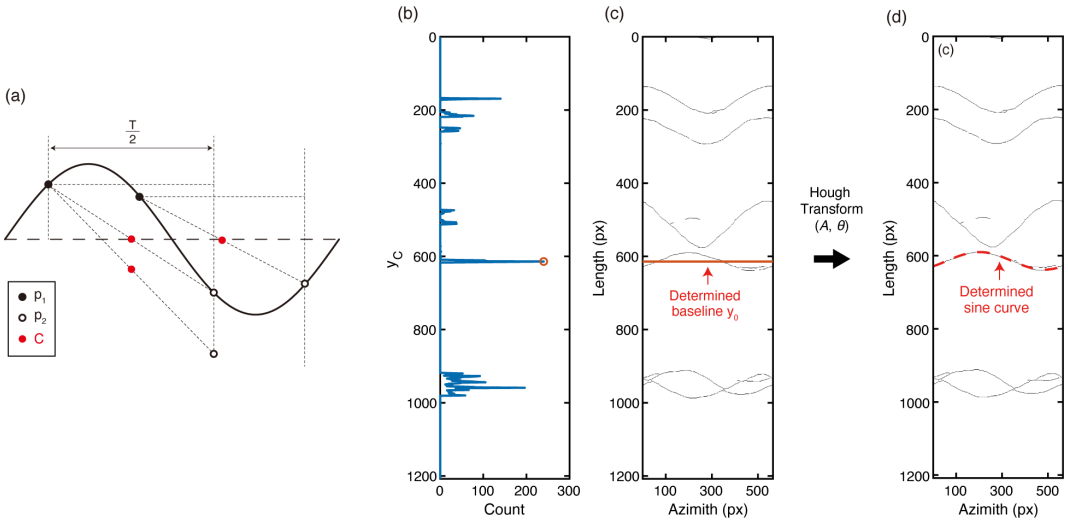

Figure 4.5 Example of detecting a sine curve in the binarized image. (a) Sine curve with selected points p_1 and p_2. (b) 1-D accumulator space for locating the baselines. The red circle represents the highest peak, which is used for the following steps. (c) Original binary image with baseline (y_0) determined by peak selection from the accumulator. (d) Sine curve determined using the 2-D Hough transform and y_0 from in the previous step.

Then, by using the determined candidate offset y_0, the two-dimensional Hough transform into (A, θ) space is performed as follows:

8. Map each edge point in the binary image into (A, θ) parameter space (Figure 4.6a) by

$$A = \frac{y - y_0}{\sin(\omega x + \theta)}, \tag{4.4}$$

where x, y are the coordinates of the edge point, $0 \leq A < A_{\max}$, and $0 \leq \theta < 2\pi$. $A_{\max}$ should be chosen in advance.

9. Divide the parameter space into discrete accumulator cells and then increment the value of the cell through which the (A, θ) curve passes by one (i.e., voting). This process is performed for all edges. As a result, each cell in the parameter space has the value of the number of times that the curves have passed through it (Figure 4.6b). The coordinates of the cell with the highest value in the parameter space (A^*, θ^*) correspond to the amplitude and phase of the sine wave in the original image (Figure 4.5d).
10. Although most targets can be detected by simply selecting the maximum highest value

of the accumulator surface, this can sometimes lead to false results in more complex and noisy images. To eliminate false peak detection, calculate the *Edge spreading* for each detected sine curve, which represents the total number of pixels along a sinusoid and is a measure of how long the edge candidates spread in the core circumference. Here, we define false positives as those where the *Edge spreading* was less than about two-thirds of the width of the image.

11. If the detected edges are positive, calculate the average aperture and CT number of the vein/fracture using the method described in the following section.
12. Remove these edges from the original binary image so that they will not be used in the next round of calculations. This allows efficient picking of positive peaks one by one while avoiding false positives that appear in noisy images.
13. Return to step 1.

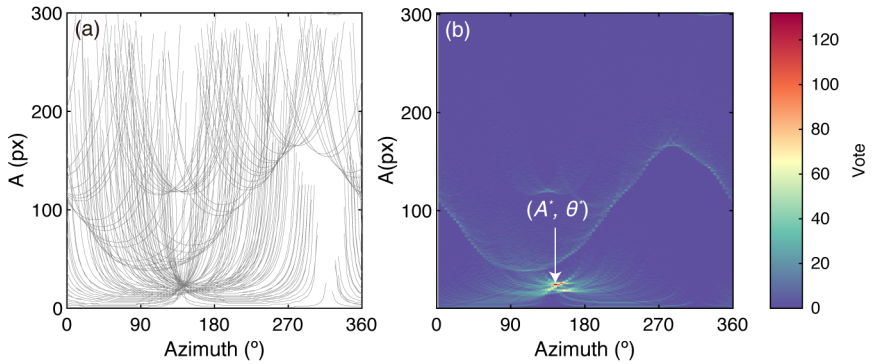

Figure 4.6 Example of the two-dimensional Hough transform. (a) Result of mapping from the binary image to (A, θ) space using Equation 4.4. (b) Result of inclementing the value of the cell through which the (A, θ) curve passes by one (i.e., voting). The coordinates of the cell with the highest value in the parameter space (A^*, θ^*) correspond to the amplitude and phase of the sine wave in the original image.

4.3.3 Determination of vein geometry and CT number

For veins with detected edges are positive (step 11 of the previous section), the aperture and CT number of the vein/fracture are determined using the binary and CT images. First, the region of interest (ROI) is set as a region with a width of 20 pixels along the determined sine curve. Then the distribution of the CT numbers of the pixels that were extracted as the edges in the ROI are examined. We define the average CT number of these edges as the CT number of the vein/fracture ($\mu_{\mathrm{vein/fracture}}$). The fraction of pixels with CT numbers less than 1000 is also calculated; if the fraction is less than 1% it is considered to be a vein, whereas if it is greater than 1% it is considered to be a fracture. Note that the value of 1000

as a threshold value is based on the fact that a pixel (i.e., mixel) with half air (CT number of -1000) and half mineral (CT number of 3000) regions will have a CT number of 1000. The veins with a CT number greater than the matrix values are defined as High-CT (HCT) veins, whereas those with lower CT numbers are defined as Low-CT (LCT) veins. The average aperture of the vein/fracture is then calculated by dividing the number of pixels in the ROI whose CT number is within $\mu_{\text{vein/fracture}} \pm 1\sigma$ by the arc length of the sine curve. Because this value is the apparent aperture in the vertical direction (Z-axis direction) of the tilted vein/fracture (Figure 4.3), we calculate the true value of aperture t as follows:

$$t = \hat{t} \cos \psi, \tag{4.5}$$

where $\hat{t}$ and ψ are the apparent aperture and dip angle of the vein/fracture, respectively. The apparent dip angle of the vein/fracture across the cylindrical core is calculated by

$$\psi = \arctan\left(\frac{2A}{r}\right), \tag{4.6}$$

where A is the scaled amplitude of the vein/fracture, and r is the diameter of the cropped core (35.2 mm).

4.4 Application to the core samples from GT site of the Oman Drilling Project

4.4.1 Results of vein detection

The newly developed method was applied to the X-ray CT images of core sections of the Samail ophiolite sampled during the Oman Drilling Project (Holes GT1A, GT2A, and GT3A). Although ~550 core sections were sampled for each hole and their CT images taken for shipboard descriptions, some of these cores are highly fractured, and only fragments are left. Therefore, we used only those parts of the cores that retain a cylindrical shape. The number of the analyzed cores is >500 for each borehole (Table 4.1). The parameters determined for all analyzed cores are summarized in the Supplementary Material (Data Set S1).

Figure 4.7 shows representative results of the vein detection for each hole. The red, blue, and white dashed lines represent the detected LCT veins, HCT veins, and fractures, respectively. The veins and fractures that appear continuously and clearly in the unwrapped images were successfully detected, even if they intersect. In contrast, tubular features that are

partially interrupted, blurred, or not appearing as a clear sine curve were not detected as veins/fractures.

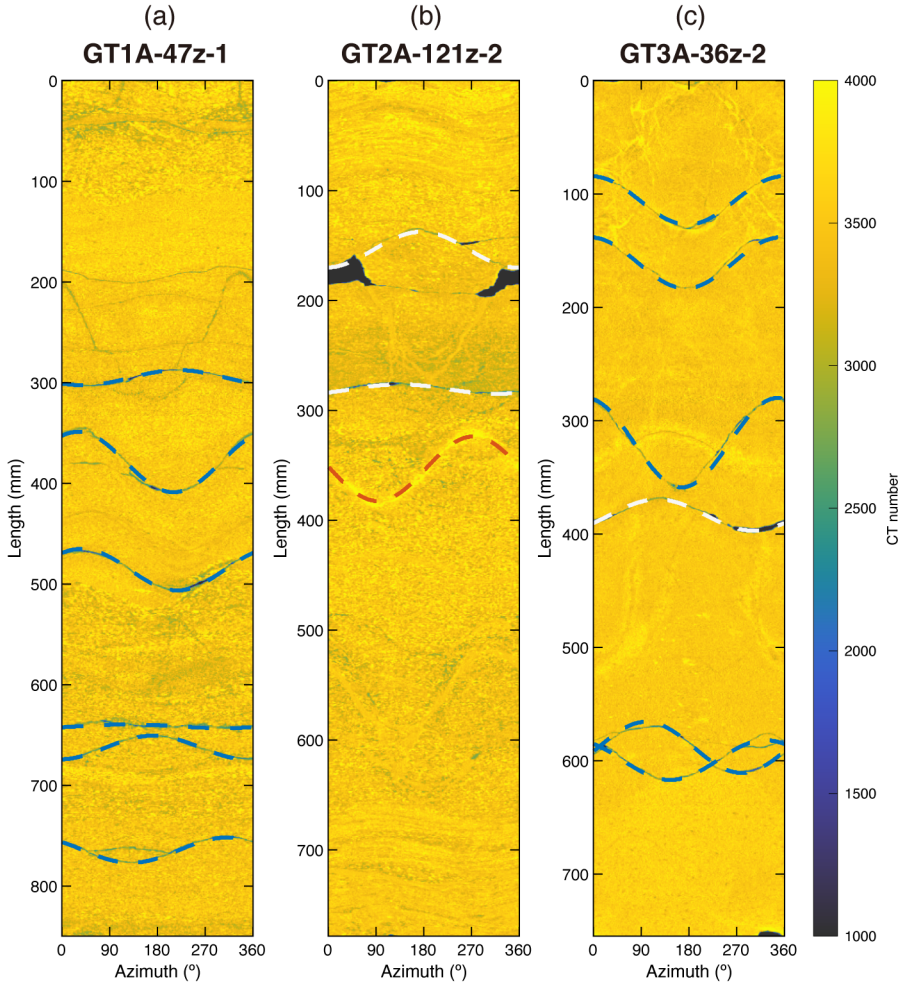

Figure 4.7 Examples of the results of the automated vein detection method applied to core sections collected from Holes GT1A, GT2A, and GT3A of the Oman Drilling Project. Red, blue, and white dashed lines represent LCT veins, HCT veins, and fractures, respectively.

Table 4.2 Summary of vein detection.

Hole	Number of vein		Vein density (m^{-1})		Median aperture (mm)	
	HCT	LCT	HCT	LCT	HCT	LCT
GT1A	63	449	0.16	1.11	1.03	0.73
GT2A	81	361	0.20	0.89	1.50	0.74
GT3A	45	571	0.11	1.43	1.39	0.71

In each hole, 45–81 HCT veins were detected, and the vein densities for the entire hole range from 0.11 to 0.20 (Table 4.2). In addition, 361–571 LCT veins were detected in each hole, with vein densities ranging from 0.89 to 1.43, and these densities are much higher than those of the HCT veins. The histograms of the CT numbers of the veins/fractures for each hole are shown in Figure 4.8. The CT numbers of the HCT veins are range from 3400 to 4800 with a peak at ~4000 for each hole, whereas the CT numbers of the LCT veins range between 1500 and 3300. Both the HCT and LCT veins appear to be a superposition of a few Gaussian distributions. The distribution of the vein CT numbers reflects differences in the secondary minerals that fill the veins, in which the peaks can represent their principal minerals and the variance of the distribution can represent the variations in mineral combinations. The wide and multimodal CT number distribution of the detected veins can be related to various mineral parageneses. Note that veins with a mean CT number of ~3400, which is a number similar to those of the matrix minerals, were not detected because it would difficult to distinguish them on CT images. Fractures also show some peaks, and the ranges of their CT numbers are much wider, with a minimum of 0 and a maximum of 3000, which partly overlaps those of the LCT veins. Because it is difficult to distinguish between fractures formed during drilling and those that had formed previously in theoceanic crust, and because the apertures do not always retain their original state, the results for the fractures will not be described or discussed in the following sections.

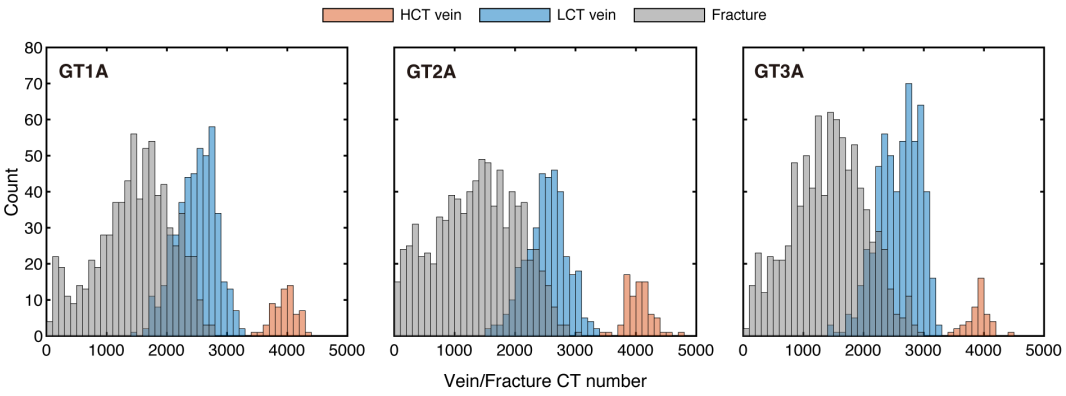

Figure 4.8 Histograms of the CT numbers of veins and fractures for Holes GT1A, GT2A, and GT3A of the Oman Drilling Project.

The spatial occurrence and pervasiveness of the HCT and LCT veins differ (Figure 4.9). The HCT veins are distributed sporadically in the boreholes, and the positions of major fault zones (Kelemen et al., 2020b, 2020c, 2020d) coincides partly with the HCT veins. This suggests that the fluid flow of the HCT vein system can be related to specific zones of faulting

in the oceanic crust. Meanwhile, the LCT veins are pervasive in the boreholes,implying that the LCT vein system was associated with widespread fracturing events that occurred throughout the oceanic crust.

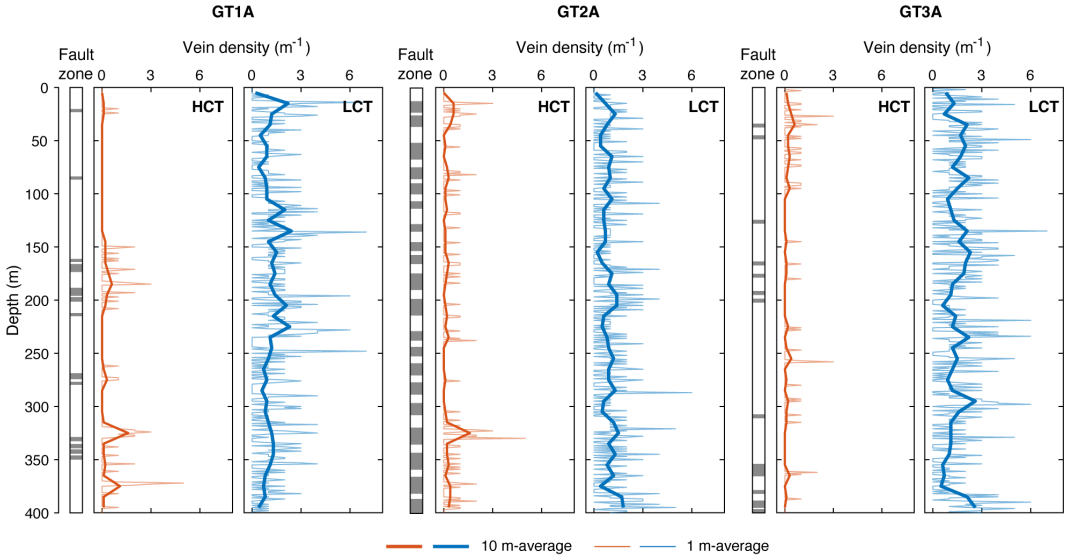

Figure 4.9 Depth variations of vein densities calculated for every 1 m (thin lines) and 10 m (thick lines). The major fault zones in each of these boreholes of the Oman Drilling Project (Kelemen et al., 2020b, 2020c, 2020d) are also shown.

4.4.1.1 Geometry of the veins

Figure 4.10 shows the histograms for the vein apertures of each vein type and borehole. Both types of veins have a distribution skewed toward thinner veins and they both show a single peak. The median values of the HCT and the LCT vein apertures are 1.0–1.5 mm and ~0.7 mm, respectively (Table 4.2). A similar distribution was reported for dikes in the drilled cores recovered from the sheeted dike complex of the Pacific plate (Tominaga et al., 2009), although its size is three orders of magnitude larger than the size of the HCT and LCT veins.

Because the cores from the Oman Drilling Project are partially contiguous on a scale of as much as several tens of meters between breaks in the core, the core orientations are not always consistent for different depth domains (Kelemen et al., 2020d). Therefore, to compare the three-dimensional orientations of the HCT and LCT veins, we captured the clustering of strike and dip angles for each vein type in the vertically contiguous intervals by performing lower hemisphere projections of poles of the veins (Figure 4.11). The stereographic projections were performed at depths of 307–353 m for Hole GT1A, 152–240 m for Hole GT2A, and 23–57 m for Hole GT3A. Because these contiguous sections are not rotated to true north, there

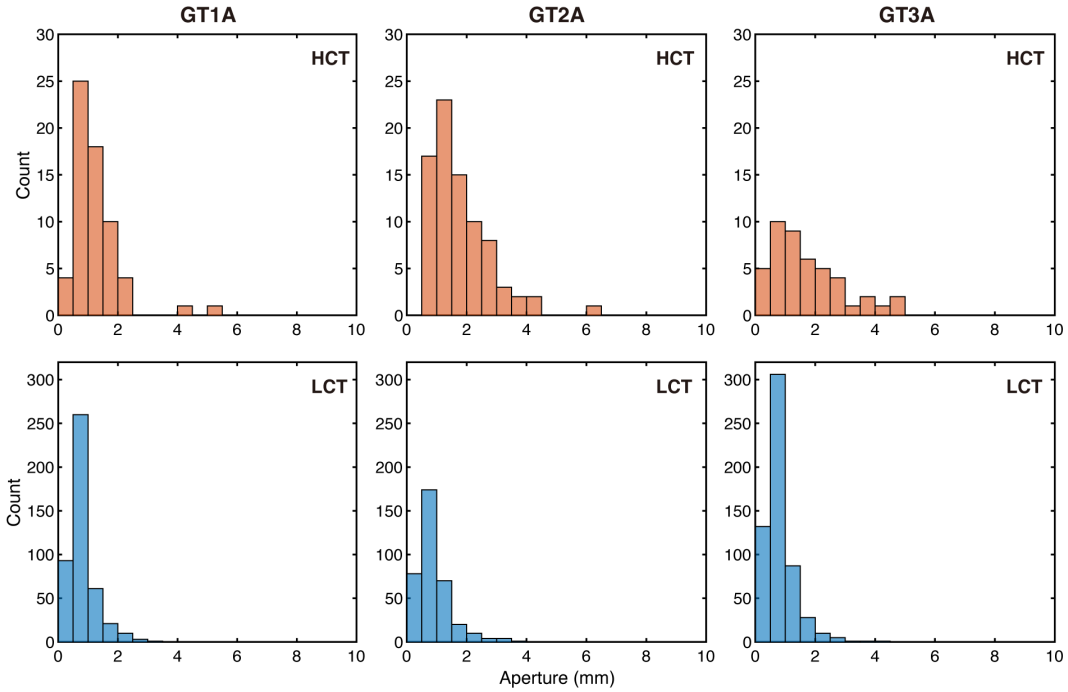

Figure 4.10 Histograms for the widths of HCT and LCT veins in Holes GT1A, GT2A, and GT3A of the Oman Drilling Project.

is no geographic significance. In Hole GT1A, the HCT and LCT veins cluster in directions orthogonal to each other, with the HCT veins at relatively steeper dip angles (~60^o) than the LCT veins. A similar situation is observed for the results of Hole GT3A. Moreover, the HCT veins in Hole GT3A tend to be aligned in the same orientation as the dikes recognized in the same depth domain, and they are therefore possibly related to magmatic/tectonic activities near the mid-ocean ridge (Kelemen et al., 2020d). Hoever, the orientation of the LCT veins differ from those of the dikes. Meanwhile, in Hole GT2A, the clusters of the HCT and LCT veins are similar in their orientations.

Note that, because the probability that a particular vein (or fracture) is intersected by a borehole depends on its orientation, sampling of planar discontinuities intersecting the core creates a bias in the apparent abundance of the orientations (Martel, 1999; Massiot et al., 2012; Terzaghi, 1965). For example, veins that are subparallel to the borehole axis are less likely to intersect the borehole, leading to a systematic underestimation of the sample size of such veins. Applying a statistical weighting factor that depends on the orientation of the vein to correct the sampling bias predicts that more than twice as many veins with dip angles of >60^o may exist than detected before nay such correction (Priest, 1993; Terzaghi, 1965). Therefore, care must be taken to allow for the possibility that the number of veins

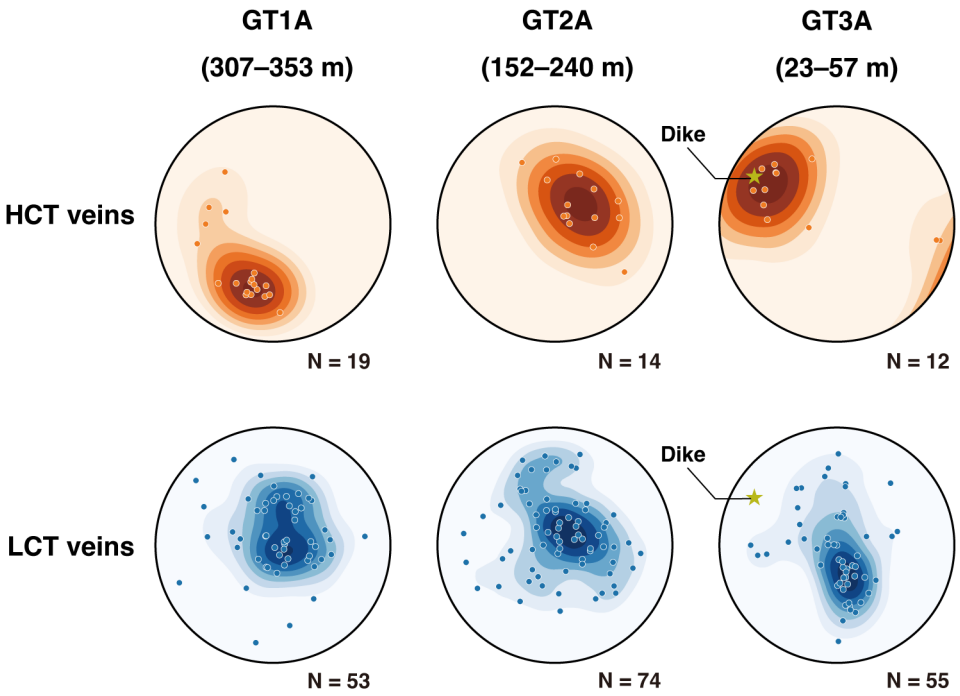

Figure 4.11 Contoured stereoplots for the HCT and LCT veins identified in the representative contiguous intervals in Holes GT1A, GT2A, and GT3A of the Oman Drilling Project. The points plotted are poles to the veins, and N is the number of veins. Because these contiguous sections are not rotated to the true north, there is no geographic significance. For GT3A, the orientation of dike intrusions identified in the same depth domain is plotted for comparetive purposes.

with high dip angle shave been underestimated.

4.4.2 Comparisons with previous studies

To understand the mechanisms of hydrothermal circulation in oceanic crust, several reseachers have described the characteristics of hydrothermal veins in ophiolites, including their distribution, shape, orientation, and mineral content (Nehlig & Juteau, 1988; Nicolas et al., 2000; van Everdingen, 1995). Also, core samples from the Oman Drilling Project were split into two halves after the XCT scanning, and the preliminary data, including the number of veins, vein-filling minerals, and two-dimensional orientations were obtained onboard D/V *Chikyu* (Kelemen et al., 2020b, 2020c, 2020d). In this section, we first compare the geometric information for the detected veins in the core samples of the Oman Drilling Project with data from the literature, and we then discuss the origin of each vein system.

4.4.2.1 Vein density and aperture

Nehlig & Juteau (1988) described the hydrothermal veins in the crustal section of the Samail ophiolite, and they reported that the veins filled with epidote, zoisite, and amphibole in the sheeted dike sections have apertures of 2 mm and the vein densities (i.e., the inverse of spacing) of 0.5–10 m^{-1}, while in the undelying gabbro sections the aperture are 1–5 mm and the vein densities are <0.5 m^{-1}. A similar range of vein apertures and densities was determined for the sheeted dike complex of the Troodos ophiolite, Cyprus (van Everdingen, 1995). These values of vein density and aperture are similar to those we estimated from the XCT images of the drilled cores (Table 4.2). Meanwhile, the shipboard descriptions of the cores of the Oman Drilling Project identified more than 10,000 veins for Holes GT1A, GT2A, and GT3A (Kelemen et al., 2020b, 2020c, 2020d), and the average vein densities are much larger than those of the veins detected in our study (Figure 4.12). This discrepancy may be due to the size of the veins and the resolution of the XCT images. The resolution of the XCT images we used was 0.625 mm/pixel for the direction parallel to the core axis (Z direction), and veins with a width smaller than this value cannot be recognized as pixels where the CT number is different from the surrounding material. This problem possibly led to our underestimating the abundance of veins. Indeed, the shipboard descriptions for Hole GT3A reported that ~80% of the logged veins have a width of <0.6 mm (Kelemen et al., 2020d), which is not visible in our XCT images. Moreover, our method cannot detect the veins that are too short to appear as a sine curve on the unwrapped image of a cylinder with a radius of 100 pixels (corresponding to ~35 mm) from the center of the core, thereby leading

to an underestimation of the number of the veins. However, the contribution of such short, narrow veins to the bulk permeability of the cores is small relative to that of larger veins, because the fracture permeability depends mainly on the scale of the fluid conduit (Gilbert et al., 2018).

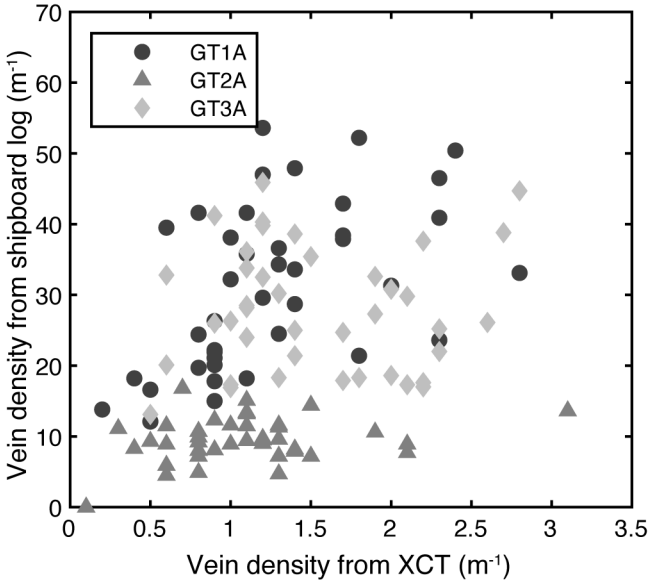

Figure 4.12 Comparison of the 10 m average vein density obtained from our XCT core data with that reported in shipboard descriptions of the cores of the Oman Drilling Project (Kelemen et al., 2020b, 2020c, 2020d).

4.4.2.2 Vein-filling minerals

The shipboard descriptions of the drilled cores from GT site of the Oman Drilling Project reported that the vein fracture fillings include a wide variety of secondary minerals such as epidote, chlorite, quartz, prehnite, and calcite, and that these minerals commonly appear in association with each other (Kelemen et al., 2020b, 2020c, 2020d). For example, the veins found in Hole GT3A are broadly classified into four parageneses of vein type based on the crosscutting relations of amphibole, quartz–epidote–chlorite, zeolite–prehnite, and calcite veins (Kelemen et al., 2020d). Because the CT number reflects the relative density of the material, the HCT veins probably contain relatively dense minerals such as amphibole, epidote, and quartz whereas the LCT veins probably contain less dense minerals such as prehnite and calcite. This was confirmed by comparing the veins we detected with the representative vein types reported in the shipboard descriptions (Kelemen et al., 2020d), so that the epdote- and prehnite-rich veins are characterized by CT numbers of ~4200 and ~2500, respectively. Indeed, prehnite-rich veins have been identified throughout the crust down to

the crust–mantle boundary in the Samail ophiolite, whereas veins with other minerals are distributed sporadically in the crust (Nehlig & Juteau, 1988). This is consistent with the fact that LCT veins are pervasive in each hole but HCT veins are relatively sparse (Figure 4.9).

4.4.2.3 Vein orientations

Systematic observations and measurements of the orientations of hydrothermal veins in the crustal sequences of the Samail ophiolite have shown that veins that were formed during on-axis fluid circulations are oriented preferentially along strike in vertical planes (Nehlig & Juteau, 1988; Nicolas et al., 2000). In other words, they are parallel to the dikes and perpendicular to the paleo-Moho. The shipboard descriptions for cores of Hole GT3A also noted that epidote-rich veins tend to show orientations similar to those of the dikes (Kelemen et al., 2020d). This is consistent with our findings for the HCT veins, which are probably filled with high-density minerals such as epidote and tend to be aligned parallel to the dikes in Hole GT3A (Figure 4.11). In Hole GT2A, hydrothermal veins filled with secondary minerals such as epidote, chlorite, quartz, laumontite, and prehnite tend to be oriented at a dip angle of ~45°, with their abundance tapering off for lower and higher dips (Kelemen et al., 2020c). This is consistent with the clusters of moderately dipping angles we detected for HCT and LCT veins in Hole GT2A (Figure 4.11). Although detailes of the angular distribution of veins were been reported in the shipboard descriptions for Hole GT1A, we found that the HCT veins in Hole GT1A are oriented preferentially at an angle of 60° (Figure 4.11), and this is similar to the orientation of the hydrothermal fault that cuts across the borehole (dip angle of 54° ± 9°, Figure 4.1) and contains a chlorite–epidote-rich gouge (Kelemen et al., 2020b; Zihlmann et al., 2018).

4.4.2.4 Origin of the veins

According to petrological observations and analysis of the veins in the Samail ophiolite, the veins that contain minerals such as epidote and quartz belong to the earliest vein system that was formed during the circulation of high-temperature hydrothermal fluid near the ridge. The veins that contain prehnite and calcite belong to later vein systems that were formed by lower temperature off-axis circulating hydrothermal fluids (Nehlig, 1994; Nehlig & Juteau, 1988). Based on these lines of evidence, the HCT vein system probably belongs to a high-temperature early vein system that formed near the ridge, whereas the LCt veins probably belong to a later lower-tempareture system of veins that formed away from the ridge. Because the HCT veins tend to be localized near major fault zones and preferentially

oriented parallel to dikes and hydrothermally-altered fault zones, the HCT veins probably reflect the flow directions of fluids related to magmatic and/or tectonic activity close to the mid-ocean ridge. On the other hand, except for Hole GT2A, the LCT veins tend to show spatial distributions and orientations that differ from those of the HCT veins, and this may indicate that the fluid flow associated with subsequent fracturing in a stress field that differed from that near the ridge, and some of this fracturing may represent thermal cracking (Korenaga, 2007).

4.5 Estimation of paleo-permeability and implications for fluid flow in the oceanic crust

To estimate the permeability structure of each vein system at the time when those veins were open fractures and acted as conduits for fluid (i.e., paleo-permeability), we applied two methods of determining the fractured-rock permeability based on the geometry and abundance of the HCT and LCT veins. First, to calculate the spatial variations in the paleo-permeability of the HCT and LCT vein systems for each borehole, we used an equivalent channel model combined with a parallel plate concept (Norton & Knapp, 1977; Walsh & Brace, 1984). The equivalent channel model is a relatively straightforward way of estimating the bulk permeability of the core samples on a variety of scales (Gilbert et al., 2018). However, it is difficult to obtain directional permeability. Therefore, to evaluate the three-dimensional permeability and the anisotropy of each vein system, we also applied Oda's permeability tensor theory (Oda, 1985) to the three-dimensional orientation data obtained in the contiguous intervals (Figure 4.11) by using vein orientation data to calculate the permeability tensor.

The following assumptions were made when estimating paleo-permeability using the equivalent channel model and permeability tensor theory, based on the work of previous reserachers (Ioannou & Spooner, 2007).

1. The host rock is generally intact and fluid flow occurs only along fractures. Thus, in intervals where no veins are detected, the permeability is set to 0.
2. The shape of a fracture is approximately that of a disk (i.e., penny-shaped), and the permeability of rock containing penny-shaped fractures is defined as the paleo-permeability of the veins.
3. The vein aperture is comparable to the original fracture aperture before the precipitation of minerals.

4. All fractures are fully connected, as all the veins trace the flow of fluids (Hosono et al., 2022).
5. All fractures of a given vein system (i.e., the HCT and the LCT veins) were open at the same time.

Given these assumptions, the permeabilities modeled should be interpreted as a first-order approximation of the maximum values for each vein system (Gilbert et al., 2018; Ioannou & Spooner, 2007). The magnitude and spatial variations of the calculated permeabilities for each vein system are then compared with permeabilities measured directly in the laboratory and within the *in situ* oceanic crust. We are then in a position to discuss the potential role millimeter-wide fractures play during the fluid flow in the oceanic crust.

4.5.1 Paleo-permeability profile based on the equivalent channel model

The permeability of rock containing a fracture network k can be given by the equivalent channel model (Walsh & Brace, 1984) as follows:

$$k = \frac{\langle t \rangle^2 \phi}{12\tau}, \tag{4.7}$$

where $\langle t \rangle$ is the average fracture aperture, ϕ is the porosity, and τ is the tortuosity of the fracture network, which is a parameter defined as the ratio of the apparent length of a fracture to its true length. The porosity of the flow channels can be expressed by the parallel plate concept as follows:

$$\phi = n\langle t \rangle, \tag{4.8}$$

where n is the fracture density (Norton & Knapp, 1977). Combining Equations 4.7, 4.8, we can calculate the bulk permeability from the vein density and aperture as follows:

$$k = \frac{n\langle t \rangle^3}{12\tau}. \tag{4.9}$$

Using Equation 4.9, we determined the bulk permeabilities of a given vein system from the average vein density and aperture for every 1 m depth, 10 m depth, and the total depth in each hole (Figure 4.13). Since the tortuosity τ is not measurable from our data, we assumed $\tau = 1$, and the calculated permeability should therefore be considered as the maximum value. The HCT and LCT vein systems show similar values of borehole-average permeability (~10^{-11}

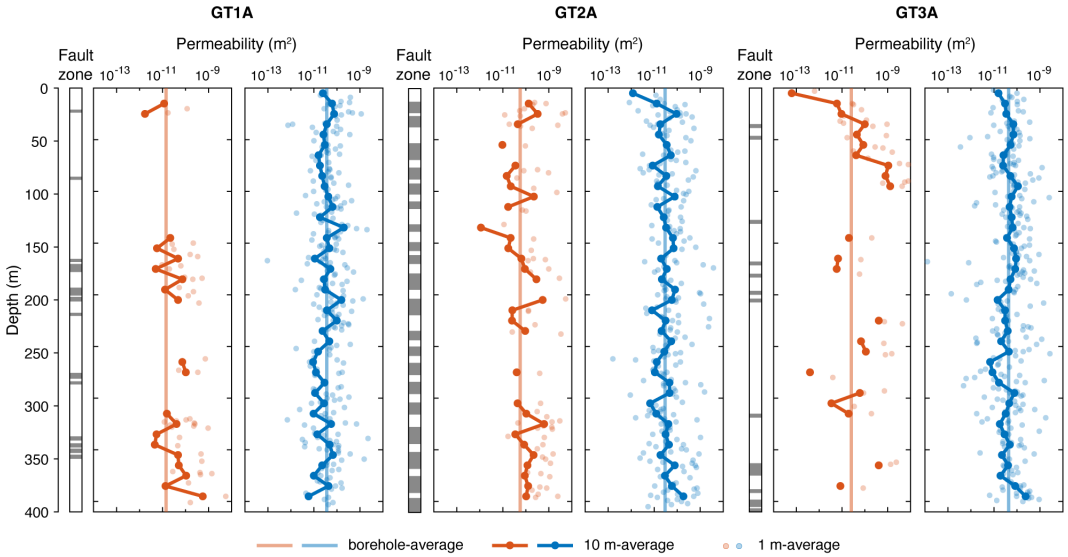

Figure 4.13 Variations in the bulk permeability of the HCT and LCT vein systems with depth, calculated for every 1 m depth (pale circles), 10 m depth (dark lines and circles), and the whole depth of the boreholes (pale lines) based on the equivalent channel model.

m^2), although their total abundances differ by one order of magnitude (Table 4.2). This could be because the HCT veins tend to have larger apertures than the LCT veins. We also found that the spatial variations of 1 and 10 m average permeabilities are different for the HCT and LCT vein systems. The HCT vein system has sporadic high-permeability zones (10^{-12}–10^{-8} m^2) in the boreholes, whereas the LCT vein system has pervasive high-permeability zones in the boreholes. Such a difference may indicate that the fluid flow associated with the LCT vein system had a much larger spatial extent and fluid flux in the oceanic crust than the HCT vein system. This result is consistent with a much larger amount of heat and chemical exchange taking place during off-axis low-temperature fluid circulation than during on-axis high-temperature hydrothermal circulation, which is suggested by heat flow measurements on the seafloor (Elderfield & Schultz, 1996; Stein & Stein, 1994). Also, as shown by the depth variations of vein densities (Figure 4.9), the high-permeability zones of the HCT vein system seem to be localized near major fault zones. This implies that the permeability structure during relatively high-temperature hydrothermal circulation near the ridge axis may be controlled by faults, as also indicated by geological and geochemical analyses (Greenberger et al., 2021; Zhang et al., 2021).

The borehole-average permeabilities calculated from our data are in good agreement with field-based calculations for the crustal sequence of ophiolite settings (Nehlig & Juteau, 1988; van Everdingen, 1995). However, these values are several orders of magnitude higher than

those obtained in laboratory experiments on basaltic and gabbroic rocks (e.g., Brett-Adams et al., 2021; Christensen & Ramananantoandro, 1988; Fortin et al., 2011; Gilbert & Bona, 2016; Karato, 1983; Katayama et al., 2020; Nara et al., 2011). This difference possibly reflects the scale of fractures. As shown in Equations 4.7, 4.9, fracture permeability depends explicitly on the fracture aperture and hence changes drastically by several orders of magnitude depending on the measurement scale, even for the same fraction of fractures (i.e., porosity). Fractures (cracks) in samples used in laboratory experiments typically have apertures of a few microns (Fortin et al., 2011; Nara et al., 2011), which is ~3 orders of magnitude smaller than the apertures of veins in the core sections we examined (Figure 4.10). Our data and calculations suggest that the larger-scale fractures can control the macroscopic flow of fluids in relatively high- and low-temperature systems in the oceanic crust. Although the contribution of microcracks to macroscopic fluid flow in oceanic crust can be limited, they may play a role in alteration and subsurface biosphere activity on a grain-scale, particularly at depths where the large-scale veins are absent, as identified for the HCT vein systems in Holes GT3A and GT1A (Figure 4.13).

The *in situ* permeability of present-day oceanic crust has been obtained from measurements using boreholes at the seafloors, such as packer injection tests and temperature and flow meter logs. Figure 4.14 shows the permeability structure at *in situ* depths of the oceanic crust that correspond to the depths in Holes GT1A, GT2A, and GT3A correspond, with the *in situ* permeabilities obtained at ocean floors of various ages and depths plotted for comparison (Becker & Davis, 2003; Fisher, 1998). The *in situ* bulk permeabilities determined for the upper parts of young (~0.6–3.9 Ma) oceanic crust range from 10^{-12} to 10^{-10} m^2 (Becker & Davis, 2003; Fisher & Becker, 2000), which is similar to the borehole-average permeabilities of the crustal sections of the Samail ophiolite calculated from our data. However, the permeabilities obtained from *in situ* packer injection tests conducted in 6 Ma crust are 10^{-18}-10^{-17} m^2 at depths of the sheeted dike complex (Becker & Fisher, 2000). This value is several orders of magnitude lower than the maximum model permeabilities in our calculations, including the paleo-permeability of the HCT vein system in Hole GT3A, which corresponds to the sheeted dike complex of the Samail ophiolite. This difference indicates that the fractures become filled with minerals deposited by circulating hydrothermal fluids, which lowers the aperture (t) and alters the geometry of the fracture network (τ), resulting in lower permeability in the present-day oceanic crust (Fisher, 1998; Gilbert et al., 2018; Ioannou & Spooner, 2007; Nehlig et al., 1994; van Everdingen, 1995). However, our calculations show that the lower oceanic crust, as well as the upper crust, may have had markedly high permeability immediately

after the formation of fractures related to the HCT and LCT vein systems.

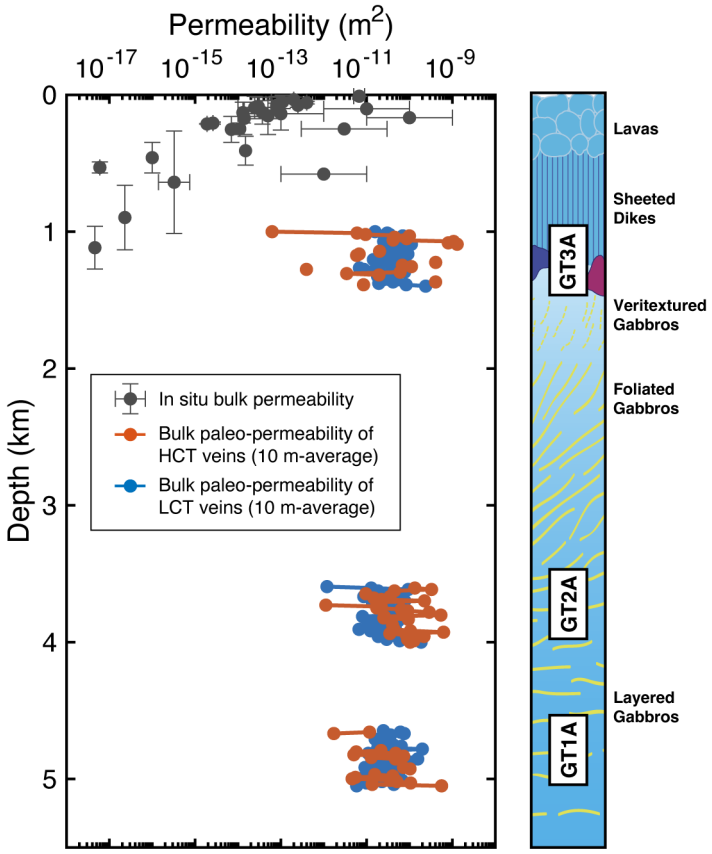

Figure 4.14 Permeability structure at the *in situ* depth of the oceanic crust corresponding to depths in Holes GT1A, GT2A, and GT3A of the Oman Drilling Project, with the generalized ophiolite stratigraphy showing the approximate original depths of each hole in the oceanic crust. *In situ* bulk permeabilities measured by packer tests and estimated from temperature and flow meter logs using boreholes at the present-day oceanc floor are also plotted for comparison. The *in situ* bulk permeability data are compiled from Fisher (1998) and Becker & Davis (2003).

4.5.2 Permeability anisotropy based on permeability tensor theory

To evaluate the three-dimensional anisotropy of permeability in the HCT and LCT vein systems, we coupled the geometry of the detected veins in the contiguous intervals of each hole (Figure 4.11) with the permeability tensor theory proposed by Oda (1985). The three-dimensional characteristics of penny-shaped fractures can be expressed by the fracture radius r, the fracture aperture t, the unit normal vector of a fracture $\boldsymbol{n}$, the fracture surface area S, and the number of fractures per unit volume ρ (i.e., volume density). Using the strike θ and dip angle ψ of a fracture, the direction cosines of the unit normal vector $\boldsymbol{n}$ can be written as

follows:

$$\boldsymbol{n} = \begin{pmatrix} \sin\psi\cos\theta \\ \sin\psi\sin\theta \\ \cos\psi \end{pmatrix}. \tag{4.10}$$

Using the vector $\boldsymbol{n}$, a second-rank symmetric tensor N_{ij}, which is referred to as the fabric tensor, can be defined as follows:

$$N_{ij} = \int_{\Omega/2} n_i n_j 2E(\boldsymbol{n}) d\Omega, \tag{4.11}$$

where Ω is the entire solid angle and $E(\boldsymbol{n})$ is a density function that describes the statistical distribution of $\boldsymbol{n}$ (Oda, 1982). The fabric tensor N_{ij} quantifies the intensity of the three-dimensional orientation of fractures and is determined from the strikes and dip angles of veins detected in the XCT images. By combining the fabric tensor with the geometric characteristics of fractures, directional permeability can be calculated as a tensor. According to Oda (1985), the permeability tensor is given as follows:

$$k_{ij} = \frac{\lambda}{12}(P_{kk}\delta_{ij} - P_{ij}), \tag{4.12}$$

where λ is a non-dimensional parameter that represents the connectivity of the fracture network (i.e., connectivity index) and ranges between 0 and 1. The tensor P_{ij} is a second-rank symmetric tensor that depends only on the geometry of fractures, and $P_{kk} = P_{11} + P_{22} + P_{33}$. When the geometric parameters t, r, and ρ are statistically independent, the tensor P_{ij} is given as follows:

$$P_{ij} = \pi\rho\langle r^2\rangle\langle t^3\rangle N_{ij}, \tag{4.13}$$

where $\langle\rangle$ denotes the average value. Although ρ and r cannot be determined from our data, P_{ij} can be calculated by the vein aperture t and the number of veins per unit length (vein density) based on the stereological method (Oda, 1985; Oda et al., 2002) as follows:

$$P_{ij} = S_0\langle t^3\rangle N_{ij}, \tag{4.14}$$

where

$$S_0 = \pi\rho\langle r^2\rangle = \frac{m(\boldsymbol{q})}{\langle|\boldsymbol{n}\cdot\boldsymbol{q}|\rangle}, \tag{4.15}$$

and

$$\langle|\boldsymbol{n}\cdot\boldsymbol{q}|\rangle = \int_{\Omega} |\boldsymbol{n}\cdot\boldsymbol{q}| E(\boldsymbol{n}) d\Omega. \tag{4.16}$$

The parameter S_0 is the fracture density defined by the surface area per unit volume of the analyzed fracture (or vein), $\boldsymbol{q}$ is the unit vector of the borehole, $m(\boldsymbol{q})$ is the intersection number per unit length, and $\boldsymbol{n} \cdot \boldsymbol{q}$ is the inner product between unit vectors $\boldsymbol{n}$ and $\boldsymbol{q}$ (Hosono et al., 2022).

The permeability tensor can be reduced to its three principal (diagonal) components, which are referred to as the maximum (k_1), intermediate (k_2), and minimum (k_3) principal permeabilities (van Everdingen, 1995). These are the eigenvalues of the tensor and the associated eigenvectors give the orientations of the principal permeabilities. We define the degree of permeability anisotropy as the ratio of the maximum to minimum principal permeabilities k_1/k_3 (Lang et al., 2014). In the calculations, the connectivity index λ is set as 1.

Table 4.3 Summary of vein data used for stereographic projections and permeability tensor calculations.

Hole	Interval (m)	Vein type	$m(\boldsymbol{q})$	$\langle t \rangle$ (mm)	S_0 ($\mathrm{mm}^2/\mathrm{mm}^3$)	k_{ii} (m^2)	k_1/k_3
GT1A	306–353	HCT	19	0.91	0.06	4.00×10^{-12} 3.34×10^{-12} 8.16×10^{-13}	4.90
GT2A	152–240	HCT	14	1.89	0.03	1.79×10^{-11} 1.55×10^{-11} 3.98×10^{-12}	4.50
GT3A	23–59	HCT	12	1.08	0.04	4.18×10^{-12} 3.81×10^{-12} 8.39×10^{-13}	4.98
GT1A	306–353	LCT	53	0.77	0.07	2.29×10^{-12} 2.21×10^{-12} 7.19×10^{-13}	2.90
GT2A	152–240	LCT	74	1.01	0.03	2.36×10^{-12} 2.20×10^{-12} 1.01×10^{-13}	2.34
GT3A	23–59	LCT	55	0.72	0.13	3.67×10^{-12} 3.18×10^{-12} 1.25×10^{-12}	2.94

Table 4.3 summarizes the calculated principal permeabilities of the HCT and LCT vein systems in the contiguous intervals of each hole and the related parameters used for the calculations. The maximum principal permeability k_1 ranges from 10^{-13} to 10^{-11} m^2 for the HCT and LCT vein systems, which is consistent with the 10 m- and borehole-average bulk permeabilities determined by the equivalent channel model (Figure 4.13). The degree of anisotropy (k_1/k_3) ranges from 4.50 to 4.98 and from 2.34 to 2.94 for the HCT and LCT vein systems, respectively. Given that the HCT vein system in these holes may be associated with local tensional faulting near the ridge, the permeability of the HCT vein system in the direction parallel to the fault may be ~5 times greater than that in the orthogonal direction. This value is similar to that estimated around a seismogenic zone based on permeability tensor theory from the geometry of quartz-veins (Hosono et al., 2022). However, the electromagnetic surveys conducted on Pacific lithosphere aged 33 Ma have shown that the electrical conductivity in the oceanic crust, which is closely related to permeability, is 18–36 times higher in the paleo mid-ocean ridge direction than in the orthogonal paleo-spreading direction (Chesley et al., 2019). They interpreted this anisotropy to have been caused by 0.8–4 mm wide seawater-filled cracks that are perfectly aligned and spaced by 1 m. Although their estimation of the crack aperture and spacing is almost consistent with our data at depths where the permeability tensor was calculated (Table 4.3), our data show that the veins are not perfectly oriented. Therefore, the electrical anisotropy observed in the oceanic crust may be attributed to other characteristics of the fractures. The transport properties, including permeability and electrical conductivity, potentially depend on the geometry of the fracture network, which is expressed by τ and λ (Guéguen & Dienes, 1989). Although we assumed those parameters as a constant, such parameters potentially have anisotropy under anisotropic stress conditions and hence may contribute to the observed anisotropy on the crustal scale. Other geological structures such as macroscopic faults and dikes that exist on a larger scale than hydrothermal veins could also be the direct cause of the observed anisotropy.

4.6 Advantages, limitations, and perspectives

The paleo-permeability method using halves of the drilled cores, as proposed by Gilbert et al. (2018), allowed us to estimate the maximum permeability of the cores of the Oman Drilling Oroject in two dimensions on a variety of scales. In addition to those advantages, our method of using X-ray CT data provides a three-dimensional permeability structure. Furthermore,

different vein minerals and systems, including open fractures, can be classified based on the CT number, which reflects the chemical composition and density of the vein-filling material.

Our method depends highly on the quality of the CT image, such as spatial resolution. For example, the veins with apertures smaller than the resolution cannot be observed in the CT images and hence are not detected, although the contribution of such invisibly small veins to the bulk permeability may be negligible compared with the contribution of millimeter-wide veins. It is also difficult to detect the veins filled by a mineral with a CT number similar to that of the surrounding material. It should be noted that our analysis may have overlooked veins filled with such minerals. These problems may be addressed by advanced image analysis techniques, such as super-resolution and feature extraction of images based on various data-driven approaches (e.g., Al-Sit et al., 2015; Kalfarisi et al., 2020; Zhao et al., 2023). In addition, because the core may rotate during recovery, the original geographic orientations may be modified and differ depth by depth, as shown in the Oman Drilling Project (Kelemen et al., 2020a). To obtain the whole-depth profile of anisotropies in vein orientation and permeability, reliable references such as paleo-magnetic properties would be required to reorientate the cores.

Our data provides the first-order magnitude of the permeability structure of the drilled cores using XCT core images. Observations and analyses using XCT data have been applied to drilled cores to extract the chemical and physical properties of the core samples (e.g., Gupta et al., 2019; Okazaki et al., 2021; Tonai et al., 2019; Williams et al., 2018). Further studies of physical and chemical properties that combine the used of our method and other XCT-based methods that use advanced analytical techniques may shed further light on the understanding of subsurface geological processes.

4.7 Conclusions

We used X-ray CT core images to investigate the distribution and geometry of veins preserved in the crustal sequences of the Samail ophiolite that were sampled during the Oman Drilling Project. Applying fracture fluid-flow models to the geometric data for the detected veins, we found that the High-CT and Low-CT vein systems both yielded permeabilities of 10^{-13} to 10^{-9} m^2, values that are similar to the bulk permeabilities measured *in situ* uppermost parts of oceanic crust. This indicates that millimeter-wide fractures can control the crustal-scale permeability down to the depths of the lower oceanic crust. However, these vein systems show different permeabilities with depth, possibly reflecting the differences in the spatial

heterogeneity of high- and low-temperature fluid circulations in oceanic crust. The calculated permeability tensor indicates that the paleo-permeability anisotropy can be less than that inferred from in situ electromagnetic surveys in the oceanic crust. This implies that the crustal-scale permeability anisotropy may be attributed to other geometrical parameters that are potentially anisotropic such as fracture connectivity and tortuosity.

Chapter 5

General discussion and conclusions

5.1 Upscaling of seismic velocity and electrical resistivity of oceanic crust

In addition to cracks, fractures may have a substantial impact not only on permeability but also on seismic velocity and electrical resistivity. To understand the subsurface fluid flow and related geological processes, the effects of cracks and fractures should be separately inferred from the observed geophysical data. This requires the development of novel models that take into account both effects of crack and fracture on seismic velocity and electrical resistivity. In this chapter, we attempt to establish the upscaled physical property model based on the dataset and insights from the previous chapters. First, the heterogeneity of the fracture distribution is evaluated in the same manner as for microcracks, and an appropriate model for calculating seismic velocities is examined. Utilizing the model, a seismic velocity model that accounts for both microcracks and fractures is proposed. Then, the percolation of the fracture network is subsequently discussed to take into account its effect on resistivity. Finally, these models of seismic velocity and electrical resistivity are combined to formulate a joint model for interpreting geophysical observations.

5.1.1 Heterogeneity of fracture distribution

As discussed in Chapter 3, quantifying the effect of water-saturated porosity on the rock's elastic properties requires evaluation of the REV of the porosity structure. Therefore, the spatial heterogeneity of the veins that were identified in Chapter 4 was estimated using the

depth distributions of the veins, in a similar manner applied to MSCL-W data as described in Chapter 3. The depth variations in the paleo-porosity and paleo-permeability for LCT-veins of Holes GT1A, GT2A, and GT3A were used for the analyses (Figure 5.1). The changes in the mean values of each physical variable and their magnitude of relative gradient errors (ϵ_g) as the window length were systematically increased were computed. The maximum window length was set to 100 m, and the window was moved throughout each hole by every 20 m depth. The REV criterion was defined here as $\epsilon_g = 0.1$ so that the mean porosity and permeability clearly reach the plateaus.

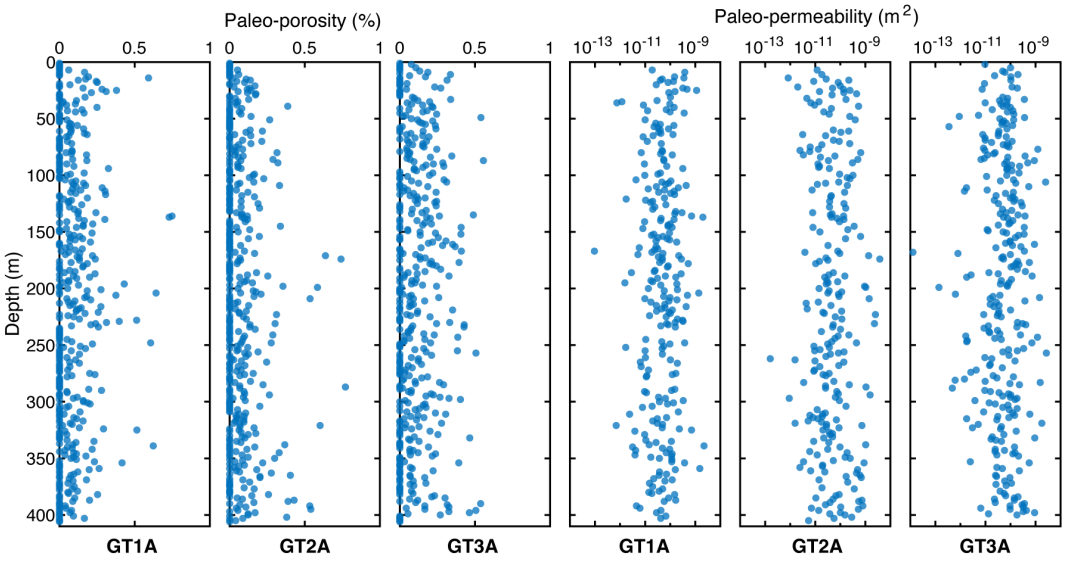

Figure 5.1 Downhole variations in paleo-porosity and paleo-permeability of LCT-veins for Holes GT1A, GT2A, and GT3A.

Figure 5.2 shows the calculated mean porosity and permeability and the magnitude of relative gradient errors for those variables as a function of the window length. The colors indicate the results of each hole. Similar to the variables associated with microcracks, the porosity and permeability of the LCT-veins converged to constant values as the window length increased. The L_{REV} estimated using the $\epsilon_g < 0.1$ ranges from 6–30 m for each hole (Figure 5.3), which is similar or one order of magnitude larger than that estimated for crack density and P-wave velocity of Hole GT3A. This means that if the seismic velocity is influenced by large-scale fractures, the velocity can reflect the characteristics of the fracture network on a scale of several or tens of meters.

To examine the validity of theoretical models to compute the effect of fractures on seismic velocity under water-saturated conditions, the critical frequency at which the wave-induced

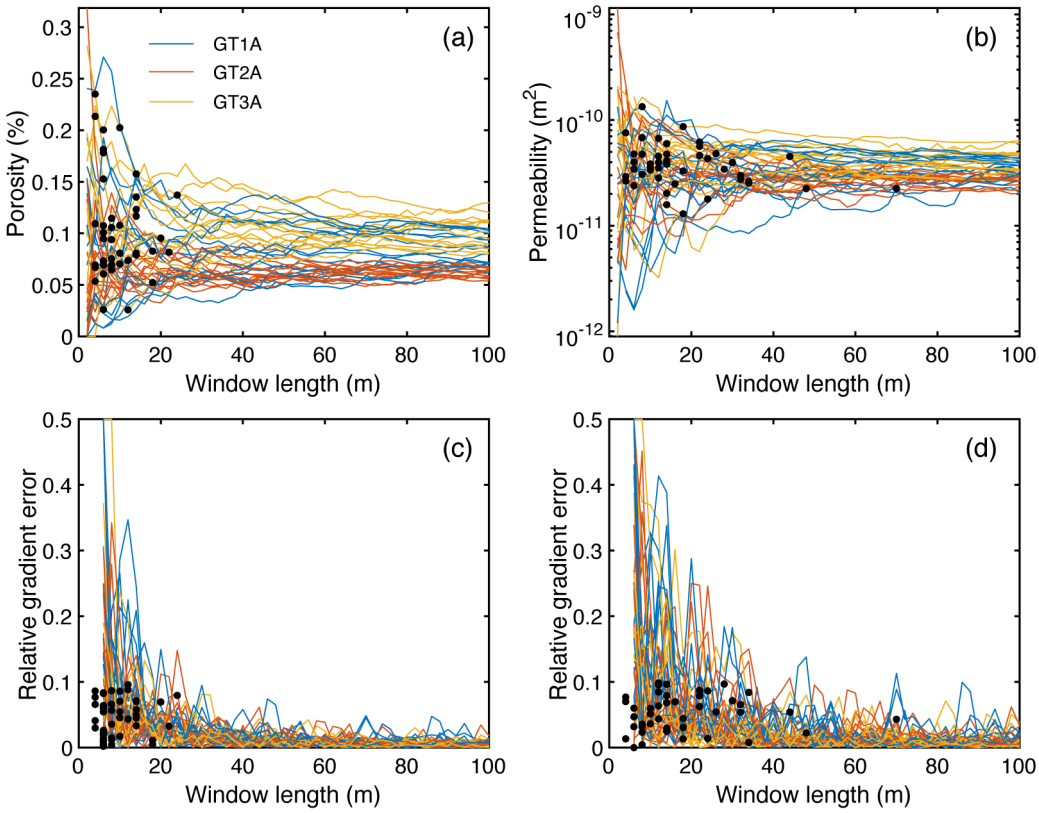

Figure 5.2 (a,b) Changes in mean vein (fracture) porosity and permeability, and (c,d) the relative gradient errors as a function of the window length. The color indicates the depth of the center of the moving window. Black dots indicate L_{REV}.

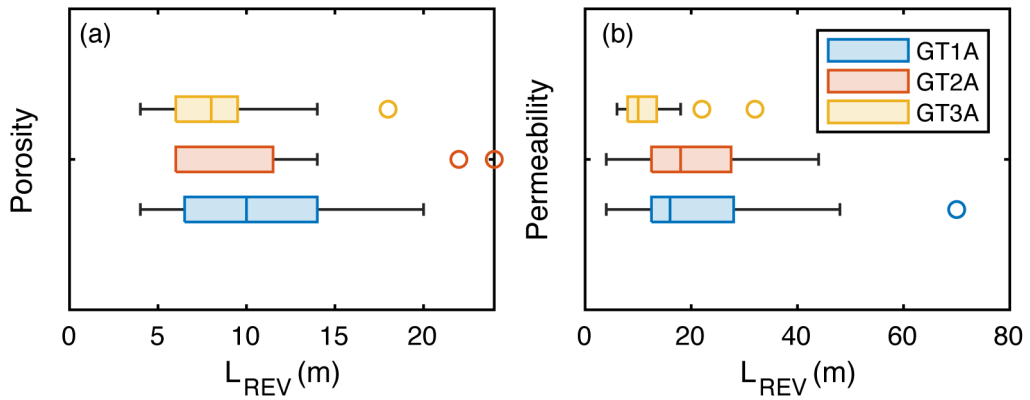

Figure 5.3 Boxplots of the length of REV (L_{REV}) for vein (fracture) porosity and permeability that are determined using the criterion of $\epsilon < 0.1$.

fluid flow can fully diffuse over the scale of the REV during the wave propagation was calculated. The rate of fluid flow within a rock was computed using Equation 4.17. The permeability of the fractured rock on the scale of the REV was taken to be $k = 3.3 \times 10^{-11}$˘4.8×10^{-11} m^2, based on the average permeability determined for the LCT-vein of Hole GT3A (Figure 5.2b). The viscosity and drained bulk modulus were set to 10^{-4} Pa.s and 11.8 GPa, respectively.

Figure 5.4 shows the calculated critical frequencies for the fractured rock as a function of the REV length, plotted with the results for the microcracks. In the region above the red line, the fluid within the fracture REV cannot follow the rate of loading, resulting in unrelaxed conditions, whereas, in the region below the red line, the fluid can fully diffuse within the REV during the loading, resulting in relaxed conditions. As the fracture REV has a scale of several meters or more, it cannot be captured as a homogeneous pore structure at the frequency of the sonic logging velocity. This means that the fracture characteristics extracted from the logging velocities reflect the localized structure and care must be taken when extrapolating it to larger scales. At seismic frequencies, however, the fracture network can be considered a homogeneous structure (domain F in Figure 5.4). The domain F locates below the critical frequencies estimated from the fracture permeability, suggesting that the seismic velocities "see" the relaxed (undrained) conditions.

5.1.2 Seismic velocity

Ultrasonic velocity and resistivity datasets measured on the core samples from Hole GT3A indicate that seismic velocities at a macroscopic scale possibly reflect microcrack structure under unrelaxed conditions (Chapter 2). This suggests that the effect of water-saturated cracks on seismic velocity can be modeled by effective medium theory, which postulates isolated cracks. On the other hand, paleo-porosity and permeability estimations from the spatial abundance of millimeter-wide vein minerals in the core sections indicate that the relatively large-scale fractures can undergo either unrelaxed conditions or relaxed (undrained) conditions during the seismic wave propagation. This implies that one needs to combine effective medium theory and Gassmann's equation when modeling the effect of water-saturated fractures on the seismic velocities.

Elastic properties of rock with multi-scale porosities can be modeled based on the differential self-consistent scheme of effective medium theory (Bailly et al., 2019). The elastic moduli of the cracked medium $M_{\text{eff}}^{\text{crack}}$ under water-saturated conditions are assumed to be the one of a

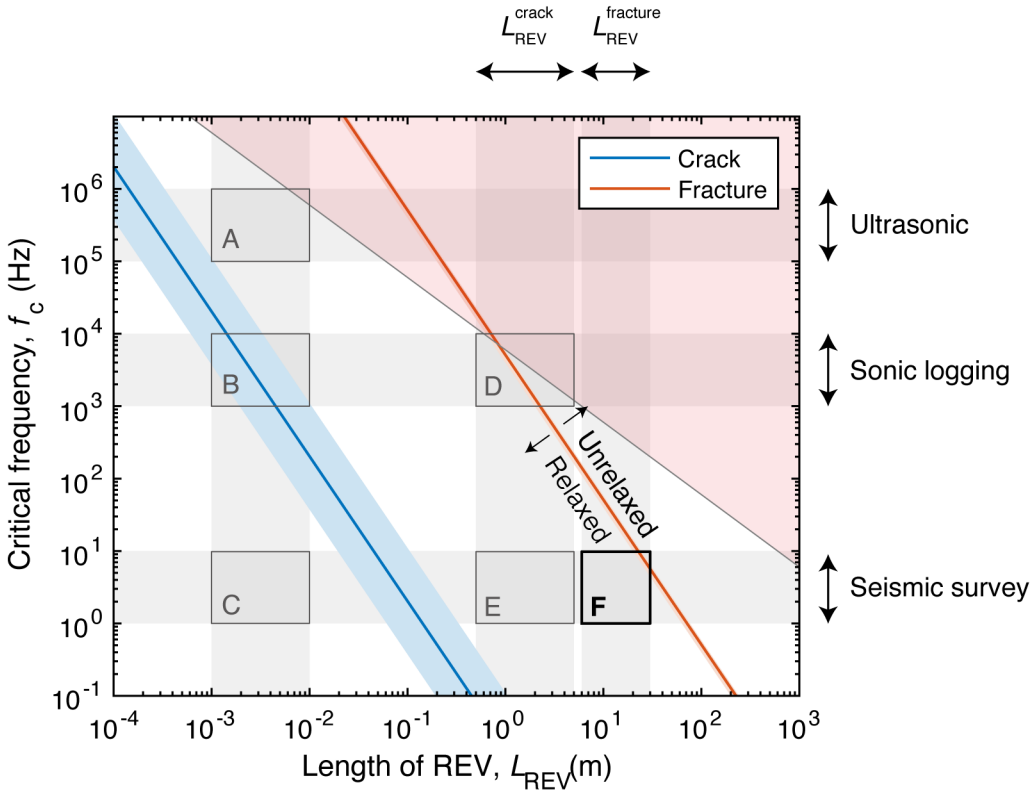

Figure 5.4 Critical frequency at which unrelaxed/relaxed transition occurs in a cracked rock (blue line) and a fractured rock (red lines) as a function of the length of REV. The red-colored region denotes the range of wavelengths greater than REV. The domain F is newly defined for the range of the fracture REV and seismic frequency.

matrix containing a given population of cracks as:

$$M_{\text{eff}}^{\text{crack}} = f(x_{\text{crack}}, M_0), \tag{5.1}$$

where x_{crack} is the crack microstructural parameters such as crack density, crack porosity, and aspect ratio, and M_0 is the crack-free matrix modulus. Meanwhile, when considering the effective elastic properties of a medium containing not only cracks but also fractures at a larger scale ($M_{\text{eff}}^{\text{fracture}}$), the matrix modulus can be assumed to be one of the effective medium containing cracks as defined above, such that

$$M_{\text{eff}}^{\text{fracture}} = g(x_{\text{fracture},}, M_{\text{eff}}^{\text{crack}}), \tag{5.2}$$

where x_{fracture} is the parameters related to the abundance and geometry of fractures, such as fracture porosity. Based on the REV estimations presented in the previous chapters and sections, the function f corresponds to the effective medium model such as Kachanov (1994)'s equations, whereas the function g corresponds either to the effective medium model or combined use of the effective medium model and Gassmann's equation.

Figure 5.5 shows the upscaled seismic velocity computed as a function of crack and fracture porosities, with the crack-free velocities of $V_{\text{P}}^0 = 7.0$ km/s and $V_{\text{S}}^0 = 3.8$ km/s. The aspect ratio of the crack was assumed to be 0.002, which is the median value of those obtained for the discrete laboratory samples of Hole GT3A as presented in Chapter 2. The aspect ratio of fracture was also assumed to be 0.002, which is similar to that estimated for vein minerals in Cyprus ophiolite (van Everdingen, 1995). The boxplots of the macroscopic crack and fracture porosities of Hole GT3A, which were determined from MSCL-W data and vein abundances, respectively, are also shown in Figure 5.5 and the ranges of seismic velocity corresponding to those porosities are highlighted as bold lines. First, V_{P} and V_{S} decrease systematically but differently with increasing crack porosity. These changes are more moderate than the conventional interpretation assuming undrained conditions for the crack effect (dashed lines), in particular for V_{S}. This results in an increase in $V_{\text{P}}/V_{\text{S}}$ from 1.84 to 2.05–2.22 in the range of crack porosity of Hole GT3A, which is also relatively smaller than that based on the conventional interpretations. Given that the crack density should be $\rho_c < 1$ for DEM method (Le Ravalec & Guéguen, 1996), $V_{\text{P}}/V_{\text{S}}$ is not expected to exceed ~2.2 for the aspect ratio of 0.002, whereas $V_{\text{P}}/V_{\text{S}}$ for undrained conditions can increase up to ~3. Meanwhile, in this new model, the effect of millimeter-wide fractures are further introduced into the effective medium containing the cracks. V_{P} and V_{S} subsequently decrease with the addition

of fracture porosity along with the trend for undrained conditions. Since the shear modulus is independent of the presence of pore water under undrained conditions, the decrease in V_S is significant relative to that in V_P. As a result, the impact of fracture porosity on V_P/V_S is significant relative to that of cracks. In the range of the fracture porosity detemined for Hole GT3A, V_P/V_S can increase up to ~2.3.

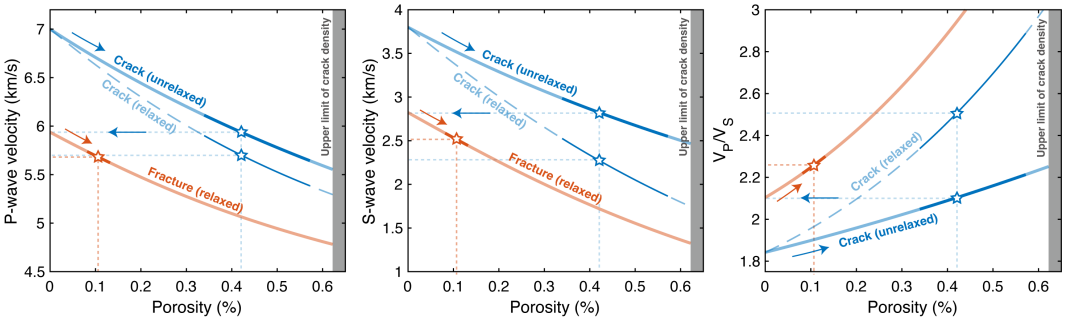

Figure 5.5 Upscaled (a) P-wave velocity (b) S-wave velocity, and (b) V_P/V_S as a function of crack and fracture porosities. The range of crack and fracture porosities at each REV scale of Hole GT3A are highlighted as bold lines, and the median values are denoted as star symbols. Gray areas correspond the upper limit of crack density parameter for DEM method ($\rho_c > 1$).

High V_P/V_S is often observed within subducting oceanic crust by seismological surveys. Audet et al. (2009) reported the anomalouly high V_P/V_S of 2.35 $\pm$ 0.1 at Cascadia subduction zone. They concluded that such seismic anomalies can be caused by the presence of extremely high pore pressure close to the lithostatic pressure which is enough high to remain the cracks open within the deep oceanic crust. Pimienta et al. (2018) suggested a link between those V_P/V_S anomalies and elastic properties under undrained conditions based on the laboratory measurements on frequency-dependent elastic moduli. Given that the V_P/V_S measured for the discrete core samples from Hole GT3A is at most ~2.2 (Chapter 2), such high V_P/V_S anomalies may be associated with the presence of homogeneously distributed large-scale fractures.

5.1.3 Electrical properties

In Chapter 2, the cross-property relationship between elastic and electrical properties, which can quantify the degree of connectivity of the crack network as well as the abundance and geometry of cracks, were developed based on the existing theoretical models. Although connectivity is an important factor to evaluate the nature of subsurface fluid flow via permeability, the permeability depends much more strongly on the scale of the void, as demonstrated in Chapter 3. To quantitatively assess subsurface fluid flow, it is necessary to

determine the scale of the pore structure extracted from geophysical data. Upscale modeling of resistivity is therefore performed in the same manner as for seismic velocities above, taking into account the effects of both cracks and fractures.

Electrical conductivity of a cracked rock $\sigma_{\text{eff}}^{\text{crack}}$ can be modeled as a function of crack porosity ϕ_{crack} and connectivity C_{crack} as:

$$\sigma_{\text{eff}}^{\text{crack}} = f(\phi_{\text{crack}}, C_{\text{crack}}, \sigma_{\text{fluid}}, \sigma_0), \tag{5.3}$$

where σ_{fluid} is the fluid conductivity and σ_0 is the matrix conductivity. The crack connectivity C_{crack} is a non-dimensional parameter that can be computed as a function of crack density ρ_{crack} based on the percolation theory as:

$$C_{\text{crack}} = g(\rho_{\text{crack}}). \tag{5.4}$$

Analogous to the case of seismic velocity, the electrical conductivity at the fracture scale can be modeled by considering the matrix as the effective medium equivalent to the cracked rock. Then, the effective conductivity of the fractured medium $\sigma_{\text{eff}}^{\text{fracture}}$ is given by

$$\sigma_{\text{eff}}^{\text{fracture}} = f(\phi_{\text{fracture}}, C_{\text{fracture}}, \sigma_{\text{fluid}}, \sigma_{\text{eff}}^{\text{crack}}), \tag{5.5}$$

where ϕ_{fracture} is the fracture porosity and C_{fracture} is the fracture connectivity. Nevertheless, even if the fractures are isolated from each other, if the crack network pervasively spreads over the scale of fracture REV, it is expected to act as a conduit for electrical conduction between the fractures. Assuming such a situation, the fracture connectivity may be expressed as a superposition with the crack connectivity as:

$$C_{\text{fracture}} = g(\rho_{\text{fracture}}) + C_{\text{crack}}. \tag{5.6}$$

Note that, C_{crack} and C_{fracture} need to satisfy $0 \leq C_{\text{crack}}, C_{\text{fracture}} \leq 1$.

Figure 5.6 shows the upscaled electrical resistivity computed as a function of crack and fracture porosities, with reference conductivities of $\sigma_{\text{fluid}} = 5$ S/m and $\sigma_0 = 10^{-5}$ S/m. The aspect ratios of crack and fracture to calculate the porosities were set to be 0.002. As the crack porosity increases and exceeds the percolation threshold (0.08% for the aspect ratio of 0.002), the resistivity decreases by several orders of magnitude, followed by a linear and gradual decrease. Given the range of the crack porosity of Hole GT3A, the resistivity ranges

from 135 Ωm to 153 Ωm, and the crack interconnection has completed ($C_{\mathrm{crack}} = 1$). As a result, even if the fracture porosity is added to this cracked rock, the resistivity does not change significantly as shown when the crack porosity is added to the intact matrix. This indicates that the bulk electrical resistivity of the oceanic crust can be controlled dominantly by crack-scale conduction, in contrast to seismic velocity.

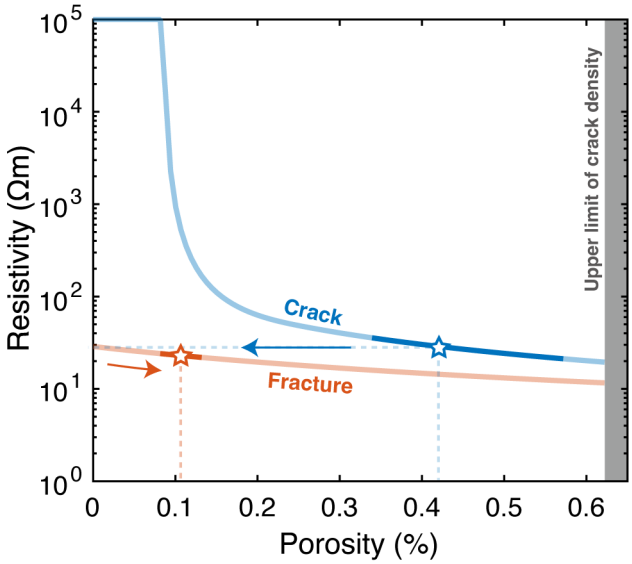

Figure 5.6 Upscaled electrical resistivity as a function of crack and fracture porosities. The range of crack and fracture porosities at each REV scale of Hole GT3A are highlighted as bold lines, and the median values are denoted as star symbols. Gray areas correspond the upper limit of crack density parameter for DEM method ($\rho_c > 1$)

5.2 Perspectives and future tasks

5.2.1 How can we extract the effects of cracks and fractures separately from the observed data?

Althoug the new upscaled physical properties models were developed, using independently these models cannot be sufficient to extract separately the contributions of the cracks and fractures. Given that the cracks and fractures can affect differently on the seismic velocity and electrical resisitvity, joint interpretations using these models can be useful to infer the contrbbutions of cracks and fractures separately. However, there are still problems to be overcome, such as quantification of the percolation process of fractures and cracks, and the difference in spatial resolutions between seismic and electrical observations.

Instead, combining the seismic velocity with seismic attenuation data may be useful. Wave-

induced fluid flow results in not only the dispersion of elastic properties but also the loss of energy, which is one of the mechanisms of seismic attenuation (Mavko et al., 2020; Müller et al., 2010; Pride et al., 2004). Therefore, the seismic attenuation is thought to be an indicator of subsurface fluid migration, and the relationship between the attenuation and various geodynamic processes has been commonly discussed (Eberhart-Phillips et al., 2017; Guerin et al., 2008; e.g., Kita et al., 2014; Nakajima & Uchida, 2018). Our data indiate that the seiemic velocities see water-saturated cracks isolated between each REV (i.e., unrelaxed conditions), whereas the velocities see the fluid flow between the fractures REVs (i.e., relaxed but undrained conditions). This means that the seismic attenuation related to the fluid flow could be due mainly to the presence of the fractures.

5.2.2 Pressure effects

The data used in this thesis were measured onborad or obtained at labotarory under room temperature and pressure conditions. However, high pressure and temperature must be applied to the rock at in situ depths of the oceanic crust, and the observed geophysical data possibly includes the effects of such external factors. The temperature at in situ depths of the oceanic crust can be estimated to be from 100 °C to 200 °C, which is not high enough to significantly alter the physical properties of the rocks and cracks (Guéguen & Palciauskas, 1994). Note that the fluid viscosity was taken to be 10^{-4} Pa.s assuming the effect of in situ temperature in the computation of pore pressure equilibration (Chapters 2 and 5). On the other hand, the pressure has a significant impact on the crack-induced changes in physical properties because the cracks tend to close due to the application of pressure (Guéguen & Palciauskas, 1994). The pressure needed to completely close a crack with the initial aspect ratio α can be approximated as

$$P_{\mathrm{c}} \sim E\alpha, \tag{5.7}$$

where E is Young's modulus of the rock (Walsh, 1965). Assuming a density of 3 g/cm^3 and a depth of 3-7 km for the igneous layers of the oceanic crust, the lithostatic pressure within the crust can be approximately 100–200 MPa. Given a typical Young's modulus of the gabbroic rock of $E = 100$ GPa, cracks with an initial aspect ratio smaller than ~0.001 are possibly closed within the plutonic oceanic crust. The aspect ratio of microcracks estimated for Hole GT3A is mostly larger than 0.001 (Chapter 2), so that they can remain open even at in situ depths of the oceanic crust. This suggests that the geophysical properties at such depths may be affected by the presence of water-saturated cracks and fractures.

Nevertheless, the detailed pore structure at such conditions should be examined in terms of both laboratory- and seismic scales. As mentioned above, meanwhile, seismological and electromagnetic observations have indicated the presence of a large amount of pore water within the subducting oceanic crust despite high pressure (e.g., Audet et al., 2009; Kato et al., 2010; Kodaira et al., 2004; Yarce et al., 2019). This is possibly attributed to a reduction in effective pressure due to extremely high pore pressures close to the lithostatic pressure (Saffer & Tobin, 2011). In the context of such extreme pressure conditions, our laboratory data and interpretations may be utilized as an upper bound on crack-induced changes in geophysical properties under water-saturated conditions. In addition, the variations in the crack density and aspect ratio of Hole GT3A inferred from our laboratory measurements could be used for simulating the systematic crack closure due to elevated pressures using Equation 5.7; thereby leading to the prediction of pressure-dependence of seismic velocity and electrical resistivity at the scale of the microcrack REV we estimated.

5.2.3 Anisotropy effects

Our upscaling models assume the isotropic conditions, in which the cracks and fractures are randomly oriented. However, actual oceanic crusts can contain anisotropy of cracks/fractures, in particular for at settings such as mid-ocean ridges and subduction zones with tectonic stress fields (e.g., Tsuji et al., 2011). Indeed, anisotropic clusering of the vein minerals were indentified from our XCT data analyses (Chapter 4). To account for the effect of anisotropy, one should incorpolate the orientation distribution of the cracks/fractures into the theoretical models. For elastic properties, some theoretical models that take into account the anisotropy effect have been proposed by previous studies (Adamus, 2021; e.g., Hudson, 1990; Sayers & Kachanov, 1995). The Kachanov's effecvtive medium models, which are used in this thesis, can be extended to the case where the cracks are anisotropic (see Appendix A). The Gassmann's equations can be also extended to the anisotropy case (Brown & Korringa, 1975), and some previous studies investigate the dispersion of the elastic wave velocities under anisotropic conditions by combining those models (Guéguen & Sarout, 2009, 2011; Schubnel & Guéguen, 2003).

Although there are some models to consider the anisotropy effect on effective electrical properties (Asami, 2002; Han et al., 2020), such models have not been used with the percolation theory. If the cracks/fractures have orientation anisotropy, the probability of crack interconnection will be possibly affected. Although it may be difficult to solve such problems analytically, the anisotropic models are demanded through experimental and/or

numerical studies.

5.2.4 Implications for fluid flow behavior of the oceanic crust

Fluid flow and related geoscientific processes occur in the oceanic crust, such as grain boundary-scale alteration, global carbon cycling, and seismic activity. To understand these processes, it is necessary to understand the scale at which the geophysical data reflect the characteristics of these processes. Our proposed model, which incorporates the scale of cracks and fractures, is expected to provide a basis for understanding the role of pore water in the oceanic crust, although there are still problems to be addressed.

5.3 Summary

The objective of this thesis is to examine the distribution and geometry of cracks/fractures of varying scales in the core samples collected during the Oman Drilling Project and to establish a model to quantitatively interpret the large-scale seismic velocity structure and electromagnetic structure observed in the oceanic crust. Results of laboratory measurements on elastic wave velocities and electrical resistivity using the discrete cubic samples (~8 cm^3) taken from the core sections are presented in Chapter 2. By combining the existing theoretical models proposed by Kachanov (1994) and Guéguen & Dienes (1989), the new model to relate elastic and electrical properties via crack density microstructural parameters, including crack connectivity, was established. Applying the proposed model, the variations in the measured physical properties were quantitatively interpreted in terms of crack density, aspect ratio, and crack connectivity. Furthermore, the model was also successfully applied to the sonic velocities and electrical resistivity data obtained by borehole logging obtained at IODP Hole 1256D. This indicates that the proposed joint model can be used to interpret the geophysical properties at various scales, possibly including in situ scale geophysical data.

In Chapter 3, the spatial heterogeneity of microcrack distributions of Hole GT3A, which affects the choice of model to compute elastic properties under water-saturated conditions, was evaluated. The evaluation utilized the P-wave velocity structure of the whole core sections that was continuously measured by the Whole-round Multi-Scanner Core Logger (MSCL-W) system during the shipboard description campaign (Kelemen et al., 2020d). The results revealed that the structure of microcracks reflected by low-frequency (large-wavelength) seismic velocity can be considered the crack parameters averaged over several-meter scales. This suggests that the wave-induced pore pressure within the REV scale cannot be equilibrated

so that the elastic moduli extracted from seismic velocity can be unrelaxed condition, in contrast to the conventional interpretations.

Whereas the effects of pore-water on the geophysical properties of oceanic crust were examined in Chapters 2 and 3, in terms of microcracks, the natural geological system possibly includes various scale porosities, such as macroscopic fractures. Therefore, in Chapter 4, the spatial distributions and geometry of vein minerals, which can be considered fossilized fractures, appearing in the core sections from the Oman Drilling Project were investigated. Detection of vein appearance and its geometry was carried out using the 3-D X-ray CT images of the drilled cores. As a result, millimeter-wide veins were commonly identified throughout the crustal sections of the Oman ophiolite, with an average spacing of 1–10 m. Applying fracture fluid-flow models to the geometric data for the detected veins, it was found that the millimeter-wide fractures can have permeability of 10^{-13} to 10^{-9} m^2, which is several orders of magnitude larger than that typically measured by laboratory experiments. This indicates that the macroscopic fluid flow in the oceanic crust may be controlled by such relatively large-scale fractures.

Further studies are needed to fully realize the findings and implications of this thesis along the lines discussed above in terms of practical applications and verifications. However, the results reported in this thesis give a systematic and comprehensive relationship between geophysical properties and water-saturated cracks of deep oceanic crust for the first time. The lines of evidence that demonstrate the effect of water-saturated cracks and fractures on seismic and transport properties of oceanic crust can provide new insights into the interpretation of geophysical observations at various tectonic settings. This is of major importance and interest to understand various geoscientific processes that occur in the oceanic lithosphere, including seismic activity at subduction zones, microbial activity, and global mass cycles.

Appendix A. Crack density by Kachanov's effective medium model

A.1 Extra compliance and crack density tensor

In this thesis, the author often attempted to quantify the effect of microcracks on effective elastic moduli via scalar crack density parameter using Kachanov (1994)'s effective medium model. Meanwhile, it is known that Kachanov's model, unlike other similar models such as O'Connell & Budiansky (1974) and Kuster & Toksöz (1974), can express the crack density not only as a scalar but also in the form of a tensor. Using the crack density tensor model enables us to predict/extract crack-induced anisotropy in effective elastic constants. In this Appendix, Kachanov's effective medium model is introduced in a tensor manner.

The application of elastic waves to the crack surface induces a stress field that generates extra strains that are absent in the absence of cracks. These extra strains result in a decrease in the elastic constants of the rock in comparison to crack-free rock. The overall strain on an elastic body containing cracks can be represented as the sum of the average strain in the solid phase and the extra strain resultant from the presence of cracks ϵ_{ij}, as follows:

$$\epsilon_{ij} = S^0_{ijkl}\sigma_{kl} + \Delta\epsilon_{ij}, \tag{A1}$$

where S^0_{ijkl} is the elastic compliance tensor of the crack-free solid phase, and σ_{kl} is the stress tensor applied to the solid phase. The extra compliance due to the presence of cracks can be expressed as:

$$\Delta\epsilon_{ij} = \Delta S_{ijkl}\sigma_{kl}. \tag{A2}$$

Substituting Equation A2 into Equation A1, the overall strain can be given as:

$$\epsilon_{ij} = (S^0_{ijkl} + \Delta S_{ijkl})\sigma_{kl} = S_{ijkl}\sigma_{kl}, \tag{A3}$$

where S_{ijkl} is the effective elastic compliance.

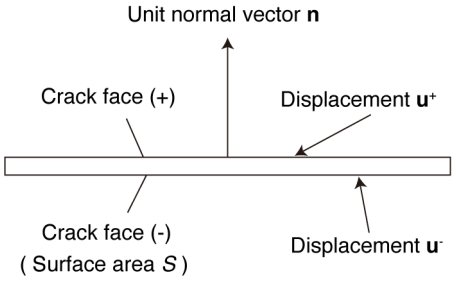

Figure A1 Schematics of a planer crack.

To compute the extra overall strain and compliance, one should initially contemplate a singular crack. When a single isolated crack exists within a solid phase under stress, the extra strain per unit volume (V) resulting from displacement at its crack surface (surface area S) is expressed by the integral over the crack surface area as follows:

$$\begin{aligned} \Delta\boldsymbol{\epsilon} &= \frac{1}{2V}\int_S (\mathbf{un} + \mathbf{nu})dS \\ \Delta\epsilon_{ij} &= \frac{1}{2V}\int_S (u_i n_j + n_i u_j)dS, \end{aligned} \tag{A4}$$

where $\mathbf{u}$ is the displacement vector caused by the stress $\boldsymbol{\sigma}$, and $\mathbf{n}$ is the unit normal vector of the crack. If the crack is planer-shaped, the extra strain can be rephrased as follows:

$$\Delta\boldsymbol{\epsilon} = \frac{1}{2V}\int_S ([\mathbf{u}]\mathbf{n} + \mathbf{n}[\mathbf{u}])dS, \tag{A5}$$

where $[\mathbf{u}] = \mathbf{u}^+ - \mathbf{u}^-$ is the displacement discontinuity vector of the crack surfaces, and superscripts $+$ and $-$ denote the front and back of the crack surface, respectively. The normal vector $\mathbf{n}$ is a constant for a planer crack, and the average extra strain is

$$\begin{aligned} \Delta\boldsymbol{\epsilon} &= \frac{S}{2V}(\mathbf{bn} + \mathbf{nb}) \\ \Delta\epsilon_{ij} &= \frac{S}{2V}(\langle b_i\rangle n_j + \langle b_j\rangle n_i), \end{aligned} \tag{A6}$$

where $\mathbf{b} = \langle \mathbf{u}^+ - \mathbf{u}^-\rangle$, and $\langle b\rangle$ is the average displacement discontinuity vector. The vector $\mathbf{b}$ can be given by a compliance tensor $\mathbf{B}$, which is a second-order symmetric tensor, and

surface traction applied to the crack surface $\mathbf{t}$ as:

$$\begin{aligned} \mathbf{b} &= \mathbf{B} \cdot \mathbf{t} = \mathbf{B} \cdot \boldsymbol{\sigma} \cdot \mathbf{n} \\ \langle b_i \rangle &= B_{ip} t_p = B_{ip} \sigma_{pq} n_q. \end{aligned} \tag{A7}$$

Therefore, the extra strain is

$$\Delta\epsilon_{ij} = \frac{S}{2V}(B_{ip}\sigma_{pq}n_q n_j + B_{jp}\sigma_{pq}n_q n_i), \tag{A8}$$

and the extra compliace is

$$\Delta S_{ijkl} = \frac{S}{4V}(B_{ik}n_l n_j + B_{il}n_k n_j + B_{jk}n_l n_i + B_{jl}n_k n_i). \tag{A9}$$

When a rock contains N cracks, the extra compliance due to the cracks is given as a sum of each crack contribution:

$$\Delta S_{ijkl} = \frac{1}{4V} \sum_{(m)=1}^{N} \left[B_{ik}n_l n_j + B_{il}n_k n_j + B_{jk}n_l n_i + B_{jl}n_k n_i\right]^{(m)} S^{(m)}, \tag{A10}$$

where m denotes mth crack. Note that if the cracks exhibit directional characteristics, the summed component can be substituted by the integral of the directional distribution function, as demonstrated below.

As $\mathbf{B}$ is a second-order symmetric tensor, it possesses three primary directional components for the elastic compliance of the crack. When uniform stress is imposed in one direction, no displacement ($\mathbf{b}$) transpires in the remaining two directions. Consequently,

$$\mathbf{B} = \begin{pmatrix} B_{nn} & 0 & 0 \\ 0 & B_{ss} & 0 \\ 0 & 0 & B_{tt} \end{pmatrix} = B_{nn}\mathbf{nn} + B_{ss}\mathbf{ss} + B_{tt}\mathbf{tt}.$$

As two orthogonal directions are equivalent on the plane of the crack, $B_{ss} = B_{tt} \equiv B_T$, and ultimately $\mathbf{B}$ is the composite of the component B_N perpendicular to the crack and the horizontal component (shear component) B_T, as follows:

$$\begin{aligned} \mathbf{B} &= B_N\mathbf{nn} + B_T(\mathbf{I} - \mathbf{nn}) \\ B_{ij} &= B_N n_i n_j + B_T(\delta_{ij} - n_i n_j). \end{aligned} \tag{A11}$$

This leads to

$$\begin{aligned} B_{ik}n_l n_j &= B_N n_i n_k n_l n_j + B_T \delta_{ik} n_l n_j - B_T n_i n_k n_l n_j \\ &= B_T \delta_{ik} n_l n_j + (B_N - B_T) n_i n_j n_k n_l. \end{aligned} \tag{A12}$$

The same calculations for the other components yield the extra compliance

$$\begin{aligned} &\Delta S_{ijkl} \\ &= \frac{1}{4V} \sum_{(m)=1}^{N} \left[B_T(\delta_{ik}n_l n_j + \delta_{il}n_k n_j + \delta_{jk}n_l n_i + \delta_{jl}n_k n_i) + 4(B_N - B_T) n_i n_j n_k n_l \right]^{(m)} S^{(m)} \\ &= \frac{1}{V} \sum_{(m)=1}^{N} \left[\frac{1}{4}(\delta_{ik}n_l n_j + \delta_{il}n_k n_j + \delta_{jk}n_l n_i + \delta_{jl}n_k n_i) + \left(\frac{B_N}{B_T} - 1 \right) n_i n_j n_k n_l \right]^{(m)} B_T S^{(m)}. \end{aligned} \tag{A13}$$

In the case of a penny-shaped crack, which has a radius of c, the aperture of w, and the surface of $S = \pi c^2$, B_N and B_T are given as:

$$B_T = \frac{32(1-\nu_0^2)c}{3\pi E_0(2-\nu_0)}, \tag{A14}$$

and

$$\frac{B_N}{B_T} = \left(1 - \frac{\nu_0}{2}\right) \frac{\delta}{1+\delta}, \tag{A15}$$

where E_0 and ν_0 are Young's modulus and Poisson's ratio of the solid phase. The parameter δ is a non-dimensional scalar that characterizes the coupling between the stress and the pore pressure and is given as:

$$\delta = \frac{16(1-\nu_0^2)E_0\zeta}{3\pi K_f}, \tag{A16}$$

where K_f is the fluid bulk modulus, and $\zeta = w/c$ is the crack aspect rario. For a penny-shaped crack,

$$B_T S = \frac{32(1-\nu_0^2)c}{3\pi E_0(2-\nu_0)} \times \pi c^2 = \frac{32(1-\nu_0^2)}{3E_0(2-\nu_0)} c^3. \tag{A17}$$

Substituting Equation A14, the extra compliance is

$$\begin{aligned} &\Delta S_{ijkl} \\ &= \frac{1}{V} \sum_{(m)=1}^{N} \left[\frac{1}{4}(\delta_{ik}n_l n_j + \delta_{il}n_k n_j + \delta_{jk}n_l n_i + \delta_{jl}n_k n_i) + \left(\frac{B_N}{B_T} - 1 \right) n_i n_j n_k n_l \right]^{(m)} B_T S^{(m)} \\ &= \frac{h}{V} \sum_{(m)=1}^{N} \left[\frac{1}{4}(\delta_{ik}n_l n_j + \delta_{il}n_k n_j + \delta_{jk}n_l n_i + \delta_{jl}n_k n_i) + \psi n_i n_j n_k n_l \right]^{(m)} (c^{(m)})^3, \end{aligned} \tag{A18}$$

where

$$h = \frac{32(1-\nu_0^2)}{3E_0(2-\nu_0)} \tag{A19}$$

and

$$\psi = \left(1 - \frac{\nu_0}{2}\right)\frac{\delta}{1+\delta} - 1. \tag{A20}$$

Here, we define a second- and forth-rank tensors α_{ij} and β_{ijkl} as follows:

$$\alpha_{ij} = \frac{1}{V}\sum_{(m)=1}^{N}(c^3 n_i n_j)^{(m)} = \frac{Nc^3}{V}\sum_{N}\frac{n_i n_j}{N} = \frac{Nc^3}{V}\langle n_i n_j\rangle \tag{A21}$$

$$\beta_{ijkl} = \frac{1}{V}\sum_{(m)=1}^{N}(c^3 n_i n_j n_k n_l)^{(m)} = \frac{Nc^3}{V}\sum_{N}\frac{n_i n_j n_k n_l}{N} = \frac{Nc^3}{V}\langle n_i n_j n_k n_l\rangle, \tag{A22}$$

where $\langle n_i n_j\rangle$ is the moment of the normal vectors. Note that

$$\mathrm{tr}(\alpha_{ij}) = \frac{1}{V}\sum_{(m)=1}^{N} c^3 = \frac{Nc^3}{V} = \rho, \tag{A23}$$

where ρ is referred to as crack density parameter. Therefore, the tensors α_{ij} and β_{ijkl} can be understood as the crack density tensors that are characterized by the population of the cracks with normal vectors n_i and n_j as:

$$\alpha_{ij} = \rho\langle n_i n_j\rangle$$
$$\beta_{ijkl} = \rho\langle n_i n_j n_k n_l\rangle$$

Finally, the extra compliance tensor due to the presence of cracks can be expressed as a function of the second- and forth-rank crack density tensors as:

$$\Delta S_{ijkl} = h\left[\frac{1}{4}(\delta_{ik}\alpha_{jl} + \delta_{il}\alpha_{jk} + \delta_{jk}\alpha_{il} + \delta_{jl}\alpha_{ik}) + \psi\beta_{ijkl}\right]. \tag{A24}$$

A.2 Components of effective compliance tensor

One of the prevalent areas of interest in geoscience and geophysics is that of transverse isotropy (TI) medium. In a TI medium, one axis of symmetry (axis 3 in this instance) serves as the axis of symmetry, while the directional distributions are equivalent across the remaining two axes. The elastic compliance tensor of the TI medium **S** is given as the inverse

of stiffness tensor $\mathbf{C}$:

$$\begin{aligned}\mathbf{S}=\mathbf{C}^{-1}&=\begin{pmatrix} S_{1111} & S_{1122} & S_{1133} & 0 & 0 & 0 \\ S_{1122} & S_{1111} & S_{1133} & 0 & 0 & 0 \\ S_{1133} & S_{1133} & S_{3333} & 0 & 0 & 0 \\ 0 & 0 & 0 & S_{2323} & 0 & 0 \\ 0 & 0 & 0 & 0 & S_{2323} & 0 \\ 0 & 0 & 0 & 0 & 0 & S_{1212} \end{pmatrix} \\ &=\begin{pmatrix} \frac{1}{E} & -\frac{\nu}{E} & -\frac{\nu}{E} & 0 & 0 & 0 \\ -\frac{\nu}{E} & \frac{1}{E} & -\frac{\nu}{E} & 0 & 0 & 0 \\ -\frac{\nu}{E} & -\frac{\nu}{E} & \frac{1}{E} & 0 & 0 & 0 \\ 0 & 0 & 0 & \frac{1+\nu}{2E} & 0 & 0 \\ 0 & 0 & 0 & 0 & \frac{1+\nu}{2E} & 0 \\ 0 & 0 & 0 & 0 & 0 & \frac{1+\nu}{2E} \end{pmatrix},\end{aligned} \tag{A25}$$

where E and ν are Young's modulus and Poisson ratio of the TI medium, respectively. For a general transversely isotropic orientation distribution of cracks, $\alpha_{11}=\alpha_{22}$, $\beta_{1111}=\beta_{2222}$, $\beta_{1133}=\beta_{1313}=\beta_{2233}=\beta_{2323}$, and $\beta_{1212}=\beta_{1122}=\beta_{1111}/3$. Therefore, we have each component of the effective elastic compliance tensor of the TI medium via five independent components of the crack density tensor $(\alpha_{11},\alpha_{33},\beta_{1111},\beta_{3333},\beta_{1133})$ as:

$$\begin{aligned} S_{1111}&=\frac{1}{E_0}+h(\alpha_{11}+\psi\beta_{1111}),\\ S_{3333}&=\frac{1}{E_0}+h(\alpha_{33}+\psi\beta_{3333}),\\ S_{1122}&=-\frac{\nu_0}{E_0}+\frac{h}{3}\psi\beta_{1111},\\ S_{1133}&=-\frac{\nu_0}{E_0}+h\psi\beta_{1133},\\ S_{1212}&=\frac{1+\nu_0}{2E_0}+h\left(\frac{\alpha_{11}}{2}+\frac{\psi}{3}\beta_{1111}\right),\\ S_{1313}&=\frac{1+\nu_0}{2E_0}+h\left(\frac{\alpha_{11}+\alpha_{33}}{4}+\psi\beta_{1133}\right). \end{aligned} \tag{A26}$$

In the limit case of a dry medium, $K_f\to 0$, and the parameter $\delta/(1+\delta)\to 1$, which yields

$$\psi=-\frac{\nu_0}{2}. \tag{A27}$$

This means that there is no contribution of the aspect ratio ζ to the effective compliance under dry conditions. Note that, since the Poisson's ratio of the solid phase is typically 0.2–0.3, $\psi\beta_{ijkl}$ under dry conditions is negligibly small in comparison to α_{ij}. Therefore, to reduce the number of unknowns and simplify the calculation when determining the crack density tensor under dry conditions, each component of the compliance tensor can be utilized in the following form, disregarding the β_{ijkl} terms (Sayers & Kachanov, 1995):

$$\begin{aligned} S_{1111} &= \frac{1}{E_0} + h\alpha_{11}, \\ S_{3333} &= \frac{1}{E_0} + h\alpha_{33}, \\ S_{1122} &= -\frac{\nu_0}{E_0}, \\ S_{1133} &= -\frac{\nu_0}{E_0}, \\ S_{1212} &= \frac{1+\nu_0}{2E_0} + \frac{h}{2}\alpha_{11}, \\ S_{1313} &= \frac{1+\nu_0}{2E_0} + \frac{h}{4}(\alpha_{11}+\alpha_{33}). \end{aligned} \tag{A28}$$

The compliance tensors are often abbreviated as the Voigt notation (Mavko et al., 2020). With the Voigt notation, four subscripts of the compliance tensor (S_{ijkl}) are reduced to two (S_{pq}) using the convention summarized in Table A1 and the relation $S_{pq} = \mathbf{N}S_{ijkl}$, where

$$N = \begin{cases} 1 & \text{for} \quad p \text{ and } q = 1,2,3 \\ 2 & \text{for} \quad p \text{ or } q = 4,5,6 \\ 4 & \text{for} \quad p \text{ and } q = 4,5,6 \end{cases}. \tag{A29}$$

Table A1 Voigt notation

ij or kl	11	22	33	23 or 32	31 or 13	12 or 21
p or q	1	2	3	4	5	6

In the case of TI medium, care must be taken that multiplying the factors of 4 is needed for S_{1212} and S_{1313} as:

$$\begin{aligned} S_{44} = 4S_{1313} &= \frac{2(1+\nu_0)}{E_0} + 2h\alpha_{11}, \\ S_{66} = 4S_{1212} &= \frac{2(1+\nu_0)}{E_0} + h(\alpha_{11}+\alpha_{33}), \end{aligned} \tag{A30}$$

where $2(1+\nu_0)/E_0 = 1/G_0$.

A.3 Transformation to scalar crack density

Equation A26 may be inverted to obtain the α_{ij} and β_{ijkl} given the S_{ij} obtained from elastic wave velocity measurements (Sayers & Kachanov, 1995). As described above, as the number of unknowns under dry conditions is two (α_{11} and α_{33}), only two components of elastic wave velocity are required to invert the crack densities. Meanwhile, the number of unknowns to be determined increases by three ($\beta_{1111}, \beta_{3333}, \beta_{1133}$) under wet conditions. Therefore, a full inversion of the crack tensor under wet conditions requires more than four components of velocity measurements, including on-axis velocity, whereas the number of electrical feedthroughs to measure the velocities is often limited.

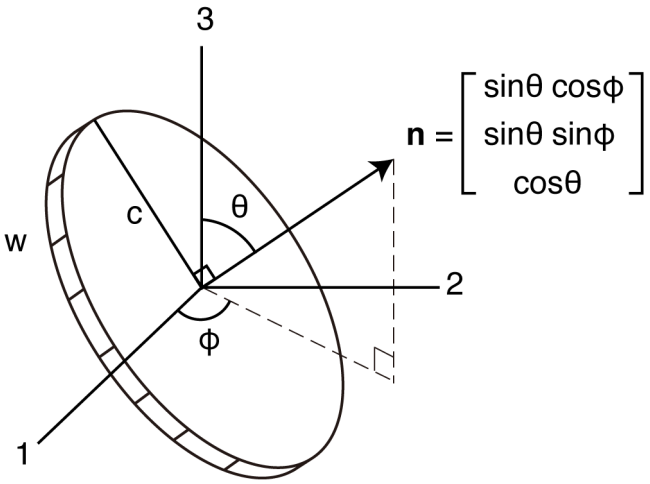

Figure A2 Penny-shape crack with a radius of c and width w. Symmetry axis 3 is imposed by transverse isotropy, where θ and ϕ are the polar angles and the azimuthal angle, respectively.

Nevertheless, by assuming the orientation distribution of cracks (i.e., anisotropy), the number of unknowns (components that need to be measured) can be reduced by utilizing the symmetry of the TI medium and the anisotropy of cracks. If the TI medium is characterized by a high concentration of cracks, the summation component in Equation A21 can be replaced by integrals of the crack orientation distributions (Brantut, 2015; Hudson, 1990), and the second order and the fourth order moments of the crack orientation distribution are given as:

$$\begin{aligned} \langle n_i n_j \rangle &= \frac{1}{2\pi} \int_0^{2\pi} \int_0^{\pi/2} f(\theta,\phi) n_i n_j \sin\theta d\theta d\phi \\ \langle n_i n_j n_k n_l \rangle &= \frac{1}{2\pi} \int_0^{2\pi} \int_0^{\pi/2} f(\theta,\phi) n_i n_j n_k n_l \sin\theta d\theta d\phi, \end{aligned} \tag{A31}$$

where $f(\theta, \phi)$ is the number density of cracks with normal unit vectors lying in the solid angle $(\theta, \theta + d\theta)$; $(\phi, \phi + d\phi)$, θ is the polar angle, and ϕ is the azimuthal angle. The normal vector $\mathbf{n}$ is written as

$$\mathbf{n} = \begin{pmatrix} \sin\theta\cos\phi \\ \sin\theta\sin\phi \\ \cos\theta \end{pmatrix}. \tag{A32}$$

Here, we consider three different distributions of crack orientations in terms of transverse isotropy: horizontal cracks, vertical cracks, and isotropic cracks. These cases represent limiting cases of expected real situations (Guéguen & Sarout, 2011). The first case is that of identical cracks aligned in the horizontal plane x_1x_2, perpendicular to the symmetry axis x_3 (Figure A3a). The normals are oriented along $\theta = 0$, and the azimuthal angles ϕ are random. The second case is that of cracks oriented in the symmetry axis x_3, in which the normals are oriented along $\theta = 90$ž with the randomly oriented azimuthal angles (Figure A3b). The third case is that of randomly oriented cracks (Figure A3c). The density functions for each case are given as:

$$f(\theta) = \begin{cases} \frac{N_h}{V\sin\theta} & \text{(for horizontal cracks)} \\ \frac{N_v}{V\sin\theta} & \text{(for vertical cracks)} \\ \frac{N_r}{V} & \text{(for randomly oriented cracks),} \end{cases} \tag{A33}$$

where N_h, N_v, and N_r are the number of horizontal, vertical, and randomly oriented cracks within the volume V, respectively. Analogous to Equation A23, three independent scalr crack densities, horizontal crack density ρ_h, vertical crack density ρ_v, and randomly oriented crack density ρ, can be defined as:

$$\begin{aligned} \rho_h &= \frac{N_h c_h^3}{V}, \\ \rho_v &= \frac{N_v c_v^3}{V}, \\ \rho_r &= \frac{N_r c_r^3}{V}. \end{aligned} \tag{A34}$$

A.3.1 Horizontal cracks

As shown above, the normals of horizontal cracks are oriented along $\theta = 0$, and the azimuthal angles ϕ are randomly distributed from 0^o to 360^o. In this case, $n_1 = \sin\theta\cos\phi = 0$, $n_2 = \sin\theta\sin\phi = 0$, and $n_3 = \cos\theta = 1$, so that the crack density tensors α_{ij} and β_{ijkl}

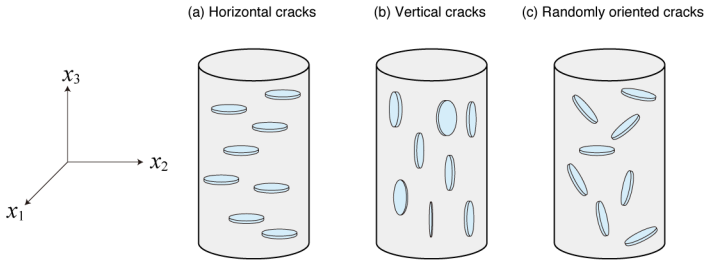

Figure A3 Three limiting cases of crack orientation distributions for the transversely isotropy. (a) Maximum anisotropy: cracks with normals oriented along the symmetry axis x_3. (b) Intermediate anisotropy: cracks with normals oriented orthogonal to x_3. (c) No anisotropy: cracks with randomly oriented normals.

become

$$\begin{aligned}
\alpha_{11} &= \rho_h \langle n_1 n_1 \rangle = 0 \\
\alpha_{33} &= \rho_h \langle n_3 n_3 \rangle = \rho_h \frac{1}{2\pi} \int_0^{2\pi} d\phi = \rho_h \\
\beta_{1111} &= \rho_h \langle n_1 n_1 n_1 n_1 \rangle = 0 \\
\beta_{3333} &= \rho_h \langle n_3 n_3 n_3 n_3 \rangle = \rho_h \frac{1}{2\pi} \int_0^{2\pi} d\phi = \rho_h .
\end{aligned} \tag{A35}$$

with all other components being zero. The resulting effective compliance tensor in the Voigt notation is given as:

$$\begin{aligned}
S_{11} &= \frac{1}{E_0}, \\
S_{33} &= \frac{1}{E_0} + h\psi\rho_h, \\
S_{12} &= -\frac{\nu_0}{E_0}, \\
S_{13} &= -\frac{\nu_0}{E_0}, \\
S_{44} &= \frac{2(1+\nu_0)}{E_0} + h\psi\rho_h, \\
S_{66} &= \frac{2(1+\nu_0)}{E_0}.
\end{aligned} \tag{A36}$$

Recalling $\mathbf{S} = \mathbf{C}^{-1}$, the effective stiffness tensor C_{ij} that can be used to directly compute

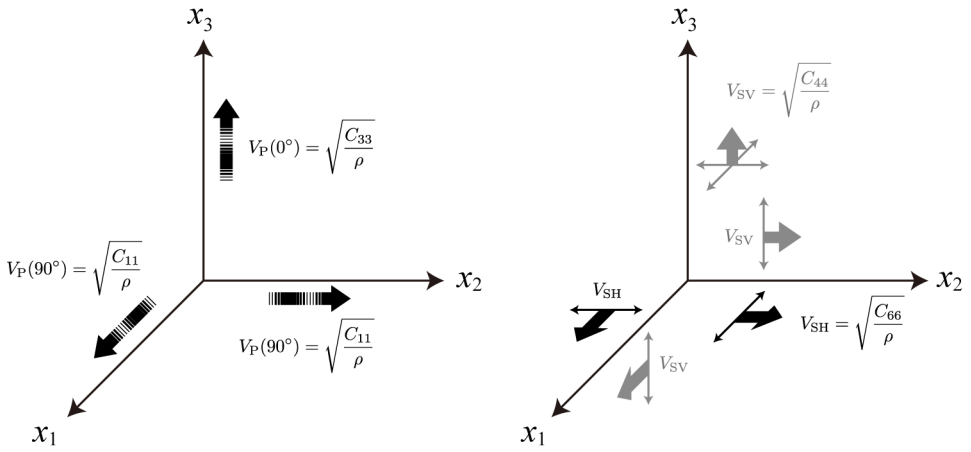

Figure A4 Elastic wave velocities in a transversely isotropic medium, and the corresponding stiffness components. S-waves are polarized in the planes perpendicular (SH-wave) and parallel (SV-wave) to the symmetry axis x_3.

elastic wave velocities (Figure A4) is given by

$$
\begin{aligned}
C_{11} &= \left(E_0 + \frac{\nu_0^2}{\frac{1-2\nu_0}{E_0} + h\rho_h(1+\psi_h)} \right) \frac{1}{1-\nu_0^2} = \frac{E_0}{1-\nu_0^2} + \frac{1}{\frac{1-\nu_0^2}{\nu_0^2}\left(\frac{1-2\nu_0}{E_0} + h\rho_h(1+\psi_h)\right)}, \\
C_{33} &= \frac{1}{\frac{(1-2\nu_0)(1+\nu_0)}{E_0(1-\nu_0)} + h\rho_h(1+\psi_h)} = \frac{1}{\frac{1}{K_0+\frac{4}{3}G_0} + h\rho_h(1+\psi_h)}, \\
C_{44} &= \frac{1}{\frac{2(1+\nu_0)}{E_0} + h\rho_h} = \frac{1}{\frac{1}{G_0} + h\rho_h}, \\
C_{66} &= \frac{E_0}{2(1+\nu_0)} = G_0, \\
C_{13} &= \frac{1}{\frac{(1+\nu_0)(1-2\nu_0)}{E_0\nu_0} + \frac{1-\nu_0}{\nu_0} h\rho_h(1+\psi_h)}, \\
C_{12} &= C_{11} - 2C_{66},
\end{aligned}
\tag{A37}
$$

where

$$
\psi_h = \left(1 - \frac{\nu_0}{2}\right) \frac{\delta_h}{1+\delta_h} - 1, \tag{A38}
$$

and

$$
\delta_h = \frac{16(1-\nu_0^2)E_0\zeta_h}{3\pi K_f}. \tag{A39}
$$

Figure A5 shows the elastic wave velocities calculated as a function of horizontal crack density using Equation A37. The crack-free velocities are taken to be $V_P^0 = 7.0$ km/s and $V_S^0 = 3.8$ km/s. P-wave velocity propagating parallel to the symmetry axis (axial direction, $V_P(90°)$)

markedly decreases with increasing crack density, whereas that perpendicular to the axis (radial direction, $V_{\mathrm{P}}(0°)$) does not decrease significantly. Similar trends are observed for polarized S-wave velocities propagating in the radial direction, in which SH-wave velocity $V_{\mathrm{SH}}(90°)$ is independent of crack density whereas SV-wave velocity $V_{\mathrm{SH}}(90°)$ decreases with crack density. In contrast, SH- and SV-wave velocities in the axial direction are comparable to each other, due to the symmetry of transverse isotropy. The resulting $V_{\mathrm{P}}/V_{\mathrm{S}}$ decreases differently from SH- and SV-wave velocities in the radial direction, whereas those in the axial direction are comparable. Under water-saturated conditions, similar trends to those under dry conditions are also observed, but the amount of decrease is limited. It should be noted that the V_{P} and V_{S} in the radial direction do not depend on the aspect ratio, whereas V_{P} in the axial direction slightly depends on the aspect ratio.

A.3.2 Vertical crack

Vertical cracks have the normals oriented along $\theta = 90$ž, and the azimuthal angles ϕ are randomly distributed from 0º to 360º as well as the horizontal cracks. In this case, $n_1 = \cos\phi$, $n_2 = \sin\phi$, and $n_3 = 0$, so that the crack density tensors α_{ij} and β_{ijkl} become

$$\begin{aligned}
\alpha_{11} &= \frac{\rho_v}{2\pi}\int_0^{2\pi}(\cos^2\phi)d\phi = \frac{\rho_v}{2} \\
\alpha_{33} &= \rho_v\langle n_3 n_3\rangle = 0 \\
\beta_{1111} &= \langle n_1 n_1 n_1 n_1\rangle = \frac{\rho_v}{2\pi}\int_0^{2\pi}(\cos^4\phi)d\phi = \frac{3}{8}\rho_v \\
\beta_{1212} &= \langle n_1 n_1 n_2 n_2\rangle = \frac{\rho_v}{2\pi}\int_0^{2\pi}(\cos^2\phi\sin\phi^2)d\phi = \frac{1}{8}\rho_v \\
\beta_{3333} &= \rho_v\langle n_3 n_3 n_3 n_3\rangle = 0.
\end{aligned} \tag{A40}$$

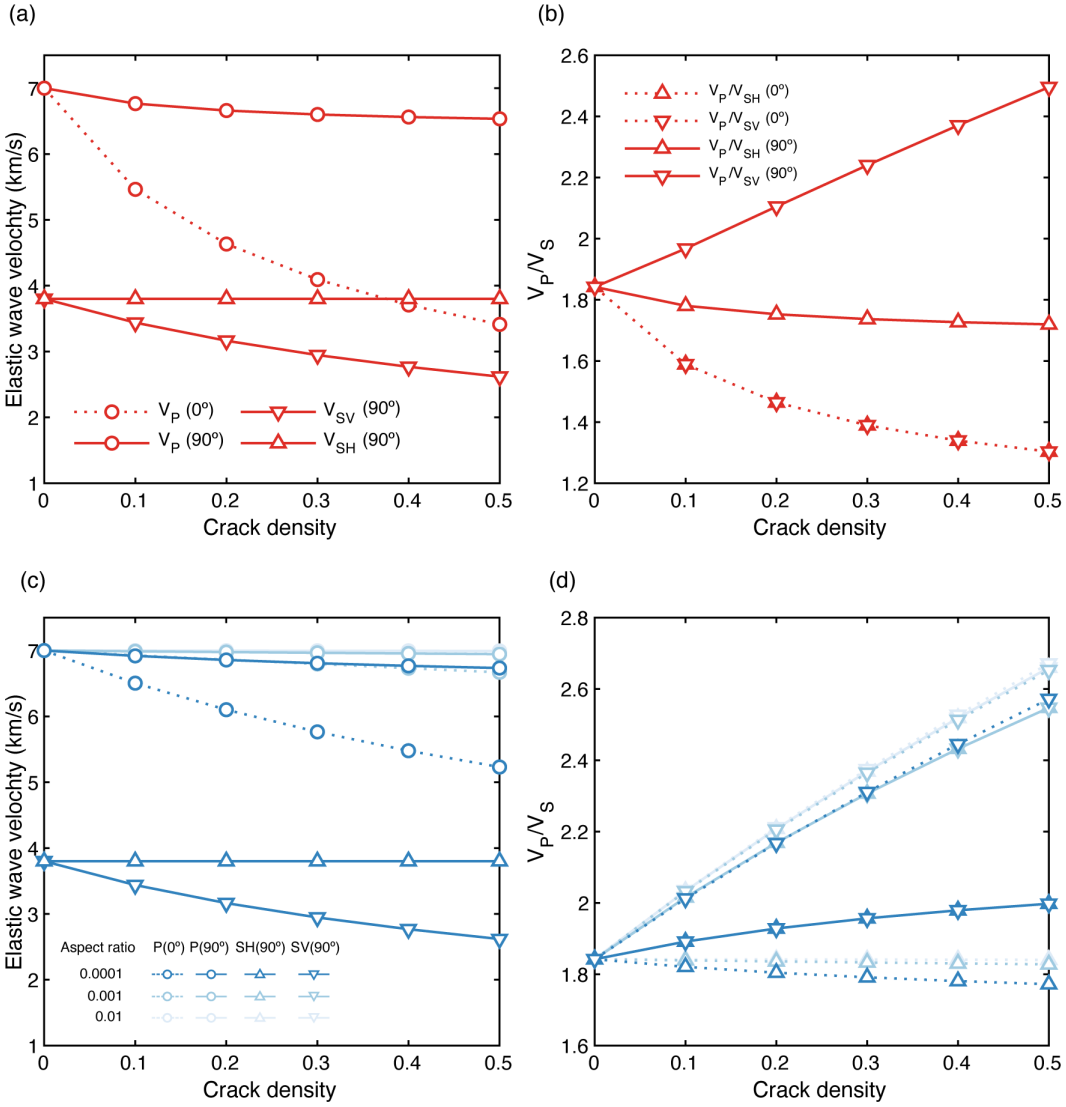

Figure A5 Elastic wave velocity as a function of horizontal crack density under dry (a,b) and water-saturated (unrelaxed) conditions (c,d). The contribution of the fourth-rank crack density tensor (β_{ijkl}) is included for both conditions. Numbers in parentheses denote the propagation angle against the symmetry angle. For water-saturated conditions, typical aspect ratios of 0.01, 0.001, and 0.0001 are assumed. The calculation was performed assuming no crack interactions.

with all other components being zero. The resulting effective compliance tensor in the Voigt notation is given as:

$$\begin{aligned}
S_{11} &= \frac{1}{E_0} + \left(\frac{1}{2} + \frac{3}{8}\psi\right) h\rho_v, \\
S_{33} &= \frac{1}{E_0}, \\
S_{12} &= -\frac{\nu_0}{E_0} + \frac{1}{8} h\psi\rho_v, \\
S_{13} &= -\frac{\nu_0}{E_0}, \\
S_{44} &= \frac{2(1+\nu_0)}{E_0} + \frac{1}{2} h\rho_v, \\
S_{66} &= \frac{2(1+\nu_0)}{E_0} + \left(1 + \frac{1}{2}\psi\right) h\rho_v.
\end{aligned} \tag{A41}$$

The effective stiffness tensor C_{ij} are

$$\begin{aligned}
C_{11} &= \frac{1}{\frac{2(1+\nu_0)}{E_0} + h\rho_v\left(1 + \frac{1}{2}\psi_v\right)} + \frac{1}{\frac{2(1-2\nu_0)(1+\nu_0)}{E_0} + h\rho_v(1+\psi_v)}, \\
C_{33} &= E_0 + \frac{\nu_0^2}{\frac{(1-2\nu_0)(1+\nu_0)}{2E_0} + \frac{h}{4}\rho_v(1+\psi_v)}, \\
C_{44} &= \frac{1}{\frac{2(1+\nu_0)}{E_0} + \frac{h}{2}\rho_v}, \\
C_{66} &= \frac{1}{\frac{2(1+\nu_0)}{E_0} + h\rho_v\left(1 + \frac{1}{2}\psi_v\right)}, \\
C_{13} &= \frac{\nu_0}{\frac{(1-2\nu_0)(1+\nu_0)}{E_0} + \frac{h}{2}\rho_v(1+\psi_v)}, \\
C_{12} &= C_{11} - 2C_{66},
\end{aligned} \tag{A42}$$

where

$$\psi_v = \left(1 - \frac{\nu_0}{2}\right)\frac{\delta_v}{1+\delta_v} - 1, \tag{A43}$$

and

$$\delta_v = \frac{16(1-\nu_0^2)E_0\zeta_v}{3\pi K_f}. \tag{A44}$$

Figure A6 shows the elastic wave velocities calculated as a function of vertical crack density using Equation A42, with the crack-free velocities of $V_{\mathrm{P}}^0 = 7.0$ km/s and $V_{\mathrm{S}}^0 = 3.8$ km/s. Although trends similar to those for horizontal cracks are observed, the direction in which the velocity reduction is remarkable is opposite to that for horizontal cracks. Radial V_{P} and V_{SH} markedly decrease with vertical crack density, whereas the decreases in axial V_{P} and V_{SV} are relatively small. Thus, the trends of $V_{\mathrm{P}}/V_{\mathrm{S}}$ are also opposite between these two

cases Under water-saturated conditions, the effect of aspect ratio on the radial V_{P} becomes significant, resulting in marked increases in $V_{\mathrm{P}}/V_{\mathrm{S}}$.

A.3.3 Randomly oriented crack

In the case that the crack normals are randomly oriented, crack normal components are characterized by the following moments of their orientational distribution:

$$\begin{aligned}
\alpha_{11} &= \rho_r\langle n_1 n_1\rangle = \rho_r \frac{1}{2\pi}\int_0^{2\pi}\int_0^{\pi/2} \sin\theta^2\cos\phi^2\sin\theta d\theta d\phi = \frac{1}{3}\rho_r,\\
\alpha_{33} &= \rho_r\langle n_3 n_3\rangle = \rho_r \frac{1}{2\pi}\int_0^{2\pi}\int_0^{\pi/2} \cos\theta^2\sin\theta d\theta d\phi = \frac{1}{3}\rho_r,\\
\beta_{1111} &= \rho_r\langle n_1 n_1 n_1 n_1\rangle = \rho_r \frac{1}{2\pi}\int_0^{2\pi}\int_0^{\pi/2} \sin\theta^4\cos\phi^4\sin\theta d\theta d\phi = \frac{1}{5}\rho_r,\\
\beta_{3333} &= \rho_r\langle n_3 n_3 n_3 n_3\rangle = \rho_r \frac{1}{2\pi}\int_0^{2\pi}\int_0^{\pi/2} \cos\theta^4\sin\theta d\theta d\phi = \frac{1}{5}\rho_r,\\
\beta_{1133} &= \rho_r\langle n_1 n_1 n_3 n_3\rangle = \rho_r \frac{1}{2\pi}\int_0^{2\pi}\int_0^{\pi/2} \sin\theta^2\cos\phi^2\cos\theta^2\sin\theta d\theta d\phi = \frac{1}{15}\rho_r,
\end{aligned} \tag{A45}$$

These indicate that there is no anisotropy in the case of randomly oriented cracks, and the elastic constants to compute the velocities are:

$$\begin{aligned}
\frac{K_0}{K} &= 1 + \frac{h'\rho}{1-2\nu_0}(1+\psi),\\
\frac{G_0}{G} &= 1 + \frac{h'\rho}{1+\nu_0}\left(1+\frac{2}{5}\psi\right),
\end{aligned} \tag{A46}$$

where

$$h' = \frac{16(1-\nu_0^2)}{9(1-\nu_0/2)} \tag{A47}$$

and

$$\psi = \left(1-\frac{\nu_0}{2}\right)\frac{\delta}{1+\delta} - 1. \tag{A48}$$

These equations are comparable to those for scalar crack density presented by Kachanov (1994).

Figure A7 shows the elastic wave velocities calculated as a function of randomly oriented crack density using Equation A46, with the crack-free velocities of $V_{\mathrm{P}}^0 = 7.0$ km/s and $V_{\mathrm{S}}^0 = 3.8$ km/s. These results are comparable to those calculated using equations by Kachanov (1994) as expected.

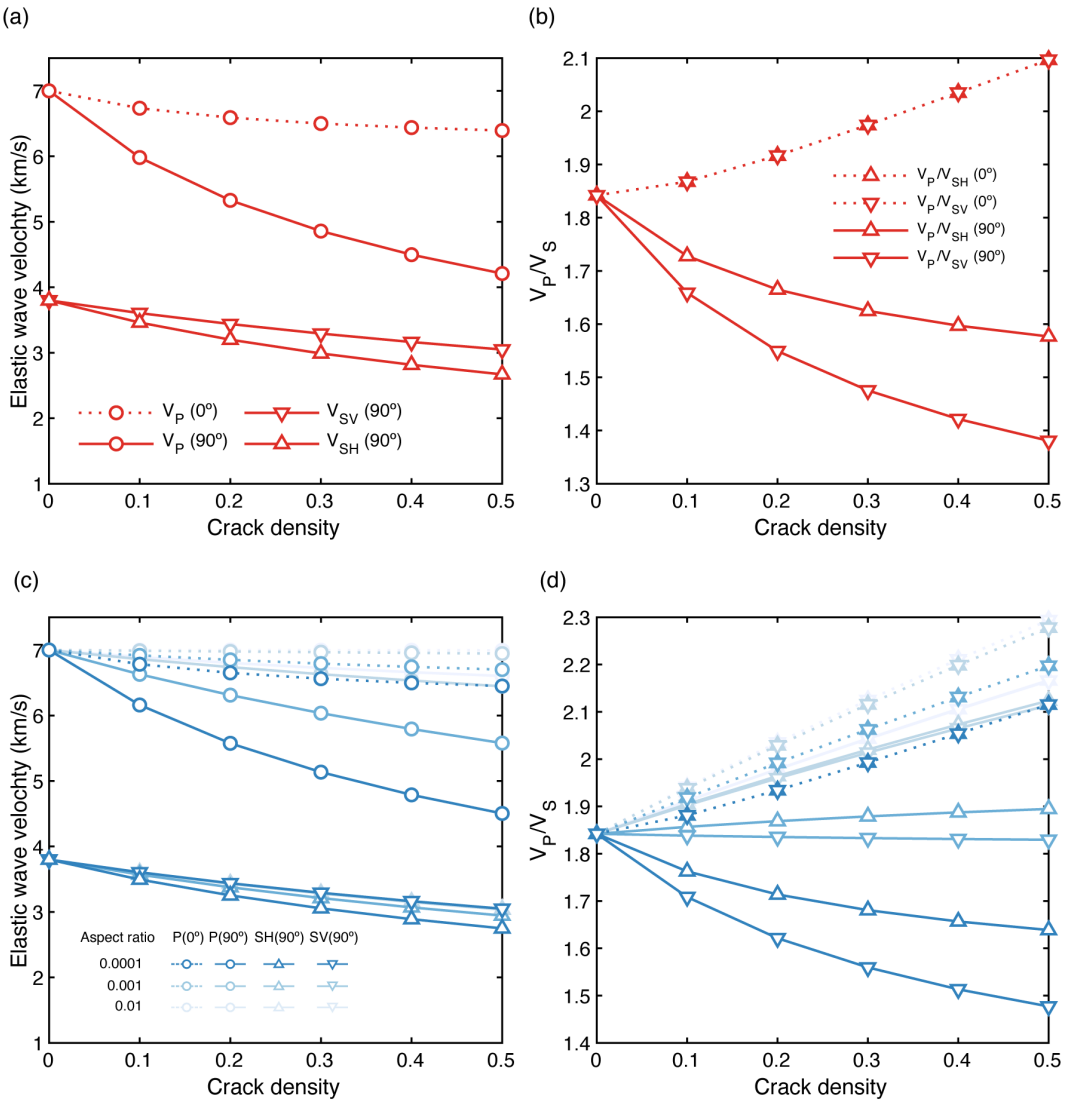

Figure A6 Elastic wave velocity as a function of vertical crack density under dry (a,b) and water-saturated (unrelaxed) conditions (c,d). The contribution of the fourth-rank crack density tensor (β_{ijkl}) is included for both conditions. Numbers in parentheses denote the propagation angle against the symmetry angle. For water-saturated conditions, typical aspect ratios of 0.01, 0.001, and 0.0001 are assumed. The calculation was performed assuming no crack interactions.

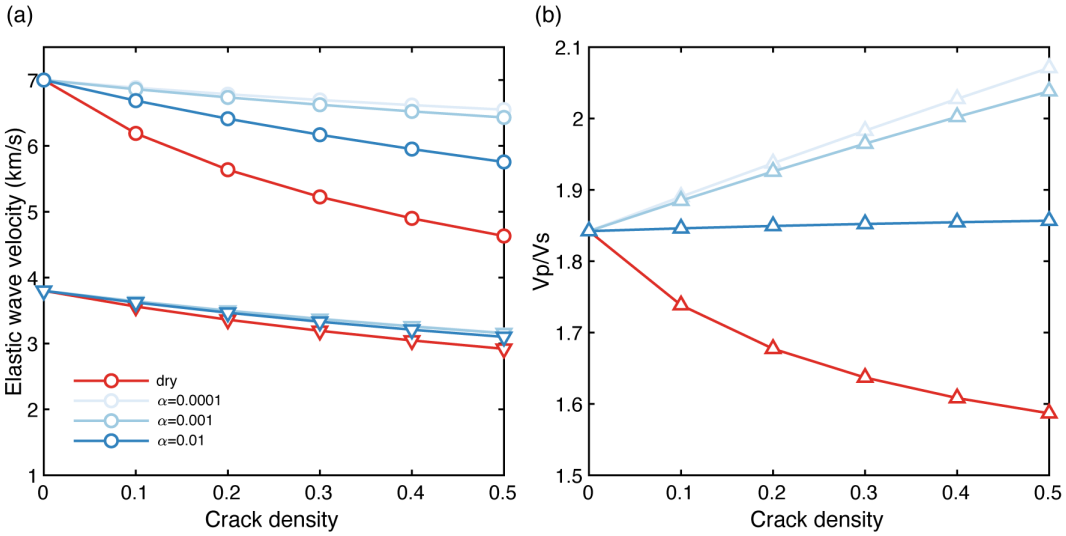

Figure A7 Elastic wave velocity as a function of randomly oriented crack density under dry (a) and water-saturated (unrelaxed) conditions (b). For water-saturated conditions, typical aspect ratios of 0.01, 0.001, and 0.0001 are assumed. The calculation was performed assuming no crack interactions.

References

Adamus, F. P. (2021). Effective elasticity of a medium with many parallel fractures. *Geophysical Journal International*, *227*(3), 1818–1831. https://doi.org/10.1093/gji/ggab306

Akamatsu, Y., Katayama, I., & Tonegawa, T. (2021). Changes in elastic wave velocity during brittle deformation of gabbro and peridotite: Implications for oceanic moho reflectivity. *Earth and Planetary Science Letters*, *568*, 117036. https://doi.org/10.1016/j.epsl.2021.117036

Al-Sit, W., Al-Nuaimy, W., Marelli, M., & Al-Ataby, A. (2015). Visual texture for automated characterisation of geological features in borehole televiewer imagery. *Journal of Applied Geophysics*, *119*, 139–146. https://doi.org/10.1016/j.jappgeo.2015.05.015

Archie, G. E. (1942). The electrical resistivity log as an aid in determining some reservoir characteristics. *Transactions of the AIME*, *146*(01), 54–62.

Asami, K. (2002). Characterization of heterogeneous systems by dielectric spectroscopy. *Progress in Polymer Science*, *27*(8), 1617–1659. https://doi.org/10.1016/S0079-6700(02)00015-1

Assous, S., Elkington, P., Clark, S., & Whetton, J. (2014). Automated detection of planar geologic features in borehole images. *Geophysics*, *79*(1), D11–D19. https://doi.org/10.1190/geo2013-0189.1

Audet, P., & Bürgmann, R. (2014). Possible control of subduction zone slow-earthquake periodicity by silica enrichment. *Nature*, *510*(7505), 389–392. https://doi.org/10.1038/nature13391

Audet, P., Bostock, M. G., Christensen, N. I., & Peacock, S. M. (2009). Seismic evidence for overpressured subducted oceanic crust and megathrust fault sealing. *Nature*, *457*(7225), 76–78. https://doi.org/10.1038/nature07650

Bailly, C., Fortin, J., Adelinet, M., & Hamon, Y. (2019). Upscaling of elastic properties in carbonates: A modeling approach based on a multiscale geophysical data set. *Journal*

of Geophysical Research, [Solid Earth], *124*(12), 13021–13038. https://doi.org/10.1029/2019jb018391

Baker, D. R., Mancini, L., Polacci, M., Higgins, Gualda, G. A. R., Hill, R. J., & Rivers, M. L. (2012). An introduction to the application of x-ray microtomography to the three-dimensional study of igneous rocks. *Lithos*, *148*, 262–276. https://doi.org/10.1016/j.lithos.2012.06.008

Becker, K., & Davis, E. E. (2003). New evidence for age variation and scale effects of permeabilities of young oceanic crust from borehole thermal and pressure measurements. *Earth and Planetary Science Letters*, *210*(3), 499–508. https://doi.org/10.1016/S0012-821X(03)00160-2

Becker, K., & Fisher, A. T. (2000). Permeability of upper oceanic basement on the eastern flank of the juan de fuca ridge determined with drill-string packer experiments. *Journal of Geophysical Research*, *105*, 897–912.

Becker, K., Von Herzen, R. P., Francis, T. J. G., Anderson, R. N., Honnorez, J., Adamson, A. C., et al. (1982). In situ electrical resistivity and bulk porosity of the oceanic crust costa rica rift. *Nature*, *300*(5893), 594–598. https://doi.org/10.1038/300594a0

Benson, P., Schubnel, A., Vinciguerra, S., Trovato, C., Meredith, P., & Young, R. P. (2006). Modeling the permeability evolution of microcracked rocks from elastic wave velocity inversion at elevated isostatic pressure. *Journal of Geophysical Research*, *111*(B4). https://doi.org/10.1029/2005jb003710

Birch, F. (1961). The velocity of compressional waves in rocks to 10 kilobars: 2. *Journal of Geophysical Research*, *66*(7), 2199–2224. https://doi.org/10.1029/jz066i007p02199

Bosch, D., Jamais, M., Boudier, F., Nicolas, A., Dautria, J.-M., & Agrinier, P. (2004). Deep and high-temperature hydrothermal circulation in the oman Ophiolite—Petrological and isotopic evidence. *Journal of Petrology*, *45*(6), 1181–1208. https://doi.org/10.1093/petrology/egh010

Brantut, N. (2015). Time-dependent recovery of microcrack damage and seismic wave speeds in deformed limestone. *Journal of Geophysical Research, [Solid Earth]*. https://doi.org/10.1002/2015JB012324

Brett-Adams, A. C., Diamond, L. W., Petrini, C., & Madonna, C. (2021). Influence of in-situ temperatures and pressures on the permeability of hydrothermally altered basalts in the oceanic crust. *Tectonophysics*, 228994. https://doi.org/10.1016/j.tecto.2021.228994

Brown, J. M., & Abramson, E. H. (2016). Elasticity of calcium and calcium-sodium amphiboles. *Physics of the Earth and Planetary Interiors*, *261*, 161–171. https://doi.org/

10.1016/j.pepi.2016.10.010

Brown, R. J. S., & Korringa, J. (1975). On the dependence of the elastic properties of a porous rock on the compressibility of the pore fluid. *Geophysics*, *40*(4), 608–616. https://doi.org/10.1190/1.1440551

Cai, J., Wei, W., Hu, X., & Wood, D. A. (2017). Electrical conductivity models in saturated porous media: A review. *Earth-Science Reviews*, *171*, 419–433. https://doi.org/10.1016/j.earscirev.2017.06.013

Carcione, J. M., Ursin, B., & Nordskag, J. I. (2007). Cross-property relations between electrical conductivity and the seismic velocity of rocks. *Geophysics*, *72*(5), E193–E204. https://doi.org/10.1190/1.2762224

Carlson, R. L. (2010). How crack porosity and shape control seismic velocities in the upper oceanic crust: Modeling downhole logs from holes 504B and 1256D. *Geochemistry, Geophysics, Geosystems*, *11*(4). https://doi.org/10.1029/2009gc002955

Carlson, R. L., & Miller, D. J. (2004). Influence of pressure and mineralogy on seismic velocities in oceanic gabbros: Implications for the composition and state of the lower oceanic crust. *Journal of Geophysical Research*, *109*(B9). https://doi.org/10.1029/2003jb002699

Carmichael, R. S. (2017). *Practical handbook of physical properties of rocks and minerals (1988)*. CRC Press.

Changchun, Z., & Ge, S. (2002). A hough transform-based method for fast detection of fixed period sinusoidal curves in images. In *6th international conference on signal processing, 2002.* (Vol. 1, pp. 909–912 vol.1). ieeexplore.ieee.org. https://doi.org/10.1109/ICOSP.2002.1181204

Chesley, C., Key, K., Constable, S., Behrens, J., & MacGregor, L. (2019). Crustal cracks and frozen flow in oceanic lithosphere inferred from electrical anisotropy. *Geochemistry, Geophysics, Geosystems*, *20*(12), 5979–5999. https://doi.org/10.1029/2019gc008628

Chesley, C., Naif, S., Key, K., & Bassett, D. (2021). Fluid-rich subducting topography generates anomalous forearc porosity. *Nature*, *595*(7866), 255–260. https://doi.org/10.1038/s41586-021-03619-8

Christensen, N. I. (1984). Pore pressure and oceanic crustal seismic structure. *Geophysical Journal International*, *79*(2), 411–423. https://doi.org/10.1111/j.1365-246X.1984.tb02232.x

Christensen, N. I., & Ramananantoandro, R. (1988). Permeability of the oceanic crust based on experimental studies of basalt permeability at elevated pressures. *Tectonophysics*,

149(1), 181–186. https://doi.org/10.1016/0040-1951(88)90126-6

Cilli, P. A., & Chapman, M. (2021). Linking elastic and electrical properties of rocks using cross-property DEM. *Geophysical Journal International*, *225*(3), 1812–1823. https://doi.org/10.1093/gji/ggab046

Coogan, L. A., Howard, K. A., Gillis, K. M., Bickle, M. J., Chapman, H., Boyce, A. J., et al. (2006). Chemical and thermal constraints on focussed fluid flow in the lower oceanic crust. *American Journal of Science*, *306*(6), 389–427. https://doi.org/10.2475/06.2006.01

Costanza-Robinson, M. S., Estabrook, B. D., & Fouhey, D. F. (2011). Representative elementary volume estimation for porosity, moisture saturation, and air-water interfacial areas in unsaturated porous media: Data quality implications. *Water Resources Research*, *47*(7). https://doi.org/10.1029/2010wr009655

Detrick, R., Collins, J., Stephen, R., & Swift, S. (1994). In situ evidence for the nature of the seismic layer 2/3 boundary in oceanic crust. *Nature*, *370*(6487), 288–290. https://doi.org/10.1038/370288a0

Eberhart-Phillips, D., Bannister, S., & Reyners, M. (2017). Deciphering the 3-D distribution of fluid along the shallow hikurangi subduction zone using P- and s-wave attenuation. *Geophysical Journal International*, *211*(2), 1032–1045. https://doi.org/10.1093/gji/ggx348

Einaudi, F., Pezard, P. A., Cochemé, J.-J., Coulon, C., Laverne, C., & Godard, M. (2000). Petrography, geochemistry and physical properties of a continuous extrusive section from the sarami massif, semail ophiolite. *Marine Geophysical Researches*, *21*(3/4), 387–408. https://doi.org/10.1023/a:1026752415989

Einaudi, F., Pezard, P. A., Ildefonse, B., & Glover, P. (2005). Electrical properties of slow-spreading ridge gabbros from ODP hole 1105A, SW indian ridge. *Geological Society, London, Special Publications*, *240*(1), 179–193. https://doi.org/10.1144/GSL.SP.2005.240.01.14

Elderfield, H., & Schultz, A. (1996). Mid-Ocean ridge hydrothermal fluxes and the chemical composition of the ocean. *Annual Review of Earth and Planetary Sciences*, *24*(1), 191–224. https://doi.org/10.1146/annurev.earth.24.1.191

Evans, R. L. (1994). Constraints on the Large-Scale porosity and permeability structure of young oceanic crust from velocity and resistivity data. *Geophysical Journal International*, *119*(3), 869–879. https://doi.org/10.1111/j.1365-246X.1994.tb04023.x

Faccenda, M. (2014). Water in the slab: A trilogy. *Tectonophysics*, *614*, 1–30. https://doi.org/10.1016/j.tecto.2013.12.020

Fisher, A. T. (1998). Permeability within basaltic oceanic crust. *Reviews of Geophysics*,

36(2), 143–182. https://doi.org/10.1029/97rg02916

Fisher, A. T., & Becker, K. (2000). Channelized fluid flow in oceanic crust reconciles heat-flow and permeability data. *Nature*, *403*(6765), 71–74. https://doi.org/10.1038/47463

Fortin, J., & Guéguen, Y. (2021). Porous and cracked rocks elasticity: Macroscopic poroelasticity and effective media theory. *Mathematics and Mechanics of Solids: MMS*, *26*(8), 1158–1172. https://doi.org/10.1177/10812865211022034

Fortin, J., Guéguen, Y., & Schubnel, A. (2007). Effects of pore collapse and grain crushing on ultrasonic velocities and Vp/Vs. *Journal of Geophysical Research*, *112*(B8). https://doi.org/10.1029/2005jb004005

Fortin, J., Stanchits, S., Vinciguerra, S., & Guéguen, Y. (2011). Influence of thermal and mechanical cracks on permeability and elastic wave velocities in a basalt from mt. Etna volcano subjected to elevated pressure. *Tectonophysics*, *503*(1), 60–74. https://doi.org/10.1016/j.tecto.2010.09.028

Fujie, G., Kodaira, S., Yamashita, M., Sato, T., Takahashi, T., & Takahashi, N. (2013). Systematic changes in the incoming plate structure at the kuril trench. *Geophysical Research Letters*, *40*(1), 88–93.

Fujie, G., Kodaira, S., Kaiho, Y., Yamamoto, Y., Takahashi, T., Miura, S., & Yamada, T. (2018). Controlling factor of incoming plate hydration at the north-western pacific margin. *Nature Communications*, *9*(1), 3844. https://doi.org/10.1038/s41467-018-06320-z

Furnes, H., Muehlenbachs, K., Torsvik, T., Thorseth, I. H., & Tumyr, O. (2001). Microbial fractionation of carbon isotopes in altered basaltic glass from the atlantic ocean, lau basin and costa rica rift. *Chemical Geology*, *173*(4), 313–330. https://doi.org/10.1016/S0009-2541(00)00285-0

Gassmann, F. (1951). Elasticity of porous media. *Vierteljahrsschrder Naturforschenden Gesselschaft*, *96*(1–23).

Gilbert, L. A., & Bona, M. L. (2016). Permeability of oceanic crustal rock samples from IODP hole 1256D. *Geochemistry, Geophysics, Geosystems*, *17*(9), 3825–3832. https://doi.org/10.1002/2016gc006467

Gilbert, L. A., & Salisbury, M. H. (2011). Oceanic crustal velocities from laboratory and logging measurements of integrated ocean drilling program hole 1256D. *Geochemistry, Geophysics, Geosystems*, *12*(9). https://doi.org/10.1029/2011gc003750

Gilbert, L. A., Crispini, L., Tartarotti, P., & Bona, M. L. (2018). Permeability structure of the Lava-Dike transition of 15-Myr-Old oceanic crust formed at the east pacific rise. *Geochemistry, Geophysics, Geosystems*, *19*(9), 3555–3569. https://doi.org/10.1029/

2018gc007696

Glover, P. W. J. (2010). A generalized archie's law for n phases. *Geophysics*, *75*(6), E247–E265. https://doi.org/10.1190/1.3509781

Glover, P. W. J., Hole, M. J., & Pous, J. (2000). A modified archie's law for two conducting phases. *Earth and Planetary Science Letters*, *180*, 369–383.

Godel, B. (2013). High-Resolution X-Ray computed tomography and its application to ore deposits: From data acquisition to quantitative Three-Dimensional measurements with case studies from Ni-Cu-PGE deposits. *Economic Geology and the Bulletin of the Society of Economic Geologists*, *108*(8), 2005–2019. https://doi.org/10.2113/econgeo.108.8.2005

Greenberger, R. N., Harris, M., Ehlmann, B. L., Crotteau, M., Kelemen, P. B., Manning, C. E., et al. (2021). Hydrothermal alteration of the ocean crust and patterns in mineralization with depth as measured by micro-imaging infrared spectroscopy. *Journal of Geophysical Research, [Solid Earth]*. https://doi.org/10.1029/2021jb021976

Guéguen, Y., & Dienes, J. (1989). Transport properties of rocks from statistics and percolation. *Mathematical Geology*, *21*(1), 1–13. https://doi.org/10.1007/BF00897237

Guéguen, Y., & Kachanov, M. (2011). Effective elastic properties of cracked rocks — an overview. In Y. M. Leroy & F. K. Lehner (Eds.), *Mechanics of crustal rocks* (pp. 73–125). Vienna: Springer Vienna. https://doi.org/10.1007/978-3-7091-0939-7/_3

Guéguen, Y., & Palciauskas, V. (1994). *Introduction to the physics of rocks*. Princeton University Press.

Guéguen, Y., & Sarout, J. (2009). Crack-induced anisotropy in crustal rocks: Predicted dry and fluid-saturated thomsen's parameters. *Physics of the Earth and Planetary Interiors*, *172*(1), 116–124. https://doi.org/10.1016/j.pepi.2008.05.020

Guéguen, Y., & Sarout, J. (2011). Characteristics of anisotropy and dispersion in cracked medium. *Tectonophysics*, *503*(1), 165–172. https://doi.org/10.1016/j.tecto.2010.09.021

Guéguen, Y., & Schubnel, A. (2003). Elastic wave velocities and permeability of cracked rocks. *Tectonophysics*, *370*(1), 163–176. https://doi.org/10.1016/S0040-1951(03)00184-7

Guéguen, Y., Gavrilenko, P., & Le Ravalec, M. (1996). Scales of rock permeability. *Surveys in Geophysics*, *17*(3), 245–263. https://doi.org/10.1007/BF01904043

Guerin, G., Goldberg, D. S., & Iturrino, G. J. (2008). Velocity and attenuation in young oceanic crust: New downhole log results from DSDP/ODP/IODP holes 504B and 1256D. *Geochemistry, Geophysics, Geosystems*, *9*(12). https://doi.org/10.1029/2008gc002203

Gupta, L. P., Tanikawa, W., Hamada, Y., Hirose, T., Ahagon, N., Sugihara, T., et al. (2019). Examination of gas hydrate-bearing deep ocean sediments by x-ray computed tomography

and verification of physical property measurements of sediments. *Marine and Petroleum Geology*, *108*, 239–248. https://doi.org/10.1016/j.marpetgeo.2018.05.033

Hacker, B. R. (2008). H2O subduction beyond arcs. *Geochemistry, Geophysics, Geosystems*, *9*(3). https://doi.org/10.1029/2007gc001707

Hacker, B. R., Abers, G. A., & Peacock, S. M. (2003). Subduction factory 1. Theoretical mineralogy, densities, seismic wave speeds, and H2O contents. *Journal of Geophysical Research*, *108*(B1). https://doi.org/10.1029/2001jb001127

Han, T. (2018). An effective medium approach to modelling the pressure-dependent electrical properties of porous rocks. *Geophysical Journal International*, *214*(1), 70–78. https://doi.org/10.1093/gji/ggy125

Han, T., Yan, H., Xu, D., & Fu, L.-Y. (2020). Theoretical correlations between the elastic and electrical properties in layered porous rocks with cracks of varying orientations. *Earth-Science Reviews*, *211*, 103420. https://doi.org/10.1016/j.earscirev.2020.103420

Hassanzadegan, A., Blöcher, G., Milsch, H., Urpi, L., & Zimmermann, G. (2014). The effects of temperature and pressure on the porosity evolution of flechtinger sandstone. *Rock Mechanics and Rock Engineering*, *47*(2), 421–434. https://doi.org/10.1007/s00603-013-0401-z

Hatakeyama, K., Katayama, I., Abe, N., Okazaki, K., & Michibayashi, K. (2021). Effects of alteration and cracks on the seismic velocity structure of oceanic lithosphere inferred from ultrasonic measurements of mafic and ultramafic samples collected by the oman drilling project. *Journal of Geophysical Research, [Solid Earth]*. https://doi.org/10.1029/2021jb021923

Hosono, H., Takemura, T., Asahina, D., & Otsubo, M. (2022). Estimation of paleo-permeability around a seismogenic fault based on permeability tensor from observable geometric information of quartz veins. *Earth, Planets and Space*, *74*(1), 1–13. https://doi.org/10.1186/s40623-022-01694-3

Hudson, J. A. (1990). Overall elastic properties of isotropic materials with arbitrary distribution of circular cracks. *Geophysical Journal International*, *102*(2), 465–469. https://doi.org/10.1111/j.1365-246X.1990.tb04478.x

Ildefonse, B., & Pezard, P. (2001). Electrical properties of slow-spreading ridge gabbros from ODP site 735, southwest indian ridge. *Tectonophysics*, *330*(1-2), 69–92. https://doi.org/10.1016/s0040-1951(00)00220-1

Ildefonse, B., Drouin, M., Violay, M., et al. (2009). Data report: Electrical properties of gabbroic and troctolitic rocks from IODP hole U1309D, atlantis massif. *Proc. IODP*/

Volume.

Ioannou, S. E., & Spooner, E. T. C. (2007). Fracture analysis of a volcanogenic massive Sulfide-Related hydrothermal cracking zone, upper bell river complex, matagami, quebec: Application of permeability tensor theory. *Economic Geology and the Bulletin of the Society of Economic Geologists*, *102*(4), 667–690. https://doi.org/10.2113/gsecongeo.102.4.667

Iwamori, H., Ueki, K., Hoshide, T., Sakuma, H., Ichiki, M., Watanabe, T., et al. (2021). Simultaneous analysis of seismic velocity and electrical conductivity in the crust and the uppermost mantle: A forward model and inversion test based on grid search. *Journal of Geophysical Research, [Solid Earth]*, *126*(9). https://doi.org/10.1029/2021jb022307

Jerman, T. (2017, May). Jerman enhancement filter (https://github.com/timjerman/JermanEnhancementFilter), GitHub. https://github.com/timjerman/JermanEnhancementFilter.

Jerman, T., Pernuš, F., Likar, B., & Špiclin, Ž. (2015). Beyond frangi: An improved multiscale vesselness filter. In *Medical imaging 2015: Image processing* (Vol. 9413, p. 94132A). International Society for Optics; Photonics. https://doi.org/10.1117/12.2081147

Jerman, T., Pernus, F., Likar, B., & Spiclin, Z. (2016). Enhancement of vascular structures in 3D and 2D angiographic images. *IEEE Transactions on Medical Imaging*, *35*(9), 2107–2118. https://doi.org/10.1109/TMI.2016.2550102

Kachanov, M. (1994). Elastic solids with many cracks and related problems. In J. W. Hutchinson & T. Y. Wu (Eds.), *Advances in applied mechanics* (Vol. 30, pp. 259–445). Elsevier. https://doi.org/10.1016/S0065-2156(08)70176-5

Kalfarisi, R., Wu, Z. Y., & Soh, K. (2020). Crack detection and segmentation using deep learning with 3D reality mesh model for quantitative assessment and integrated visualization. *Journal of Computing in Civil Engineering*, *34*(3), 04020010. https://doi.org/10.1061/(ASCE)CP.1943-5487.0000890

Kan, R., & Sen, P. N. (1987). Electrolytic conduction in periodic arrays of insulators with charges. *The Journal of Chemical Physics*, *86*(10), 5748–5756. https://doi.org/10.1063/1.452502

Karato, S. (1983). Physical-properties of basalts from Deep-Sea drilling project Hole-504B, Costa-Rica rift. *Initial Reports of the Deep Sea Drilling Project*, *69*(MAY), 687–695.

Katayama, I., Terada, T., Okazaki, K., & Tanikawa, W. (2012). Episodic tremor and slow slip potentially linked to permeability contrasts at the moho. *Nature Geoscience*, *5*(10), 731–734. https://doi.org/10.1038/ngeo1559

Katayama, I., Abe, N., Hatakeyama, K., Akamatsu, Y., Okazaki, K., Ulven, O. I., et al.

(2020). Permeability profiles across the crust-mantle sections in the oman drilling project inferred from dry and wet resistivity data. *Journal of Geophysical Research, [Solid Earth]*, *125*(8). https://doi.org/10.1029/2019jb018698

Katayama, I., Abe, N., Okazaki, K., Hatakeyama, K., Akamatsu, Y., Michibayashi, K., et al. (2021). Crack geometry of serpentinized peridotites inferred from onboard ultrasonic data from the oman drilling project. *Tectonophysics*, *814*(228978), 228978. https://doi.org/10.1016/j.tecto.2021.228978

Kato, A., Iidaka, T., Ikuta, R., Yoshida, Y., Katsumata, K., Iwasaki, T., et al. (2010). Variations of fluid pressure within the subducting oceanic crust and slow earthquakes. *Geophysical Research Letters*, *37*(14). https://doi.org/10.1029/2010gl043723

Kelemen, P. B., Matter, J. M., Teagle, D. A. H., Coggon, J. A., & the Oman Drilling Project Science Team. (2020a). *Proceedings of the oman drilling project*. International Ocean Discovery Program College Station, TX.

Kelemen, P. B., Matter, J. M., Teagle, D. A. H., Coggon, J. A., & the Oman Drilling Project Science Team. (2020b). Site GT1: Layered cumulate gabbros and deep fault zones. In P. B. Kelemen, J. M. Matter, D. A. H. Teagle, J. A. Coggon, et al. (Eds.), *Proceedings of of the oman drilling project* (pp. 1–120). International Ocean Discovery Program, College Station, TX. https://doi.org/10.14379/OmanDP.proc.2020

Kelemen, P. B., Matter, J. M., Teagle, D. A. H., Coggon, J. A., & the Oman Drilling Project Science Team. (2020c). Site GT2: Foliated to layered gabbro transition. In P. B. Kelemen, J. M. Matter, D. A. H. Teagle, J. A. Coggon, et al. (Eds.), *Proceedings of of the oman drilling project* (pp. 1–130). International Ocean Discovery Program, College Station, TX. https://doi.org/10.14379/OmanDP.proc.2020

Kelemen, P. B., Matter, J. M., Teagle, D. A. H., Coggon, J. A., & the Oman Drilling Project Science Team. (2020d). Site GT3: Sheeted dike to gabbro transition. In P. B. Kelemen, J. M. Matter, D. A. H. Teagle, J. A. Coggon, et al. (Eds.), *Proceedings of of the oman drilling project* (pp. 1–152). International Ocean Discovery Program, College Station, TX. https://doi.org/10.14379/OmanDP.proc.2020

Key, K., Constable, S., Matsuno, T., Evans, R. L., & Myer, D. (2012). Electromagnetic detection of plate hydration due to bending faults at the middle america trench. *Earth and Planetary Science Letters*, *351-352*, 45–53. https://doi.org/10.1016/j.epsl.2012.07.020

Kita, S., Nakajima, J., Hasegawa, A., et al. (2014). Detailed seismic attenuation structure beneath hokkaido, northeastern japan: Arc-arc collision process, arc magmatism, and seismotectonics. *Journal of.*

Kodaira, S., Iidaka, T., Kato, A., Park, J.-O., Iwasaki, T., & Kaneda, Y. (2004). High pore fluid pressure may cause silent slip in the nankai trough. *Science*, *304*(5675), 1295–1298. https://doi.org/10.1126/science.1096535

Korenaga, J. (2007). Thermal cracking and the deep hydration of oceanic lithosphere: A key to the generation of plate tectonics? *Journal of Geophysical Research*, *112*(B5). https://doi.org/10.1029/2006jb004502

Kurz, J. H., Grosse, C. U., & Reinhardt, H.-W. (2005). Strategies for reliable automatic onset time picking of acoustic emissions and of ultrasound signals in concrete. *Ultrasonics*, *43*(7), 538–546. https://doi.org/10.1016/j.ultras.2004.12.005

Kuster, G. T., & Toksöz, M. N. (1974). Velocity and attenuation of seismic waves in two-phase media: Part i. Theoretical formulations. *Geophysics*, *39*(5), 587–606. https://doi.org/10.1190/1.1440450

Kuwatani, T., Nagata, K., Okada, M., & Toriumi, M. (2014). Markov random field modeling for mapping geofluid distributions from seismic velocity structures. *Earth, Planets and Space*, *66*(1), 5. https://doi.org/10.1186/1880-5981-66-5

Lang, P. S., Paluszny, A., & Zimmerman, R. W. (2014). Permeability tensor of three-dimensional fractured porous rock and a comparison to trace map predictions. *Journal of Geophysical Research, [Solid Earth]*, *119*(8), 6288–6307. https://doi.org/10.1002/2014jb011027

Le Ravalec, M., & Guéguen, Y. (1996). High- and low-frequency elastic moduli for a saturated porous/cracked rock-differential self-consistent and poroelastic theories. *Geophysics*, *61*(4), 1080–1094. https://doi.org/10.1190/1.1444029

Li, J. H., Zhang, L. M., Wang, Y., & Fredlund, D. G. (2009). Permeability tensor and representative elementary volume of saturated cracked soil. *Canadian Geotechnical Journal*, *46*(8), 928–942. https://doi.org/10.1139/t09-037

Manning, C. E., Weston, P. E., & Mahon, K. I. (1996). Rapid high-temperature metamorphism of east pacific rise gabbros from hess deep. *Earth and Planetary Science Letters*, *144*(1), 123–132. https://doi.org/10.1016/0012-821X(96)00153-7

Martel, S. J. (1999). Analysis of fracture orientation data from boreholes. *Environmental & Engineering Geoscience*, (2), 213–233.

Massiot, C., McNamara, D. D., Lewis, B., & Bignall, G. (2012). Statistical corrections of fracture sampling bias in boreholes from acoustic televiewer logs. In *New zealand geothermal workshop 2012*. unknown. https://doi.org/10.13140/RG.2.1.4187.8009

Matonti, C., Guglielmi, Y., Viseur, S., Bruna, P. O., Borgomano, J., Dahl, C., & Marié, L.

(2015). Heterogeneities and diagenetic control on the spatial distribution of carbonate rocks acoustic properties at the outcrop scale. *Tectonophysics*, *638*, 94–111. https://doi.org/10.1016/j.tecto.2014.10.020

Mavko, G., Mukerji, T., & Dvorkin, J. (2020). *The rock physics handbook*. Cambridge University Press.

Michibayashi, K., Tominaga, M., Ildefonse, B., & Teagle, D. (2019). What lies beneath: The formation and evolution of oceanic lithosphere. *Oceanography*, *32*(1), 138–149. https://doi.org/10.5670/oceanog.2019.136

Müller, R. D., & Dutkiewicz, A. (2018). Oceanic crustal carbon cycle drives 26-million-year atmospheric carbon dioxide periodicities. *Science Advances*, *4*(2), eaaq0500. https://doi.org/10.1126/sciadv.aaq0500

Müller, T. M., Gurevich, B., & Lebedev, M. (2010). Seismic wave attenuation and dispersion resulting from wave-induced flow in porous rocks — a review. *Geophysics*, *75*(5), 75A147–75A164. https://doi.org/10.1190/1.3463417

Nagase, K., Hatakeyama, K., Okazaki, K., Akamatsu, Y., Abe, N., Michibayashi, K., & Katayama, I. (2022). Simultaneous measurements of elastic wave velocity and porosity of epidosites collected from the oman ophiolite: Implication for low V $_P$ /v $_S$ anomaly in the oceanic crust. *Geophysical Research Letters*. https://doi.org/10.1029/2022gl098234

Naif, S., Key, K., Constable, S., & Evans, R. L. (2015). Water-rich bending faults at the middle america trench. *Geochemistry, Geophysics, Geosystems*, *16*(8), 2582–2597. https://doi.org/10.1002/2015gc005927

Nakajima, J., & Uchida, N. (2018). Repeated drainage from megathrusts during episodic slow slip. *Nature Geoscience*, *11*(5), 351–356. https://doi.org/10.1038/s41561-018-0090-z

Nara, Y., Meredith, P. G., Yoneda, T., & Kaneko, K. (2011). Influence of macro-fractures and micro-fractures on permeability and elastic wave velocities in basalt at elevated pressure. *Tectonophysics*, *503*(1), 52–59. https://doi.org/10.1016/j.tecto.2010.09.027

Nehlig, P. (1994). Fracture and permeability analysis in magma-hydrothermal transition zones in the samail ophiolite (oman). *Journal of Geophysical Research*, *99*(B1), 589–601. https://doi.org/10.1029/93jb02569

Nehlig, P., & Juteau, T. (1988). Flow porosities, permeabilities and preliminary data on fluid inclusions and fossil thermal gradients in the crustal sequence of the sumail ophiolite (oman). *Tectonophysics*.

Nehlig, P., Juteau, T., Bendel, V., & Cotten, J. (1994). The root zones of oceanic hydrothermal systems: Constraints from the samail ophiolite (oman). *Journal of Geophysical*

Research, *99*(B3), 4703–4713. https://doi.org/10.1029/93jb02663

Nicolas, A., Boudier, F., Ildefonse, B., & Ball, E. (2000). Accretion of oman and united arab emirates ophiolite – discussion of a new structural map. *Marine Geophysical Researches*, *21*(3), 147–180. https://doi.org/10.1023/A:1026769727917

Norton, D., & Knapp, R. (1977). Transport phenomena in hydrothermal systems: The nature of porosity. *American Journal of Science*, *277*.

O'Connell, R. J., & Budiansky, B. (1974). Seismic velocities in dry and saturated cracked solids. *Journal of Geophysical Research*, *79*(35), 5412–5426. https://doi.org/10.1029/jb079i035p05412

Oda, M. (1982). FABRIC TENSOR FOR DISCONTINUOUS GEOLOGICAL MATERIALS. *Soils and Foundations*, *22*(4), 96–108. https://doi.org/10.3208/sandf1972.22.4/_96

Oda, M. (1985). Permeability tensor for discontinuous rock masses. *Géotechnique*, *35*(4), 483–495. https://doi.org/10.1680/geot.1985.35.4.483

Oda, M., Katsube, T., & Takemura, T. (2002). Microcrack evolution and brittle failure of inada granite in triaxial compression tests at 140 MPa. *Journal of Geophysical Research*, *107*(B10), ECV 9-1-ECV 9-17. https://doi.org/10.1029/2001jb000272

Ohtani, T., Nakano, T., Nakashima, Y., & Muraoka, H. (2001). Three-dimensional shape analysis of miarolitic cavities and enclaves in the kakkonda granite by x-ray computed tomography. *Journal of Structural Geology*, *23*(11), 1741–1751. https://doi.org/10.1016/S0191-8141(01)00033-5

Okazaki, K., Michibayashi, K., Hatakeyama, K., Abe, N., Johnson, K. T. M., Kelemen, P. B., & the Oman Drilling Project Science Team. (2021). Major mineral fraction and physical properties of carbonated peridotite (listvenite) from ICDP oman drilling project hole BT1B inferred from x-ray CT core images. *Journal of Geophysical Research, [Solid Earth]*, *126*(12). https://doi.org/10.1029/2021jb022719

Paterson, M. S., & Wong, T.-F. (2005). *Experimental rock deformation - the brittle field*. Springer Science & Business Media.

Peacock, S. M. (2001). Are the lower planes of double seismic zones caused by serpentine dehydration in subducting oceanic mantle? *Geology*, *29*(4), 299–302. https://doi.org/10.1130/0091-7613(2001)029%3C0299:ATLPOD%3E2.0.CO;2

Pezard, P. A. (1990). Electrical properties of mid-ocean ridge basalt and implications for the structure of the upper oceanic crust in hole 504B. *Journal of Geophysical Research*, *95*(B6), 9237. https://doi.org/10.1029/jb095ib06p09237

Pimienta, L., Sarout, J., Esteban, L., David, C., & Clennell, M. B. (2017). Pressure-

dependent elastic and transport properties of porous and permeable rocks: Microstructural control. *Journal of Geophysical Research, [Solid Earth]*, *122*(11), 8952–8968. https://doi.org/10.1002/2017jb014464

Pimienta, L., Schubnel, A., Violay, M., Fortin, J., Guéguen, Y., & Lyon-Caen, H. (2018). Anomalous V p / V s ratios at seismic frequencies might evidence highly damaged rocks in subduction zones. *Geophysical Research Letters*, *45*(22), 12, 210–12, 217. https://doi.org/10.1029/2018gl080132

Pimienta, L., Orellana, L. F., & Violay, M. (2019). Variations in elastic and electrical properties of crustal rocks with varying degree of microfracturation. *Journal of Geophysical Research, [Solid Earth]*, *124*(7), 6376–6396. https://doi.org/10.1029/2019jb017339

Pride, S. R., Berryman, J. G., & Harris, J. M. (2004). Seismic attenuation due to wave-induced flow. *Journal of Geophysical Research*, *109*(B1). https://doi.org/10.1029/2003jb002639

Pride, S. R., Berryman, J. G., Commer, M., Nakagawa, S., Newman, G. A., & Vasco, D. W. (2017). Changes in geophysical properties caused by fluid injection into porous rocks: Analytical models. *Geophysical Prospecting*, *65*(3), 766–790. https://doi.org/10.1111/1365-2478.12435

Priest, S. D. (1993). *Discontinuity analysis for rock engineering.* Springer, Dordrecht. https://doi.org/10.1007/978-94-011-1498-1

Revil, A., & Glover, P. W. J. (1998). Nature of surface electrical conductivity in natural sands, sandstones, and clays. *Geophysical Research Letters*, *25*(5), 691–694. https://doi.org/10.1029/98gl00296

Ringrose, P. S., Martinius, A. W., & Alvestad, J. (2008). Multiscale geological reservoir modelling in practice. *Geological Society London Special Publications*, *309*(1), 123–134. https://doi.org/10.1144/SP309.9

Saffer, D. M., & Tobin, H. J. (2011). Hydrogeology and mechanics of subduction zone forearcs: Fluid flow and pore pressure. *Annual Review of Earth and Planetary Sciences*, *39*(1), 157–186. https://doi.org/10.1146/annurev-earth-040610-133408

Sarout, J., Ferjani, M., & Guéguen, Y. (2009). A semi-automatic processing technique for elastic-wave laboratory data. *Ultrasonics*, *49*(4-5), 452–458. https://doi.org/10.1016/j.ultras.2008.12.001

Sayers, C. M., & Kachanov, M. (1995). Microcrack-induced elastic wave anisotropy of brittle rocks. *Journal of Geophysical Research*, *100*(B3), 4149–4156. https://doi.org/10.1029/94jb03134

Schubnel, A., & Guéguen, Y. (2003). Dispersion and anisotropy of elastic waves in cracked

rocks. *Journal of Geophysical Research*, *108*(B2). https://doi.org/10.1029/2002jb001824

Schubnel, A., Benson, P. M., Thompson, B. D., Hazzard, J. F., & Young, R. P. (2006). Quantifying damage, saturation and anisotropy in cracked rocks by inverting elastic wave velocities. In G. Dresen, A. Zang, & O. Stephansson (Eds.), *Rock damage and fluid transport, part I* (pp. 947–973). Basel: Birkhäuser Basel. https://doi.org/10.1007/3-7643-7712-7/_3

Schulze-Makuch, D., Carlson, D. A., Cherkauer, D. S., & Malik, P. (1999). Scale dependency of hydraulic conductivity in heterogeneous media. *Ground Water*, *37*(6), 904–919. https://doi.org/10.1111/j.1745-6584.1999.tb01190.x

Schwalenberg, K., Rippe, D., Koch, S., & Scholl, C. (2017). Marine-controlled source electromagnetic study of methane seeps and gas hydrates at opouawe bank, hikurangi margin, new zealand. *Journal of Geophysical Research, [Solid Earth]*, *122*(5), 3334–3350. https://doi.org/10.1002/2016jb013702

Shafiro, B., & Kachanov, M. (1997). Materials with fluid-filled pores of various shapes: Effective elastic properties and fluid pressure polarization. *International Journal of Solids and Structures*, *34*(27), 3517–3540. https://doi.org/10.1016/S0020-7683(96)00185-0

Shearer, P. M. (1988). Cracked media, poisson's ratio and the structure of the upper oceanic crust. *Geophysical Journal International*, *92*(2), 357–362. https://doi.org/10.1111/j.1365-246X.1988.tb01149.x

Stein, C. A., & Stein, S. (1994). Constraints on hydrothermal heat flux through the oceanic lithosphere from global heat flow. *Journal of Geophysical Research*, *99*(B2), 3081–3095. https://doi.org/10.1029/93jb02222

Suzuki, Y., Yamashita, S., Kouduka, M., Ao, Y., Mukai, H., Mitsunobu, S., et al. (2020). Deep microbial proliferation at the basalt interface in 33.5–104 million-year-old oceanic crust. *Communications Biology*, *3*(1), 1–9. https://doi.org/10.1038/s42003-020-0860-1

Swift, S., Reichow, M., Tikku, A., Tominaga, M., & Gilbert, L. (2008). Velocity structure of upper ocean crust at ocean drilling program site 1256. *Geochemistry, Geophysics, Geosystems*, *9*(10). https://doi.org/10.1029/2008gc002188

Taibi, F., Akbarizadeh, G., & Farshidi, E. (2019). Robust reservoir rock fracture recognition based on a new sparse feature learning and data training method. *Multidimensional Systems and Signal Processing*, *30*(4), 2113–2146. https://doi.org/10.1007/s11045-019-00645-8

Takai, K., Nakamura, K., Toki, T., Tsunogai, U., Miyazaki, M., Miyazaki, J., et al. (2008). Cell proliferation at 122°c and isotopically heavy CH_4 production by a hyperthermophilic

methanogen under high-pressure cultivation. *Proceedings of the National Academy of Sciences*, *105*(31), 10949–10954. https://doi.org/10.1073/pnas.0712334105

Takei, Y. (2002). Effect of pore geometry onVP/VS: From equilibrium geometry to crack. *Journal of Geophysical Research*, *107*(B2). https://doi.org/10.1029/2001jb000522

Teagle, D. A. H., Alt, J. C., Umino, S., Miyashita, S., Banerjee, N. R., & Wilson, D S, and the Expedition 309/312 Scientists. (2006). *Site 1256D* (Vol. 309/312, pp. 1–549). Proceedings of the Integrated Ocean Drilling Program.

Terzaghi, R. D. (1965). Sources of error in joint surveys. *Géotechnique*, *15*(3), 287–304. https://doi.org/10.1680/geot.1965.15.3.287

Tominaga, M., Teagle, D. A. H., Alt, J. C., & Umino, S. (2009). Determination of the volcanostratigraphy of oceanic crust formed at superfast spreading ridge: Electrofacies analyses of ODP/IODP hole 1256D. *Geochemistry, Geophysics, Geosystems*, *10*(1). https://doi.org/10.1029/2008gc002143

Tonai, S., Kubo, Y., Tsang, M. Y., Bowden, S., Ide, K., et al. (2019). A new method for quality control of geological cores by x-ray computed tomography: Application in IODP expedition 370. *Frontiers in Earth*.

Tsuji, T., Dvorkin, J., Mavko, G., Nakata, N., Matsuoka, T., Nakanishi, A., et al. (2011). VP/VS ratio and shear-wave splitting in the nankai trough seismogenic zone: Insights into effective stress, pore pressure, and sediment consolidation. *Geophysics*, *76*(3), WA71–WA82. https://doi.org/10.1190/1.3560018

van Everdingen. (1995). Fracture characteristics of the sheeted dike complex, troodos ophiolite, cyprus: Implications for permeability of oceanic crust. *Journal of Geophysical Research*, *100*(B10), 19957–19972. https://doi.org/10.1029/95JB01575

Violay, M., Pezard, P. A., Ildefonse, B., Belghoul, A., & Laverne, C. (2010). Petrophysical properties of the root zone of sheeted dikes in the ocean crust: A case study from hole ODP/IODP 1256D, eastern equatorial pacific. *Tectonophysics*, *493*(1), 139–152. https://doi.org/10.1016/j.tecto.2010.07.013

Voorn, M., Exner, U., & Rath, A. (2013). Multiscale hessian fracture filtering for the enhancement and segmentation of narrow fractures in 3D image data. *Computers & Geosciences*, *57*, 44–53. https://doi.org/10.1016/j.cageo.2013.03.006

Walsh, J. B. (1965). The effect of cracks on the compressibility of rock. *Journal of Geophysical Research*, *70*(2), 381–389. https://doi.org/10.1029/jz070i002p00381

Walsh, J. B., & Brace, W. F. (1984). The effect of pressure on porosity and the transport properties of rock. *Journal of Geophysical Research*, *89*(B11), 9425. https://doi.org/10.

1029/jb089ib11p09425

Warren-Smith, E., Fry, B., Wallace, L., Chon, E., Henrys, S., Sheehan, A., et al. (2019). Episodic stress and fluid pressure cycling in subducting oceanic crust during slow slip. *Nature Geoscience*, *12*(6), 475–481. https://doi.org/10.1038/s41561-019-0367-x

Watanabe, T., Makimura, M., Kaiwa, Y., Desbois, G., Yoshida, K., & Michibayashi, K. (2019). Elastic wave velocity and electrical conductivity in a brine-saturated rock and microstructure of pores. *Earth, Planets and Space*, *71*(1), 1–12. https://doi.org/10.1186/s40623-019-1112-9

Waxman, M. H., & Smits, L. J. M. (1968). Electrical conductivities in oil-bearing shaly sands. *Society of Petroleum Engineers Journal*, *8*(02), 107–122.

Wilkens, R. H., Fryer, G. J., & Karsten, J. (1991). Evolution of porosity and seismic structure of upper oceanic crust: Importance of aspect ratios. *Journal of Geophysical Research*, *96*(B11), 17981. https://doi.org/10.1029/91jb01454

Williams, J. N., Toy, V. G., Massiot, C., McNamara, D. D., Smith, S. A. F., & Mills, S. (2018). Controls on fault zone structure and brittle fracturing in the foliated hanging wall of the alpine fault. *Solid Earth*, *9*(2), 469–489. https://doi.org/10.5194/se-9-469-2018

Yarce, J., Sheehan, A. F., Nakai, J. S., Schwartz, S. Y., Mochizuki, K., Savage, M. K., et al. (2019). Seismicity at the northern hikurangi margin, new zealand, and investigation of the potential spatial and temporal relationships with a shallow slow slip event. *Journal of Geophysical Research, [Solid Earth]*, *124*(5), 4751–4766. https://doi.org/10.1029/2018jb017211

Zhang, C., Koepke, J., Wolff, P. E., Horn, I., Garbe-Schönberg, D., & Berndt, J. (2021). Multi-stage hydrothermal veins in layered gabbro of the oman ophiolite: Implications for focused fluid circulation in the lower oceanic crust. *Journal of Geophysical Research, [Solid Earth]*, *126*(8). https://doi.org/10.1029/2021jb022349

Zhao, B., Saxena, N., Hofmann, R., Pradhan, C., & Hows, A. (2023). Enhancing resolution of micro-CT images of reservoir rocks using super resolution. *Computers & Geosciences*, *170*, 105265. https://doi.org/10.1016/j.cageo.2022.105265

Zihlmann, B., Müller, S., Coggon, R. M., Koepke, J., Garbe-Schönberg, D., & Teagle, D. A. H. (2018). Hydrothermal fault zones in the lower oceanic crust: An example from wadi gideah, samail ophiolite, oman. *Lithos*, *323*, 103–124. https://doi.org/10.1016/j.lithos.2018.09.008